Investigation of the growth process of thin iron oxide films: Analysis of X-ray Photoemission Spectra by Charge Transfer Multiplet calculations

PhD. thesis

for the degree of
Doktor der Naturwissenschaften (Dr. rer. nat.)

presented to the
Department of Physics
of the University of Osnabrück
by

Martin Suendorf, Dipl. Phys.

UNIVERSITÄT OSNABRÜCK

October 2012

"The world is made up of four elements: Earth, Air, Fire and Water. This is a fact well known [...]. It's also wrong. There's a fifth element, and generally it's called Surprise."

Terry Pratchett - *The Truth*

Contents

1 Introduction

Technological progress recently involves two major aspects that play important roles in current developments. The continuing miniaturization of electronical components is the key to increasing computation power of modern computers. Smaller dimensions reduce the circuit time and energy consumption of microchips and allow higher storage densities for hard drives. This greatly improves the performance of processors and the data access rate. The second important area of research involves the incorporation of new materials into existing technologies and the tuning of material properties to required specifications. Varying the stoichiometry of composite materials or doping with foreign atoms can change the electrical, optical and magnetic properties for enhanced effectivity in technological applications [1, 2, 3, 4]. These include not only electronical devices but also catalytic surfaces for biological or chemical processes [5] and surface coatings with specific optical properties [6, 7].

Iron oxides are a frequently used material in thin film technology. The oxide phases magnetite (Fe_3O_4) and maghemite ($\gamma\text{-}Fe_2O_3$) are ferrimagnetic and therefore suitable in the implementation of magnetic data storage devices. Additionally the oxides exhibit interesting electronical properties. While maghemite is an insulator, magnetite is highly conductive at room temperature due to a large electron hopping between octahedral Fe sites [8]. It has also been shown that magnetite is spin-polarized at the FERMI edge [9, 10]. The combination of these properties makes magnetite a promising candidate for applications in spintronics [11].

Current investigations regarding iron oxides accordingly have a focus on the preparation of thin films. The formation of oxide phases is observed under varying preparation conditions [12, 13, 14]. A recurring problem here is the often reported segregation of substrate atoms into the oxide film during deposition. Furthermore the surface structure of the films could not yet be described conclusively. The characteristic $(\sqrt{2} \times \sqrt{2})R45°$ surface reconstruction of magnetite as well as other observed reconstructions [15, 16] are attributed either to an A or a B termination of the spinel (001) surface [17, 18] or to the influence of segregated substrate material.

In this work the process of oxidation in ultra-thin films is investigated. Iron oxide films are prepared by two different methods to study differences in the film growth. One set of samples is prepared by deposition of Fe in an oxygen atmosphere, a second set consists of Fe films oxidized after deposition by exposure to oxygen. For both sets the influence of the substrate temperature on the film properties is investigated. To obtain structural information X-ray Reflectivity, X-ray Diffraction and Low Energy Electron Diffraction measurements are performed. The chemical state of the samples is investigated by X-ray Photoelectron Spectroscopy. Charge Transfer Multiplet calculations [19] are established as a means to analyze photoemission spectra of transition metal oxides. These calculations can extract additional information from photoemission measurements and are shown to be a useful tool to characterize Fe oxide films.

Section 2 will give a short introduction into the theories of the employed experimental and theoretical techniques. The following Section will give an overview over the investigated materials, and Section 4 describes the experimental setups and analytical procedures used in this work. The results of the different experimental methods are presented in Section 5. The influence of different parameters on the oxide films will be discussed in Section 6. The last Section of this work gives a short summary of the contents and presents reasonable expansions for the current work.

2 Theoretical background

The characterization of ultra thin films requires a combination of different experimental techniques to cover all important properties. In this work the electronical and chemical properties of the films are examined by x-ray photoelectron spectroscopy, the film thickness by x-ray reflection and the structural properties by low energy electron diffraction and x-ray diffraction. Charge Transfer Multiplet calculations are performed to identify certain oxide species in photoelectron spectra. The following Section will explain the basic principles necessary to understand these methods.

2.1 X-ray Photoelectron Spectroscopy

X-ray Photoelectron Spectroscopy (XPS) is a powerful tool to investigate chemical and electronical properties of thin films. The method is based on the photoelectric effect, also known as HALLWACHS effect, named after WILHELM HALLWACHS, who in 1886 together with his co-worker HEINRICH HERTZ was the first scientist to study the effect previously observed by ALEXANDRE EDMOND BEQUEREL in 1839. Only in 1905 the photoelectric effect was finally explained theoretically by ALBERT EINSTEIN. In 1922 he received the NOBEL prize in physics for his work in this field. Also awarded with the NOBEL prize was KAI SIEGBAHN in 1981 for his contribution to the development of high resolution spectrometers.

2.1.1 Photoelectric effect

An electron can be emitted from a solid if it absorbs the energy of an incident photon. This phenomenon is called photoelectric effect. The energy of a photon is given as $E_{ph} = h \cdot \nu$, where h is the Planck constant and ν is the frequency of the electromagnetic wave which can be transferred to its wavelength via $\lambda = c/\nu$ with the velocity of light $c = 299792.458\,\mathrm{km/s}$. The kinetic energy of an emitted photoelectron is then given by

$$E_{kin} = h \cdot \nu - \Phi. \tag{2.1}$$

The term Φ is called *work function*. It takes into account the energy difference between a free electron and the FERMI energy of a solid. This energy difference must be overcome to emit an electron near to the FERMI edge. Electrons nearer to the atomic core experience a higher attractive potential than electrons at the FERMI edge. The additional binding energy E_B of core electrons must be included in Equation (2.1) as

$$E_{kin} = h \cdot \nu - \Phi - E_B. \tag{2.2}$$

The energies and potentials defined here are outlined in Figure 2.1. The kinetic energy E'_{kin} measured by the spectrometer differs from the actual kinetic energy of the free electron E_{kin}
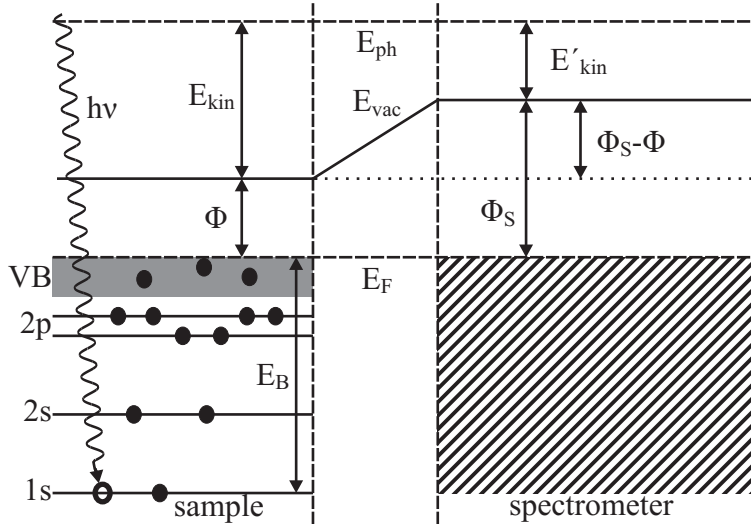
Figure 2.1: *Potentials and energies in a photoemission process. A photon with $E = h\nu$ creates a core hole and a photoelectron in the 1s shell with binding energy E_B. The kinetic energy follows from Equation (2.1). A modified kinetic energy E'_{kin} is measured because the work functions of sample and spectrometer are different.*

by the difference in the work functions of the sample and the spectrometer $\Phi_S - \Phi$. This effect is compensated by careful calibration of the measured kinetic energy for a known sample and electron orbital. A mutual electrical grounding of sample and spectrometer assures that the FERMI energy is the same for both.

The measured kinetic energy of a photoelectron can then be converted to a binding energy for the electron shell in the solid. For this it must be assumed that the electron orbitals remain unchanged after photoemission of one electron. This is stated by KOOPMANS theorem, which says that the ionization energy is the negative energy of the respective electron orbital [20]. In reality, an excited (N-1)-electron system will relax with a time constant of the order of 10^{-15} s. This relaxation process is too fast to be observed by the spectrometer, but the measured kinetic electron energies will already reflect the relaxed system. Thus, the initial and final states of the ionization process influence the measured binding energies. This leads to a broadening of photoemission spectra due to slight energy shifts for individual photoelectrons.

An electron emitted from its orbital can interact either with other electrons (if its kinetic energy is high) or with the crystal lattice (if its energy is low) on its course through the solid. These interactions limit the mobility of the photoelectrons, in this context one speaks of the *inelastic mean free path* (IMFP) λ_{in}. For typical photoelectron energies between $E_{kin} = 1500$ eV and $E_{kin} = 50$ eV it has a value ranging from $\lambda_{in} = 3$ nm to $\lambda_{in} = 0.3$ nm [21]. The penetration depth of x-rays for incident angles around 40° is significantly larger (> 100 nm
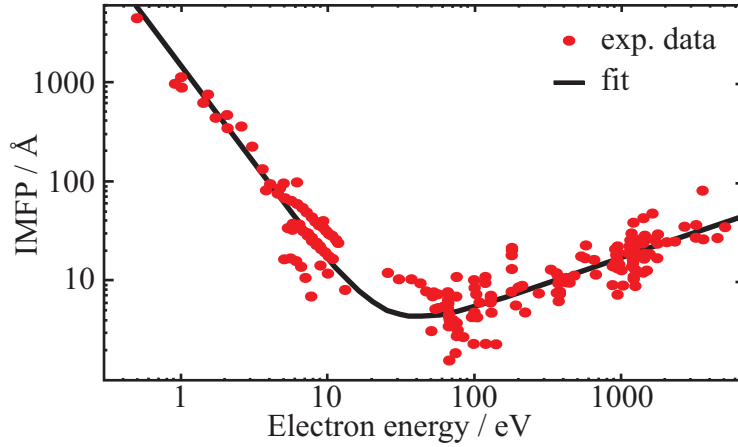
Figure 2.2: *Energy dependence of the IMFP of electrons in a solid. Red dots represent measurement data, the solid black line is a function fitted to the data. Taken from* [21].

for iron oxide [22]) than the IMFP of photoelectrons. The depth perception of XPS is therefore limited by λ_{in}, no photoelectron signal from atoms more than $5 - 10\,\text{nm}$ below the surface can be detected. This makes photoelectron spectroscopy much more surface sensitive than other techniques using x-rays like XRD or XRR (cf. Sections 2.3 and 2.5). Figure 2.2 shows the energy dependence of λ_{in}.

2.1.2 Photoemission spectra

The measured binding energies of photoelectrons are characteristic for each element and each electron orbital. In photoelectron spectroscopy the quantity of emitted electrons is measured as a function of the kinetic energy which can be converted to a binding energy for the respective electron orbital via Equation (2.2). Each orbital that emits electrons generates a peak in the photoemission spectrum. These peaks are labeled according to the quantum numbers of the contributing electron orbitals. The orbitals are labeled after a combination of the principal quantum number $n \in \mathbb{N}^*$, the orbital angular momentum quantum number l with values $l = 0, 1, \ldots, n-1$ and the total angular momentum quantum number $j = |\boldsymbol{l}| \pm |\boldsymbol{s}|$, where $|\boldsymbol{s}| = 1/2$ is the spin of an electron. Conventionally the orbital angular momentum quantum number is denoted with the letters $s, p, d \ldots$ for the values $0, 1, 2 \ldots$, respectively. The common nomenclature for photoemission peaks is then given as nl_j, for example $3d_{5/2}$ for an orbital with the quantum numbers $n = 3$, $l = 2$ and $j = 5/2$. In the case of $l = 0$ the one remaining value for j is usually omitted as in $2s$ for the quantum numbers $n = 2$ and $l = 0$.

The measured intensity of photoelectrons can be given by [23]

$$I = J_0 \cdot \sigma(E_{ph}) \cdot T \cdot \int\limits_0^\pi d\gamma \cdot L(\gamma) \cdot \int\limits_0^{2\cdot\pi} d\phi \cdot \int\limits_0^\infty dz \cdot n(z) \cdot e^{\frac{-z}{\lambda_{in} \cdot \cos\Theta}}. \tag{2.3}$$

Here J_0 is the intensity of the incident x-ray radiation. σ is the photoionization cross section that defines the interaction probability between an electron orbital and an incident photon with the energy E_{ph}. T is the transmission function that describes the transmission characteristics of the spectrometer. The first two integrals describe the spatial distribution of the photoemission, where γ is the angle between the x-ray beam and emitted electron beam and L describes the angular dependence of photoemission. The last integral handles the depth dependence of photoemission. Electrons excited farther away from the sample surface, at depth z, contribute less to the photoemission spectrum because of the limited IMFP λ_{in}.

The measured intensity of a photoelectron peak is always subject to energy broadening. Including the broadening due to final state effects (cf. Section 2.1.1), the full width at half maximum (FWHM) of a peak is given by [24]

$$\gamma = \sqrt{\gamma_x^2 + \gamma_s^2 + \gamma_a^2}. \tag{2.4}$$

The three contributions to the FWHM originate from the energy broadening of the x-ray source (γ_x), the lifetime of the excited state in the sample (γ_s) and the resolution of the electron analyzer (γ_a). This leads to peak shapes that are commonly described by a combination of a Lorentzian and a Gaussian function rather than by a δ-function-like shape expected for emission with one distinct kinetic energy. The Gaussian function simulates the instrumental broadening of the peak and the Lorentzian function simulates the lifetime broadening of the excited state.

2.1.2.1 Background intensity

The limited IMFP of electrons in solids can lead to a loss of kinetic energy for some photoelectrons emitted from their orbital. If the reduced kinetic energy at the surface suffices to overcome the work function, the electron is detected in the spectrum with an apparently increased binding energy compared to the main line caused by the electron orbital. This is called *inelastic background*. To compare the intensities or areas of different peaks, this background must be subtracted from the measured spectrum to obtain the real peak intensity.

Two different methods are most commonly used for this purpose. The empirical approach of Shirley [25] assumes that at each kinetic energy the background intensity is proportional to the integrated intensity at higher energies

$$I'(E) = I(E) - I'(E_0) \left(\frac{\sum_{E'>E} I(E')}{\sum_{E'>E_0} I(E')} \right). \tag{2.5}$$
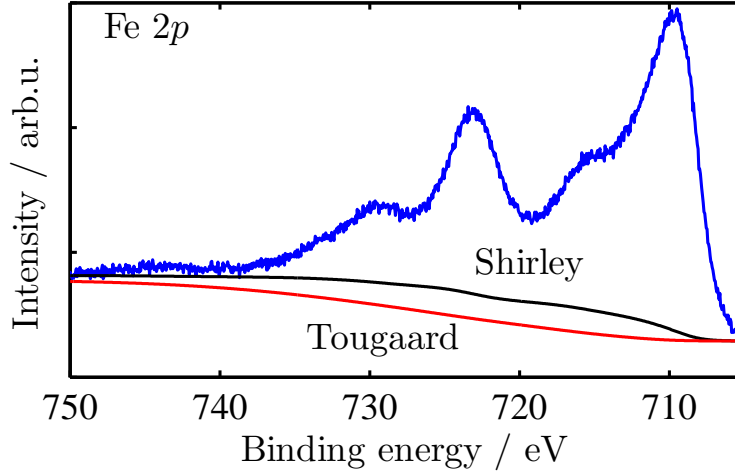
Figure 2.3: *Calculated background intensity for a Fe 2p photoemission spectrum. A* SHIRLEY *background (black line) gains a considerably higher intensity than a* TOUGAARD *background (red line). The integrated peak intensity differs by about 15 %.*

Here $I(E)$ is the measured photoelectron intensity, $I'(E)$ the corrected intensity, and E_0 is the lowest kinetic energy in the examined region of the photoemission spectrum. Iteration of Equation (2.5) gives the background intensity at each kinetic energy. This method does not reproduce the real background caused by inelastic electron energy loss but provides reasonably good results for all material systems. It should be noted that the obtained background intensity strongly depends on the photoelectron intensity at the boundaries of the considered energy interval.

Tougaard [26] proposed a different approach based on actual electron energy loss measurements (EELS). He found that the background intensity can be calculated by

$$F(E) = J(E) - \lambda_{in} \cdot \int\limits_{E}^{\infty} dE' \cdot K(E' - E) \cdot J(E'), \qquad (2.6)$$

where $J(E)$ is the flux of emitted electrons with kinetic energy E, λ_{in} is the IMFP of the electron and $K(E)$ is the probability that an electron will lose energy before reaching the surface. In the case that $K(E)$ is more or less independent of energy, the term $\lambda_{in} \cdot K(E)$ can be approximated by a universal cross-section $\lambda_{in} \cdot K_0 \simeq \frac{B \cdot T}{(C+T^2)^2}$ where T is the energy loss of an electron. This technique is independent of the energy interval, but the parameters B and C must be optimized for each material individually. For metals and their oxides $B = 2866 \, \text{eV}^2$ and $C = 1643 \, \text{eV}^2$ are good approximations [27].

Figure 2.3 shows a comparison between the two calculation methods. The backgrounds

are calculated for an Fe $2p$ photoemission spectrum using the same energy interval. A SHIRLEY background (black line) gains a higher intensity than a TOUGAARD background (red line). The difference in the integrated intensity of the peak area is about 15%. The peak areas in XPS can be used for a quantitative analysis of films, therefore the subtraction of a suitable background is essential in the process (cf. Section 2.1.2.6).

2.1.2.2 Satellite structures

The inelastic electron energy loss described in Section 2.1.2.1 is an *extrinsic* effect causing a continuous background over the whole photoemission spectrum. Here *extrinsic* means that the energy loss occurs outside the original excited atom. In addition, *intrinsic* effects in the emitting atom can cause discrete peaks shifted with respect to the main photoemission peak. These peaks are called *satellites*.

Intrinsic effects always decrease the kinetic energy of the photoelectron, thus the satellite peaks are always shifted to higher binding energies. In a *shake-up*-process the photoexcitation of one electron causes a second electron on the same atom to jump to a higher energy level. The energy it gains by this is taken from the kinetic energy of the emitted electron. In a *shake-off*-process the second electron takes enough energy from the primary photoelectron as to also be emitted from the atom.

The radiation source can also be a cause for satellite structures. Ideally the photoexcitation includes only one photon energy, typically the $K_{\alpha 1}$ radiation of the x-ray anode. In a non-monochromatized x-ray source other excitation energies like $K_{\alpha 2}$ can be present, giving rise to satellite peaks with slightly shifted binding energies compared to the main lines caused by the electron orbitals. The satellites will always be shifted to lower binding energies as the main $K_{\alpha 1}$ excitation has the highest energy.

For some materials like transition metal oxides the strong hybridization between metal-$3d$ and ligand-$2p$-states is another source for satellite structures in photoemission spectra. The $2p$-orbitals of oxygen show a strong overlap with the metal-$3d$-orbitals making a ligand-to-metal $2p$-$3d$ charge transfer very likely. Such an electron transfer will leave the system in a new electronic configuration

$$3d^n L \longrightarrow 3d^{n+1} \underline{L}, \tag{2.7}$$

where L denotes the ligand-shell-electron and $\underline{L}$ the respective hole. In the ground state the $3d^n$ configuration has the lowest energy, whereas after photoemission the influence of the core hole potential causes a rearrangement of the energy states making the $3d^{n+1}$ configuration the lowest. This is illustrated in Figure 2.4 for a system with two charge transfer states. The parameters used in the diagram will be explained in Sections 2.2 and 4.3, where the principle of charge transfer states will be picked up again as a crucial part for the theoretical calculation of photoemission spectra.
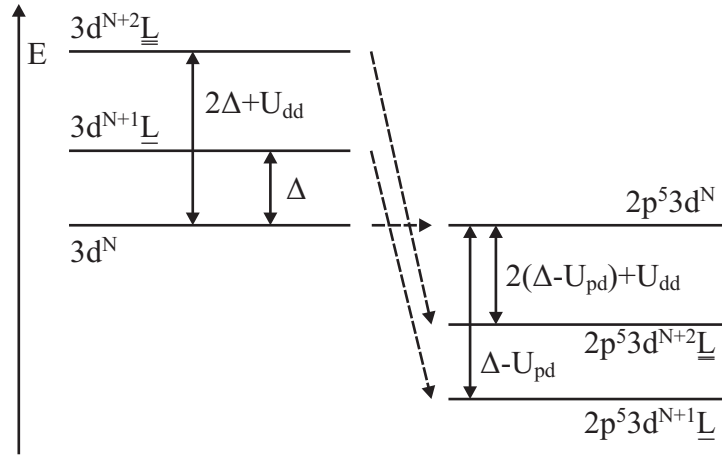
Figure 2.4: *Ordering of energy states in a 2p photoemission process for a system with two charge transfer states. In the final state (right) the ordering of the energy states is changed by the influence of additional potentials. The variables are explained in Section 4.3.*

2.1.2.3   Auger peaks

The Auger-effect is named after Pierre Auger who discovered it in the 1920s. It describes the radiation-free transition of an electron to a lower shell in the same atom. The core hole can be created, for example, by emission of a primary electron as it is the case in photoemission spectroscopy. An electron from a higher shell can occupy this free state, the energy gained by this transition to a lower shell is directly absorbed by an electron in a higher shell which is then itself emitted from the atom. If the kinetic energy of this Auger electron is high enough it can leave the solid and is detected as an Auger peak in the photoemission spectrum. The kinetic energy of the Auger electron is independent of excitation energy, it depends solely on the shells involved in the emission process. An
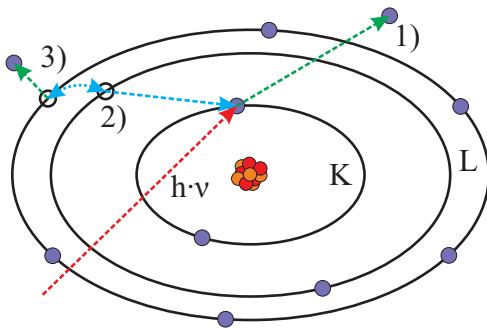

Figure 2.5: Auger *effect in photoemission spectra. The excitation energy $h\nu$ is absorbed by a primary photoelectron 1). An electron from a higher shell fills the created core hole 2). The energy gained by this relaxation can emit a third electron, the* Auger *electron, from its shell 3).*

AUGER peak is always characteristic for a specific element, the peak positions are constant regardless of the excitation energy. In photoelectron spectroscopy AUGER electrons are always detected simultaneously to the primary photoelectron, but a distinction is easy due to the different excitation energy dependencies.

AUGER peaks are labeled with three letters indicating the main quantum numbers of the shells involved in the transitions. The first letter gives the shell of the primary core hole, the second letter the initial shell of the relaxing electron, and the third letter the initial shell of the emitted AUGER electron. In Figure 2.5 the AUGER effect is shown exemplarily for a KLL-transition.

2.1.2.4   Chemical shift

The binding energy of an electron orbital is sensitive to the chemical surroundings of the atom. Differences in chemical bondings to other atoms or elements can lead to binding energy differences of the order of several eV. This effect called *chemical shift* causes additional peaks in photoemission spectra. The shift is caused by two different chemical effects. The proximity to other atoms creates an additional COULOMB-potential for each atom, and the chemical bonds to its nearest neighbors cause a dislocation of the electron orbitals in the atom. The binding energy of an electron orbital can then be expressed by

$$E_{B,sh} = E_B + E_M + K \cdot q_A. \tag{2.8}$$

Here $K \cdot q_A$ describes the dislocation of the electrons on atom A. E_M is the MADELUNG energy $E_M = \sum_B (q_B/r_{AB})$ induced by the COULOMB-potential, it is defined by the effective charge q_B of the surrounding atoms and the distance between atoms A and B.
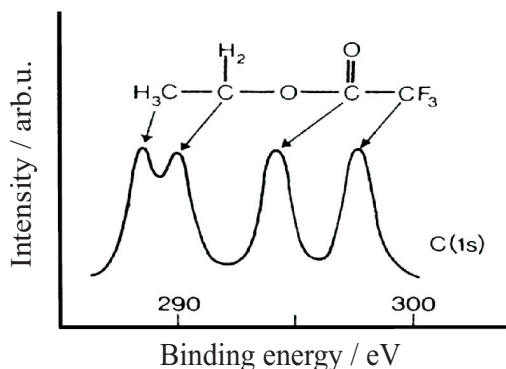
Figure 2.6: *Chemical shift in the photoemission spectrum of an organic molecule. Distinct peaks can be assigned to carbon atoms with different chemical surroundings. Taken from* [28].

Figure 2.6 shows an example of shifted binding energies for a molecule containing carbon in multiple chemical states. Atomic C has a binding energy of about 284.5 eV for the $1s$ orbital. Although the valency of C is always 4+, the $1s$ binding energy of C atoms in a methyl group CH_3 is about 10 eV lower than for a C atom in a trifluoromethyl group CF_3.

Chemical shifts can be used as a measure for the valence state of an element. By comparison with reference data a measured chemical shift can be assigned to a specific valency for an element. This is of importance for distinguishing the oxidation states of metals, for example.

2.1.2.5   Spin-Orbit coupling

Spin-orbit coupling is an important effect in photoemission spectroscopy. Two different coupling schemes between the orbital angular momentum $\boldsymbol{l}$ of an electron and its spin angular momentum $\boldsymbol{s}$ have to be considered. For light elements (around up to carbon) the RUSSELL-SAUNDERS-coupling prevails: The orbital angular moments of all electrons couple to a total orbital angular momentum $\boldsymbol{L} = \sum_i \boldsymbol{l}_i$, and all spin angular moments couple to a total spin angular momentum $\boldsymbol{S} = \sum_i \boldsymbol{s}_i$. Afterwards $\boldsymbol{L}$ and $\boldsymbol{S}$ couple to give a total angular momentum $\boldsymbol{J}$. For heavier elements the spin-orbit-interaction is much stronger than the electrostatic interaction between electrons, thus first $\boldsymbol{l}_i$ and $\boldsymbol{s}_i$ couple to a $\boldsymbol{j}_i$. Then all $\boldsymbol{j}_i$ couple to the total angular momentum $\boldsymbol{J}$. This process is called jj-coupling.

The energies of electrons with different values of $\boldsymbol{J}$ are slightly different. This causes every electron orbital with a non-vanishing orbital momentum l to emit photoelectrons with two different kinetic energies. The splitting of these peaks is characteristic for each element and orbital, it can be of the order of less than $1\,\text{eV}$ for orbitals near the FERMI-edge up to around $100\,\text{eV}$ for core levels. The two photoemission peaks induced by spin-orbit-coupling must have a fixed intensity ratio which is given by the degeneracy $2J + 1$ of the total angular momentum $\boldsymbol{J}$. For example, a $2p_{3/2}$-peak has $J_1 = 3/2$ with degeneracy 4, and a $2p_{1/2}$-peak has $J_2 = 1/2$ with degeneracy 2. This gives an intensity ratio

$$\frac{I_{J_1}}{I_{J_2}} = \frac{2J_1 + 1}{2J_2 + 1} = \frac{2}{1}. \tag{2.9}$$

For a $3d$-orbital, the ratio would be $3/2$. In measured photoemission spectra these intensity ratios are reproduced very accurately.

2.1.2.6   Quantitative analysis of photoemission spectra

In addition to a qualitative analysis to characterize the chemical state of an element, photoemission spectra can be evaluated quantitatively to investigate the ratios of different elements in a sample. For this purpose one has to compare the intensities of peaks belonging to the respective elements. The ratio between two elements is proportional to the ratio between the peak areas, but one needs to include the scattering cross section σ_i for a given orbital of a given element (cf. Section 2.1.2) and the IMFP to obtain the mass percentage of an element in a sample

$$\chi_i = \frac{A_i/(\sigma_i \cdot \lambda_i)}{\left(\sum_{i=1}^{n} A_i/(\sigma_i \cdot \lambda_i)\right)}. \tag{2.10}$$

The inclusion of σ_i assures that different probabilities for the excitation of different electron orbitals are taken into account. A suitable background must be subtracted from the peaks before calculating the areas (cf. Section 2.1.2.1).

Equation (2.10) assumes that all elements are distributed evenly in the sample, a layered structure of different materials is not taken into account. This must be kept in mind if, for example, one calculates the ratio of two materials deposited on top of each other.

2.2 Charge Transfer Multiplet Calculations

The photoemission spectra of transition metals deviate from ones expected from simple theoretical models. The reason for this is the strong influence of unoccupied states in the $3d$-orbital. This can lead to a large number of coupling effects between electron- and hole-moments on different shells. *Charge Transfer Multiplet* theory is one theoretical approach to calculate photoemission spectra with great accuracy for such materials.

The wave functions of valence orbitals like $3d$ show a strong overlap with the wave functions of core orbitals like $3s$ or $2p$. If a core electron is emitted by photoionization, the remaining core hole can be treated as a particle with reverse angular and spin momentum. The total angular momentum of the core hole $j_h = |l_h| \pm |s_h|$ then couples to the total angular momentum J_{vs} of the valence shell. If $J_{vs} = 0$ there are only the two possible orientations for the core hole which split the photoemission peak into two distinct peaks. This case is called *exchange splitting*. If the valence shell has a non-vanishing total angular momentum $J_{vs} \neq 0$, the coupling of all possible combinations of the two values must be considered. A superposition of different couplings in more than one atom leads to a multitude of final state configurations, the photoemission spectrum will contain more than just two peaks for each electron orbital. This effect is called *multiplet splitting*.

For an accurate theoretical description of a photoemission process it is not sufficient to include multiplet splittings in the calculation. As stated in Section 2.1.2.2 the effect of *charge transfer states* is also crucial. Charge transfer alters the ordering of the energy states for an electronic configuration due to the different influence of the core hole potential in the charge transfer states. A complete *charge transfer multiplet* calculation has to take all these effects into account.

The principles of such a calculation are described in [19]. The following Sections will give only a short overview of the involved quantum mechanical equations to introduce the necessary parameters. The computational realization of the calculation with all necessary steps will be discussed later in Section 4.3.

2.2.1 Atomic Multiplets

As a starting point a single atom without any exterior influence is considered. The energy states in an atom containing more than one electron are given by the atomic Hamiltonian

$$H_{atom} = \sum_N \frac{\boldsymbol{p}_i^2}{2m} + \sum_N \frac{-Z \cdot e^2}{\boldsymbol{r}_i} + \sum_{pairs} \frac{e^2}{\boldsymbol{r}_{ij}} + \sum_N \zeta(\boldsymbol{r}_i) l_i \cdot s_i. \tag{2.11}$$

The first two terms describe the kinetic energies of each electron and the electron-core Coulomb interaction. The third term is the Coulomb interaction between two electrons and the last is the spin-orbit coupling (cf. Section 2.1.2.5). Only the electron-electron interaction and the spin-orbit coupling are of importance for multiplet splitting as the

first two contributions are the same for every electron on an atomic orbital. Solving the SCHRÖDINGER equation

$$H \cdot \psi = E \cdot \psi \tag{2.12}$$

for the atomic Hamiltonian gives the elements of the transition matrix between two electronic states with the wave functions $\langle \Psi_i |$ and $\langle \Psi_f |$.

The spin-orbit coupling must apply to all electron shells with non-zero orbital angular momentum l. In the case of $2p$ photoemission for a $3d$-transition metal the relevant shells are the core shell $2p$ and the valence shell $3d$. The matrix elements of the spin-orbit coupling can then be expressed as

$$\langle 2p | \zeta_p l_p \cdot s_p | 2p \rangle \;\; \text{and} \;\; \langle 3d | \zeta_d l_d \cdot s_d | 3d \rangle . \tag{2.13}$$

Here $\langle 2p |$ and $\langle 3d |$ signify the wave functions for the electron shells $2p$ and $3d$, respectively. The interaction between spin and orbit is described by the spin-orbit coupling parameters ζ_p and ζ_d.

The matrix elements for the electron-electron repulsion are evaluated within the *central field approximation* that neglects the spherical average of electron-electron interaction and considers only the non-spherical part of the interaction. The electronic states are again expressed by wave functions of the form $\langle^{2S+1}L_J |$, the matrix elements for the electron-electron-interaction then have the form

$$\left\langle {}^{2S+1}L_J | \frac{e^2}{\boldsymbol{r}_{12}} |{}^{2S+1}L_J \right\rangle = \sum_i f_i F^i + \sum_i g_i G^i . \tag{2.14}$$

The parameters f_i, g_i, F^i and G^i are called *Slater-Condon-parameters*. They represent the direct Coulomb repulsion (F^i and f_i) and the Coulomb exchange interaction (G^i and g_i) between two electrons. Upper-case letters describe the radial part, lower-case letters the angular part of the respective interaction. This representation of the matrix elements for a two-electron wave function is very convenient as the parameter g_i is present only for electrons on different shells. This greatly simplifies the calculation of the matrix elements.

2.2.2 Crystal Field Multiplets

A *crystal field multiplet* calculation takes into account the surroundings of an atom. The energy states of the atom will be influenced by additional charges positioned on the next neighbor atoms. For the Hamiltonian this means that an additional term must be included in the calculation to describe the external charge distribution. This is done by adding a potential $\phi(\boldsymbol{r})$ to the atomic Hamiltonian

$$H_{CF} = H_{atom} - e \cdot \phi(\boldsymbol{r}) . \tag{2.15}$$

The potential $\phi(\boldsymbol{r})$ can be expressed as a series expansion of spherical harmonics Y_{LM}

$$\phi(\boldsymbol{r}) = \sum_{L=0}^{\infty} \sum_{M=-L}^{L} \boldsymbol{r}^L A_{LM} Y_{LM}(\psi, \phi) \tag{2.16}$$

which is treated as a perturbation to the atomic energy states. This means that the matrix elements of $\phi(\boldsymbol{r})$ must be expressed in terms of $\langle 3d|$ wave functions. The necessary matrix elements $\langle 3d | \phi(\boldsymbol{r}) | 3d \rangle$ can again be split into a radial and a spherical part. The radial part gives the strength of the crystal field. The spherical part can be written completely in Y_{LM} symmetry. The resulting crystal field potential reduces to

$$\phi(\boldsymbol{r}) = A_{00} Y_{00} + \sum_{M=-2}^{2} \boldsymbol{r}^2 A_{2M} Y_{2M} + \sum_{M=-4}^{4} \boldsymbol{r}^4 A_{4M} Y_{4M}, \tag{2.17}$$

other terms do not contribute in the series. This formulation already hints to the usual definition of the crystal field by the three parameters X_{400}, X_{420} and X_{220}. The indices $\{ijk\}$ result from the definition of the symmetry properties of electron orbitals in the notation of BUTLER [29]. In optical spectroscopy the crystal field is often given with the parameters Dq, Ds and Dt. These two sets are related by the conditions

$$
\begin{aligned}
X_{400} &= 6 \cdot \sqrt{30} \cdot Dq - 7/2 \cdot \sqrt{30} \cdot Dt \\
X_{420} &= -5/2 \cdot \sqrt{42} \cdot Dt \\
X_{220} &= -\sqrt{70} \cdot Ds.
\end{aligned}
\tag{2.18}
$$

A cubic crystal is assigned to the O_h symmetry group, in this case only one parameter X_{400} is relevant. Such a field can be found for example for iron atoms in a wustite structure where each iron atom is coordinated octahedrally by six oxygen atoms. In tetrahedral symmetry (D_{4h}) where one atom is in the center of a three-sided pyramid all three parameters X_{400}, X_{420} and X_{220} must be given. This is the case for example in magnetite for some of the Fe^{3+} atoms.

2.2.3   Charge Transfer Multiplets

The crystal field multiplet considers only electrons on the one atom at the centre of the calculation. As already discussed in Section 2.1.2.2 the overlap between metal-$3d$ and ligand-$2p$-orbitals can lead to a charge transfer from the ligand shell to the metal shell. A charge transfer multiplet calculation combines this effect with the atomic and crystal field multiplet effects mentioned in Section 2.1.2.2.

The ground state configuration of an atom can be written as $3d^n L$, where n is the number of electrons in the $3d$ shell and L signifies an electron in a ligand shell. The first charge transfer state then has the form $3d^{n+1}\underline{L}$. Here the underline signifies a hole in the ligand shell.

In addition to the dipole transition between initial and final state of the photoemission process these two configurations must be mixed to simulate the coexistence of both states and their influence on the photoemission spectrum. The mixing has to be calculated both in the initial and in the final states, while at the same time the dipole transitions between the respective initial and final states are calculated similar to the crystal field calculations introduced in the last Section. For instance, in an XPS $2p$ calculation with one charge transfer state this implies four distinct calculations, two dipole transitions (between initial and final states) and two monopole transitions (mixing of initial and final states, respectively). The relevant matrix elements for the mixing of the initial and final states are of the form

$$\left\langle 3d^N | H_{mix} | 3d^{N+1}\underline{L} \right\rangle \qquad \left\langle 2p^5 3d^N | H_{mix} | 2p^5 3d^{N+1}\underline{L} \right\rangle . \tag{2.19}$$

The mixing Hamiltonian can be expressed as

$$
\begin{aligned}
H_{mix} &= \sum_\nu \epsilon_\Gamma a_\nu^+ a_\nu + \sum_\nu \epsilon_{d\Gamma} a_{d\nu}^+ a_{d\nu} + \sum_\mu \epsilon_{p\Gamma} a_{p\mu}^+ a_{p\mu} + \sum_\nu V(\Gamma) \cdot (a_{d\nu}^+ a_\nu + a_\nu^+ a_{d\nu}) \\
&+ \frac{1}{2} \cdot \sum_{\nu_1,\nu_2,\nu_3,\nu_4} g_{dd}(\nu_1,\nu_2,\nu_3,\nu_4) a_{d\nu_1}^+ a_{d\nu_2} a_{d\nu_3}^+ a_{d\nu_4} \\
&+ \sum_{\nu_1,\nu_2,\mu_1,\mu_2} g_{pd}(\nu_1,\nu_2,\mu_1,\mu_2) a_{d\nu_1}^+ a_{d\nu_2} a_{p\mu_1}^+ a_{p\mu_2} \\
&+ \zeta_d \sum_{\nu_1,\nu_2} (\boldsymbol{l}\cdot\boldsymbol{s})_{\nu_1,\nu_2} a_{d\nu_1}^+ a_{d\nu_2} + \zeta_p \sum_{\mu_1,\mu_2} (\boldsymbol{l}\cdot\boldsymbol{s})_{\mu_1,\mu_2} a_{p\mu_1}^+ a_{p\mu_2} . \tag{2.20}
\end{aligned}
$$

The index ν represents a combined index (Γ, σ) of angular momentum Γ and spin momentum σ for the metal $3d$ and ligand $2p$ orbitals, respectively. μ is an equivalent index for a metal $2p$ core state. A d or p further signifies a metal $3d$ or $2p$ state. a^+ and a are electron creation and electron annihilation operators.

The first three terms in Equation (2.20) represent the metal $2p$ and $3d$ states and the ligand $2p$ states. The fourth term describes the hybridization between metal $3d$ and ligand $2p$ shells, $V(\Gamma)$ is the hybridization energy between these two states. The next two terms containing g_{dd} and g_{pd} represent all Coulomb interactions between two $3d$ electrons and between a $2p$ and a $3d$ electron, respectively. The last two terms describe the spin-orbit interactions for $2p$ electrons and $3d$ electrons with the parameters ζ_p and ζ_d.

With this Hamiltonian all possible transition matrix elements can be calculated, as a result one obtains a (relative) energy and probability for each transition. The probabilities are direct representations of the photoelectron intensity of the transition.

2.3   X-ray Diffraction

X-ray Diffraction (XRD) is an important tool to investigate structural properties of crystalline materials. The diffraction of electromagnetic waves at a crystal was postulated by MAX VON LAUE in 1912 and later demonstrated by WALTER FRIEDRICH and PAUL KNIPPING. LAUE received the NOBEL-price for his work in this field in 1914.

An electromagnetic wave falling onto a sample can interact with electrons in the sample if its wavelength is of the same order as the distances of the electrons. In a crystalline sample the electron density is centered at the atoms of the crystal, with typical atomic distances of the order of $1\,\text{Å}$. Electromagnetic waves with such a wavelength have energies around $10\,\text{keV}$. This energy region can be accessed with x-rays. The x-rays will then be scattered at the electron shells of the atoms in the sample. An amorphous sample with irregular atomic distances will result in scattered intensity over a wide range of solid angles. But if the atoms, i.e. the electron densities, are arranged periodically within the sample, constructive inference of scattered waves can occur. In this case a distinct diffraction spot can be found that is characteristic for the underlying periodicity.

For simplicity the diffraction process is usually described in reciprocal space, where the reciprocal unit cell is given by the reciprocal lattice vectors $\boldsymbol{a}^*$, $\boldsymbol{b}^*$ and $\boldsymbol{c}^*$ as

$$\boldsymbol{a}^* \,=\, 2\pi \cdot \frac{\boldsymbol{b} \times \boldsymbol{c}}{\boldsymbol{a} \cdot (\boldsymbol{b} \times \boldsymbol{c})} \quad \boldsymbol{b}^* \,=\, 2\pi \cdot \frac{\boldsymbol{c} \times \boldsymbol{a}}{\boldsymbol{b} \cdot (\boldsymbol{c} \times \boldsymbol{a})} \quad \boldsymbol{c}^* \,=\, 2\pi \cdot \frac{\boldsymbol{a} \times \boldsymbol{b}}{\boldsymbol{c} \cdot (\boldsymbol{a} \times \boldsymbol{b})}. \tag{2.21}$$

$\boldsymbol{a}$, $\boldsymbol{b}$ and $\boldsymbol{c}$ are the lattice vectors of the crystal in real space. The incident and the diffracted electron beam are expressed by their wave vectors $\boldsymbol{k}_i$ and $\boldsymbol{k}_f$ with $|\boldsymbol{k}| = 2\pi/\lambda$. The scattering process is then described by the LAUE equation

$$\boldsymbol{k}_i \,-\, \boldsymbol{k}_f \,=\, \boldsymbol{G}_{hkl}. \tag{2.22}$$

$\boldsymbol{G}_{hkl} = h \cdot \boldsymbol{a}^* + k \cdot \boldsymbol{b}^* + l \cdot \boldsymbol{c}^*$ is called the *scattering vector*, often denoted as $\boldsymbol{q}$. This equation is a 3-dimensional equivalent of the BRAGG-equation

$$n \cdot \lambda \,=\, 2d \cdot \sin\Theta, \tag{2.23}$$

where d is the distance between two neighboring atomic planes and Θ the incidence angle of the wave. For each incidence angle Θ that fulfills this equation constructive interference between diffracted waves occurs and a diffraction spot can be observed.

This work will deal only with the simplest geometry in XRD, *specular diffraction*. In this geometry the incident angle of the electromagnetic wave α_i and the angle α_f under which the diffracted intensity is detected are identical. The wave vectors $\boldsymbol{k}_i$ and $\boldsymbol{k}_f$ lie in a plane normal to the sample surface. The BRAGG-equation for this case is illustrated in Figure 2.7. At the surface of the sample the scattering centers have an infinite distance in normal direction, thus in reciprocal space the lattice points are infinitely close. This results in a diffraction rod rather than distinct spots in the direction normal to the surface.

A simultaneous uniform changing of the angles α_i and α_f results in a measurement of the diffracted intensity along the (00L) diffraction rod in reciprocal space, where L is the reciprocal lattice coordinate normal to the surface. At certain angles given by Equation (2.23) BRAGG peaks can be found. An analysis of the intensity distribution along the L-direction in reciprocal space can give information about the vertical layer distances of scattering centers in the sample.
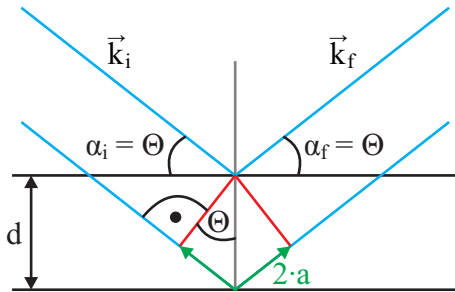

Figure 2.7: BRAGG *equation in specular diffraction geometry with incident angle* α_i *and layer distance d. Only when the path difference* $2 \cdot a$ *is an integer multiple of the wavelength of the incident electromagnetic wave with wave vector* $\boldsymbol{k}_i$ *constructive interference can occur.*

2.4 Low Energy Electron Diffraction

The diffraction of low energy electrons (LEED) has been discovered in the 1920s and is widely used for the structural characterization of crystalline surfaces since the 1960s.

The principle of electron diffraction at a surface is very similar to the diffraction of electromagnetic waves at a crystal as described for XRD in Section 2.3. Because of the low kinetic energy the electron beam interacts with atoms at the sample surface rather than with the electron shells. Diffraction can take place if the DE BROGLIE wavelength $\lambda_{deBroglie} = h/(\sqrt{2m_e \cdot E_{kin}})$ of the incident electrons is of the same order as the distance d of the scattering centers at the surface. This condition is given by the BRAGG equation

$$n \cdot \lambda_{deBroglie} = 2d \cdot \sin\Theta. \tag{2.24}$$

Here Θ is the incident angle of the electron beam. The BRAGG equation states that constructive interference is only possible if the DE BROGLIE wavelength of the incident electrons is an integer multiple of the path difference for electrons scattered at neighboring atomic layers. Typical layer distances in crystalline sample are of the order of $0.5 - 3.0\,\text{Å}$, therefore electron energies lower than $500\,\text{eV}$ are used in LEED.

LEED is very surface sensitive because the IMFP of low energy electrons scattered elastically at the surface is smaller than $10\,\text{Å}$ [21]. Therefore only the topmost $3 - 4$ atomic layers contribute to the backscattered electron intensity. In contrast to real-space-imaging techniques like *Scanning Tunneling Microscopy* (STM) or *Atomic Force Microscopy* (AFM) which can give atomic resolution on small scales, LEED images the reciprocal space. It can not detect single defects in the crystallinity, but averages the properties of a large area of the sample.

The description of the diffraction process is similar to that of XRD in Section 2.3. The only difference is that the diffraction pattern in this case is restricted to two dimensions because of the low IMFP of the electrons. The incident electron beam barely penetrates the sample surface, therefore information is restricted to the surface plane. The BRAGG equation defines the conditions for constructive interference, for LEED d is the distance of atomic rows at the surface rather than the distance of layers in a crystal as is the case in XRD. The positions of diffraction peaks are given by reciprocal lattice points where the diffraction rods of the sample surface are crossed by scattering vectors as defined by the LAUE equation (2.22). These intersection points can be found by constructing an EWALD sphere. Figure 2.8 illustrates this principle. The sample surface is defined by diffraction rods with reciprocal lattice coordinates (hk). The incident electron beam with wave vector $\boldsymbol{k}_i$ defines the EWALD sphere from which all possible diffraction spots can be obtained through their wave vectors $\boldsymbol{k}_{hk}$.

In a standard LEED optic a complete diffraction pattern is observed simultaneously on a fluorescent screen. An analysis of the distances between the diffraction spots gives a measure of the surface unit cell, the pattern itself reflects the crystal structure of the sample [31].
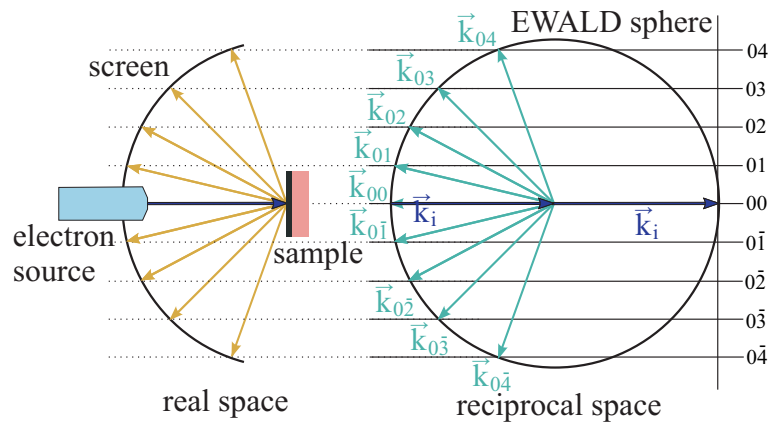
Figure 2.8: *Construction of an* Ewald *sphere in LEED. Intersections between reciprocal lattice rods and the* Ewald *sphere define diffraction spots. The indices* (hk) *denote the coordinates h and k of the reciprocal lattice rods. Taken and modified from* [30].

2.5 X-ray Reflectivity

X-ray Reflectivity (XRR) is a widely used experimental technique that allows the characterization of a thin film or of individual layers in a multilayer system. It uses the fact that the reflectivity of an interface between two materials depends on the indices of refraction of the respective materials.

An electromagnetic wave falling onto an interface between two materials (such as an air/film interface at the surface of a sample) obeys SNELL's law of refraction that describes the relation between the directions of incident and refracted beam. However, depending on the incident angle and the involved indices of refraction a part of the incident intensity is not transmitted through the interface but reflected from it. The ratio r of the reflected intensity is given by the polarization-dependent FRESNEL equations. The angles of incidence and transmittance are given by the wave vectors $\boldsymbol{k}_i$ and $\boldsymbol{k}_t$ of the electromagnetic waves.

In XRR the incident angle is varied between $0°$ and $5°$ approximately, and the reflected intensity is measured under the same angle with respect to the sample surface. A reflection occurs at every interface the electromagnetic wave hits in the sample, and the reflected waves can interfere with each other according to the BRAGG equation (cf. Section 2.3). This leads to an angle dependent distribution of reflected intensity. An analysis of this intensity distribution can give information about the thickness of the layers in the sample and about the indices of refraction of these layers. The index of refraction can then be attributed to a certain material.

In the most simple case of one layer on a substrate the reflected intensity will oscillate. Every maximum in intensity signifies a condition where the interference between waves reflected at the top and the bottom of the layer is constructive and vice versa. In this case the thickness D of the layer can be estimated to be

$$D = \frac{2\pi}{\Delta q}. \tag{2.25}$$

Here the difference of the incident angles between two intensity maxima $\Delta\Theta$ is expressed as Δq, the difference of the scattering vectors corresponding to these angles. The relation between scattering vector and angle is $q = 4\pi/\lambda \cdot \sin\Theta$.

If more than one layer is present in the sample, multiple reflections have to be taken into account as shown in Figure 2.9. The intensity transmitted at one interface is again split at the next interface and so on. The interference is then expanded to waves reflected at every interface in the sample, the resulting intensity distribution becomes more complex. The analysis of such data is discussed in more detail in Section 4.6.
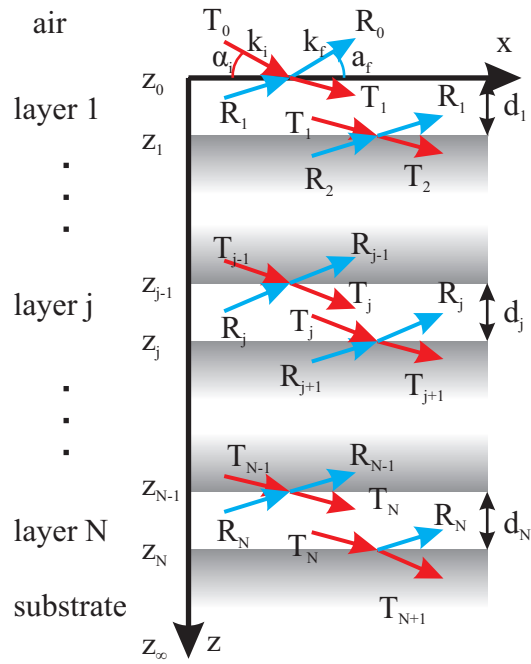
Figure 2.9: *Reflectivity for a system of N layers with air as layer 0 on top and a substrate as layer $(N+1)$ at the bottom. At each interface z_j the incident beam is split into a reflected beam R_j and a transmitted beam T_{j+1}. Multi-scattering can occur when R_j reaches the interface z_{j-1} to the layer above.*

3   Material systems

Iron oxides are promising candidates for many technical applications. This material is again easy to handle and comparatively cheap. A suitable substrate for the deposition of iron oxide films is magnesium oxide (MgO). This material has a small lattice mismatch to the most common iron oxide species. It is also easy to handle and exhibits a high thermal and mechanical stability. In addition, it is comparatively cost-effective and its large band gap makes it interesting as a model system for electrical applications with insulating substrates.

3.1   Magnesium oxide

MgO is a natural mineral that crystallizes in the Halite-structure (commonly known as rock-salt-structure) as shown in Figure 3.1. It is comprised of two equal face-centered-cubic (fcc) sublattices for Mg and O that are offset by half the O-O distance along the [001] direction. Thus each magnesium atom is octahedrally coordinated by six oxygen atoms and vice versa. The bulk unit cell has a length of $a_B = 4.21\,\text{Å}$ [32]. The surface of MgO can be described by a simple cubic unit cell of the length $a_S = a_B/\sqrt{2} = 2.982\,\text{Å}$. MgO is a non-magnetic insulator with a band gap of $7.8\,\text{eV}$ [33] and a melting point of $3125\,\text{K}$ [34]. It is transparent for wavelengths in the visible range above $300\,\text{nm}$ [35].
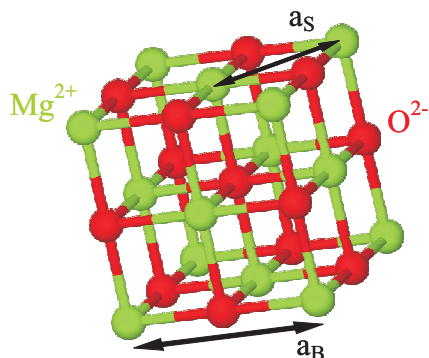

Figure 3.1: *Unit cell of magnesium oxide (MgO). Magnesium atoms (green) and oxygen atoms (red) each form fcc sublattices shifted by half the unit cell size with respect to each other. The bulk and surface unit cell vectors are indicated. Taken and modified from [30].*

3.2   Iron

Iron is a widely available $3d$-metal. It is ferromagnetic with a high CURIE-temperature of $1043\,\text{K}$ [36]. It crystallizes in three different forms. For temperatures up to $\approx 1180\,\text{K}$ the crystal structure of α-Fe is body-centered-cubic (bcc) with a lattice constant of $a_0 = 2.86\,\text{Å}$ [32]. Above that the structure changes to a fcc structure for γ-Fe, and for temperatures higher than $1800\,\text{K}$ it changes to a bcc δ-Fe [37]. In this work the temperatures are constricted to below $T = 700\,\text{K}$, so only the α-phase is of interest here. When iron is

deposited onto an MgO substrate the iron atoms adsorb on top of oxygen atoms only [32]. This results in a bcc lattice where the bulk unit cell is rotated by 45° with respect to the MgO bulk unit cell. In this way the lattice mismatch is only about 4 %.

3.3   Iron oxides

Iron is very reactive, under ambient conditions it oxidizes already at room temperature. The resulting iron oxides can be divided into three classes, Fe(II)-oxide, Fe(II,III)-oxide and Fe(III)-oxide.

Fe(II)-oxide (wustite) has the chemical formula FeO. It crystallizes in the same crystal structure as MgO with a lattice constant $a = 4.33\,\text{Å}$ [38]. The lattice mismatch to MgO is less than 3 %. The crystal structure is furthermore characterized by iron vacancies that lead to a real stoichiometry of $Fe_{1-\delta}O$. Wustite is an antiferromagnetic insulator with a NÉEL-temperature of $200\,\text{K}$ [39]. In ambient conditions it is unstable and disproportionates to metallic Fe and Fe_3O_4 [38]. As in all iron oxides the iron atoms are known to adsorb on top of the oxygen atoms of the substrate [40].
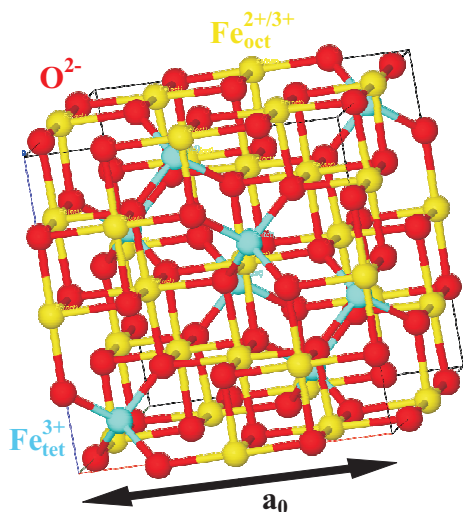
Figure 3.2: *Unit cell of the inverse spinel magnetite ($Fe^{2+}Fe_2^{3+}O_4^{2+}$). Tetrahedral sites (blue) contain only Fe^{3+} ions, octahedral sites (yellow) are randomly occupied by Fe^{2+} and Fe^{3+}. Taken and modified from [30].*

Fe(II,III)-oxide (magnetite) is a ferrimagnetic conductor with a CURIE-temperature of $860\,\text{K}$ [41]. It contains both Fe^{2+} and Fe^{3+} ions. Its chemical formula is $Fe^{2+}Fe_2^{3+}O_4^{2+}$. It crystallizes in the inverse spinel structure shown in Figure 3.2. All Fe^{2+} ions are positioned on octahedral sites whereas only half of the Fe^{3+} ions are situated on octahedral sites and the other half occupy tetrahedral sites [42]. The ions on octahedral sites are distributed randomly at RT, but at low temperatures ($T = 120\,\text{K}$) a VERWEY-transition to a rhombic structure with significantly different magnetic and electric properties [43] occurs. This process is not completely understood to date. The lattice constant of magnetite is $a_0 = 8.394\,\text{Å}$ [42] which is nearly the exact double value as for MgO, the lattice mismatch is only 0.3 %.

Fe(III)-oxides include only Fe^{3+} ions. Several different crystal structures are possible, the most common are α-Fe_2O_3 (hematite) and γ-Fe_2O_3 (maghemite).

Hematite has a trigonal crystal structure with lattice constants of $a = b = 5.034\,\text{Å}$ and $c = 13.750\,\text{Å}$ [44]. It is thus unlikely that this antiferromagnet will grow in crystalline form on MgO because of the large lattice mismatch.

Maghemite crystallizes in a spinel structure similar to magnetite. In this case the octahedral sites are occupied only by Fe^{3+} ions and vacancies ($\square$) with the effective formula $(Fe^{3+})[Fe^{3+}_{5/3}\square_{1/3}]O_4$. The lattice constant of this cubic structure is $a_0 = 8.33\,\text{Å}$ [45], which gives a lattice mismatch of $1.1\,\%$, slightly larger than for magnetite. Maghemite is a ferrimagnetic insulator at RT but converts into hematite at temperatures above $570\,\text{K}$ [46].

4 Experimental setup

All samples investigated in this work are prepared in the group "Thin films and interfaces" at the University of Osnabrück. The samples are prepared under ultra-high-vacuum (UHV) conditions and are characterized in-situ with XPS and LEED measurements. Afterwards some samples are further investigated with XRR and XRD at the synchrotron facility DESY (Deutsches Elektronen-Synchrotron) at HASYLAB in Hamburg. This section will describe the experimental setups used in Osnabrück and Hamburg and the methods used for the analysis of the data.

4.1 Ultra-High-Vacuum chamber

The UHV chamber used in this work is outlined in Figure 4.1. It consists of four chambers separated by gate valves. From the load lock the sample is transferred at first to a preparation chamber. In this chamber the substrates and, after that, the films can be prepared. The sample can be heated, several evaporators as well as a leak valve for gas inlet are available here. Using a combination of a scroll pump and a turbo pump, the base pressure in this chamber is $p \approx 1 \cdot 10^{-8}$ mbar. The third chamber contains the x-ray gun and the electron analyzer for the XPS measurements as well as the LEED optics. In addition to a scroll pump and a turbo pump an ion pump with a titanium sublimator allows for a base pressure of $p \approx 1 \cdot 10^{-10}$ mbar. The last chamber of the UHV system was used only for storage of the samples under UHV conditions in this work. The pump system is the same as in the XPS/LEED chamber, the base pressure is again $p \approx 1 \cdot 10^{-10}$ mbar.
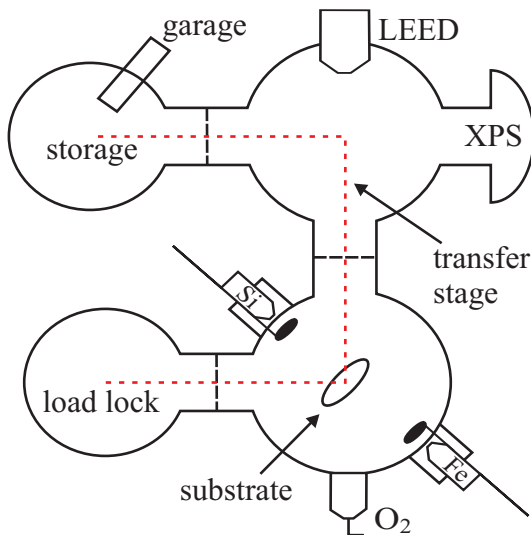

Figure 4.1: *Schematic illustration of the UHV chamber used in this work. The preparation chamber contains evaporators for iron and silicon and a leak valve to adjust oxygen pressure in the chamber. A second chamber contains the photoemission spectrometer and the electron diffraction optics. In the last chamber samples can be stored under UHV conditions.*

4.1.1 Sample preparation

MgO(001) substrates used in this work are commercially available. They have a size of $10\,\text{mm} \times 10\,\text{mm} \times 0.5\,\text{mm}$ with a miscut of $0.5°$ and are polished one-sided. Prior to the deposition of thin films the substrates are annealed at $670\,\text{K}$ for one hour to remove contaminations from the surface. To avoid the loss of oxygen in the substrate during the annealing process this is done in a $p_A \approx 1 \cdot 10^{-4}\,\text{mbar}$ O_2 atmosphere. Afterwards the substrate is cooled down to room temperature with a rate of $R = 5\,\text{K/min}$ to allow a good reordering of the surface. The quality of the substrate surface is checked by both XPS and LEED. The diffraction pattern shows a clear 1×1 reconstruction with very bright diffraction spots, indicating a high crystallinity. XPS data show only minor contaminations by carbon and argon, which is a remnant of the production process of the substrate. Both contaminations are in the range of $2 - 3\,\%$ of the total photoelectron signal.
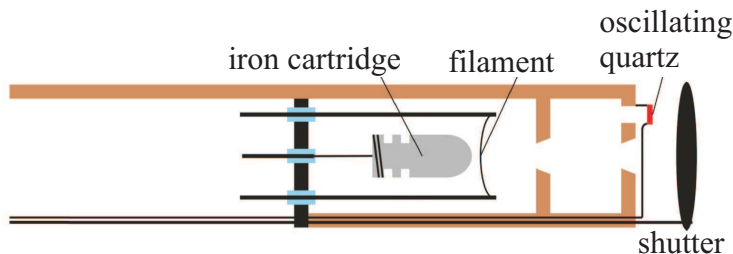
Figure 4.2: *Schematic illustration of the evaporator used in this work. Iron sublimates from a heated cartridge. The molecular beam is directed on the sample via an aperture in the casing of the evaporator. An oscillating quartz measures the amount of iron that is deposited. Taken and modified from [47].*

The thin films are prepared by molecular beam epitaxy (MBE). Figure 4.2 shows a schematic illustration of the evaporator used in this work. A positive voltage of $1000 - 1500\,\text{eV}$ is applied to an iron cartridge which is heated by electron bombardment from a tungsten filament around the cartridge. If the electric current through the cartridge is high enough, the iron starts to sublimate and forms the molecular beam which is directed through an aperture in the copper cylinder that contains the cartridge and filament. The cylinder is water cooled, which is necessary to reduce the base pressure in the chamber during evaporation. The amount of evaporated iron can be monitored by an oscillating quartz that is positioned near the center of the beam. Material deposited on this crystal will change the eigenfrequency of the crystal. This frequency change is proportional to the amount of material deposited on the crystal. By measuring the frequency change we have an indication of the amount of iron deposited on the substrate. The purity of the iron cartridge used here was $99.9\,\%$.

The substrate can be heated during evaporation. In addition to pure iron films iron oxide films can be grown by reactive growth in an oxygen atmosphere. The oxygen pressure in the chamber can be controlled by a leak valve. Alternatively pure iron films can be oxidized in an oxygen atmosphere after evaporation. It must be stated at this point that the temperature measurement on the substrate is not very exact. The design of the sample holder imposed by the design of the UHV chamber does not allow a measurement directly on the sample, rather the temperature is measured on the manipulator beside the sample holder. One would expect that the real temperature on the sample is higher than the measured one. The temperature difference between the two areas is unknown.

Before taking a sample out of the UHV system in some cases a capping layer is evaporated onto the film. In this way the films are protected from further oxidation and other contaminations from the atmosphere. For this purpose an amorphous layer of silicon is used. This has the further advantage that an amorphous film gives no signal in diffraction measurements so that investigations of the crystalline films at DESY are still possible. Si is known to oxidize easily, but silicon oxide is still amorphous and the oxidation process is restricted to a depth of 2 nm [48], thus a Si layer of at least 3 nm is enough to protect the sample. Si is evaporated similar to iron as described above. The only difference is that Si melts before it sublimates so that the raw material must be put into a small crucible inside the copper cylinder instead of a cartridge. The crucible consists of SIGRADUR®.

4.1.2 XPS

The x-ray photoelectron spectrometer is positioned in the main chamber of the UHV system. It consists of an x-ray source XR 50 and a hemispherical electron analyzer PHOIBOS 150 manufactured by SPECS® Surface Nano Analysis GmbH.
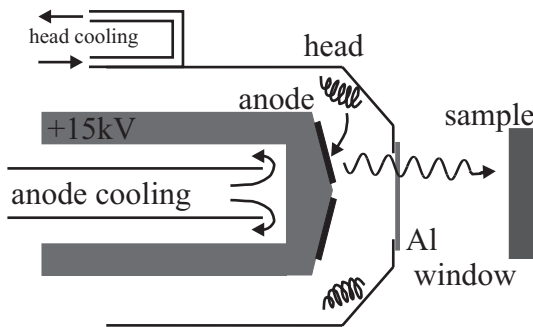

Figure 4.3: *Schematic illustration of the x-ray anode. Two different anode materials (Al and Mg) can be operated separately. The radiation is non-monochromatized.*

The x-ray source is mounted with an inclination of 35° with respect to the transfer stage of the UHV system. The source provides non-monochromatized magnesium or aluminum $K_{\alpha_{1/2}}$ radiation alternatively by using two separate anode materials (cf. Figure 4.3). Aluminum $K_{\alpha_{1/2}}$ radiation has an energy of 1486.65 eV and can be operated at $P = 400\,\text{W}$. Magnesium $K_{\alpha_{1/2}}$ radiation has an energy of 1253.64 eV and can be operated at $P = 300\,\text{W}$. In this work only the aluminum anode is used. For this source possible excitation satellites

due to $K_{\alpha_{3/4}}$ radiation should be shifted by about $10\,\mathrm{eV}$ to lower binding energy with a relative intensity of less than $7\,\%$. The source illuminates an area of about $1-2\,\mathrm{cm}^2$ of the sample.
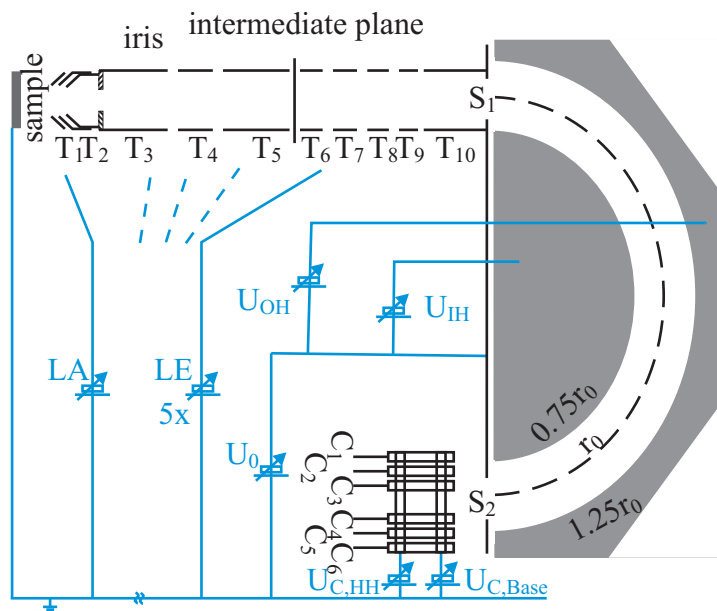

Figure 4.4: *Schematic illustration of the PHOIBOS 150 hemispherical electron analyzer. A lens system consisting of ten electrodes T_i focuses the emitted electron beam onto the entrance slit S_1. The main retardation voltage is given by $U_0 = E_{kin} + E_P + \Phi$, where E_P is the pass energy of the electrons at the entrance slit. The capacitor radius is $r_0 = 150\,\mathrm{mm}$. The electron beam is detected by a multichannel detector with six channels C_i.*

The electron analyzer is mounted normal to the transfer stage. It is shown schematically in Figure 4.4. The electrons emitted from the sample enter a lens system consisting of ten lens tubes T_i in which they are focused on the entrance slit of the electron analyzer and at the same time retarded to a pass energy E_p at the entrance slit S_1 of the analyzer. The pass energy can be set to values between $0\,\mathrm{eV}$ and $100\,\mathrm{eV}$. A higher pass energy increases the intensity of the detected photoelectrons but at the same time also increases the FWHM of the measured peaks. In this work, the pass energy was set to a medium value of $E_p = 50\,\mathrm{eV}$. The acceptance angle of the lens system is about $9°$ and the typical size of the sample spot from which photoelectrons are collected is about $0.7 \times 2.0\,\mathrm{mm}$. The photoelectron intensity is detected by a multichannel detector that consists of six channel electron multipliers (CEM). All CEMs are operated with the same detector voltage U_C. The experimental broadening of the spectrometer is given by the manufacturer to be about $1\,\mathrm{eV}$ measured at the Ag $3d_{5/2}$ peak.

The sample can be rotated normal to the plane given by the x-ray source and the electron

analyzer. In this work the detection angle is always kept at 0° with respect to the surface normal of the sample. The incident angle of the electrons is then 55°.

4.1.3 LEED

The ErLEED 150 optics is positioned in the main chamber of the UHV system. The electron energy can be varied continuously between 0 eV and 1000 eV. The diffracted electron beam creates the diffraction pattern on a transparent fluorescent screen that is centered around the electron source. The screen has a diameter of about 130 mm. The distance between the sample and the foremost grid can be reduced to $d \approx 5$ cm. The diffraction pattern is monitored by a common webcam mounted on the viewport of the unit behind the screen. Figure 4.5 shows the design of the optics schematically.
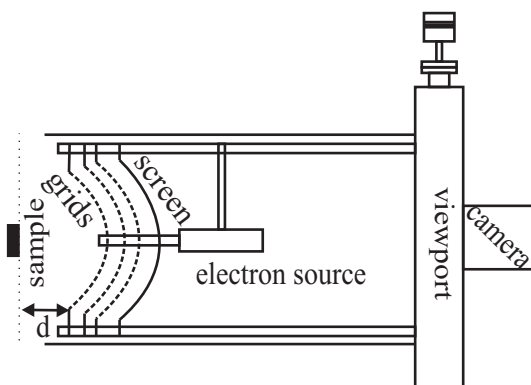
Figure 4.5: *Schematic illustration of the Er-LEED 150 optics. The diffraction pattern is viewed from behind the fluorescence screen. The distance d between sample and grids is approximately* 5 cm.

4.2 XRD and XRR measurements at DORIS III

X-ray reflection and x-ray diffraction measurements are performed at the light source DORIS III at HASYLAB in Hamburg. In this light source positrons with an energy $E = 4.45$ GeV are forced on a circular orbit by bending magnets. The constant change in direction of the positrons leads to the emission of synchrotron radiation . In this work all measurements are performed at the beamlines W1 and BW2. Both of them use a wiggler to create the synchrotron radiation. At W1 the wiggler has 32 poles, while at BW2 it has 56 poles. As the generated x-ray intensity is proportional to the number of poles, BW2 has about twice the intensity of W1. The x-ray energies of the beams are 10.5 keV at W1 and 10 keV at BW2. Both beamlines use in principle the same 6-circle diffractometer as shown in Figure 4.6. The sample is positioned at the pivot point of the diffractometer. It can be adjusted to the synchrotron beam with the translations stl and stu and the rotations sgl and sgu. The incident and detection angle are varied with om and tt.
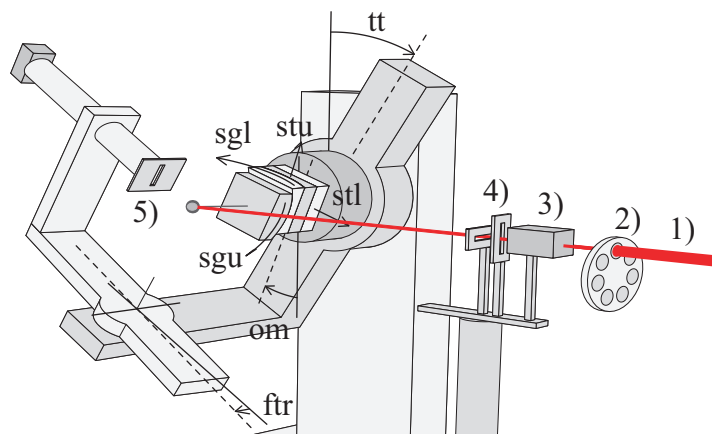
Figure 4.6: *6-circle diffractometer at beamlines W1 and BW2. The incident beam 1) is dampened by an absorber 2) before being monitored 3) for intensity calibration. A slit system 4) narrows the beam down to the desired dimensions before it hits the sample S. In front of the detector 6) the diffracted intensity is narrowed down again 5) to eliminate diffusely scattered intensity. The sample can be adjusted to the beam via the translational motors stl and stu and the rotations sgl and sgu. Different diffraction spots can be reached by the motors om, tt and ftr. Taken and modified from* [49].

4.3 Implementation of Charge Transfer Multiplet calculations

Charge transfer multiplet calculations are performed using software written by F. de Groot and E. Stavitski as described in [19]. The calculation is done in three steps. The first step is to compute the pure atomic multiplet spectrum. The only input parameter here is the atomic number and the transition one wants to examine, for example $2p^6 3d^8 \Rightarrow 2p^5 3d^8$ for a $2p$ photoemission spectrum of $_{26}Fe^{2+}$. The software calculates all electronical transitions that are possible with their strengths and relative energies. An absolute value for the energy of a transition can not be computed, this means that all theoretical spectra calculated with this method need to be calibrated to some known energy value. Comparison with other theoretical approaches to multiplet calculations has shown that the Slater-Condon-parameters calculated in this step need to be reduced to about 80% of their atomic value for the next steps in the calculation [50].

The output of the atomic multiplet calculation is then taken as input for a crystal field multiplet calculation. Here one assumes a cluster consisting of a single metal ion surrounded symmetrically by atoms of another element. The only new input parameter is the strength Dq of the crystal field created by the surroundings. Dq is defined as the energy splitting between the $3d$ e_g and t_{2g} orbitals under the crystal field. In an octahedral crystal field (O_h symmetry; six atoms positioned each along a Cartesian axis with the ion in the center)

Dq has a positive value, the e_g orbitals are higher in energy than the t_{2_g} orbitals. In a tetrahedral crystal field (D_{4h} symmetry; four atoms forming a three-sided pyramid with the ion in the center) the sign of Dq is inversed because here the e_g orbitals are lower in energy than the t_{2_g} orbitals. In addition to the crystal field strength the symmetry behavior of the electron orbitals under the influence of the crystal field must be given at this point. The incorporation of a crystal field leads to a lowering of the crystal symmetry (from simple atomic symmetry to cubic symmetry or further to tetrahedral symmetry). The change in the symmetry properties of the electron orbitals must be given as branching series from the initial spheric symmetry to the new symmetry, expressed in the notation of BUTLER [29]. This information can be determined by applying group theory [19]. The software now recalculates the elements of the transition matrix obtained in the first calculation step for the new crystal symmetry.

The last step in the calculation is now the inclusion of charge transfer states. In the case of XPS at least two charge transfer states are needed to describe a photoemission spectrum, as will be demonstrated in Section 6. This means that, for example, in the case of maghemite with Fe^{3+} clusters, three initial states ($2p^6 3d^5$, $2p^6 3d^6 \underline{L}$ and $2p^6 3d^7 \underline{L}^2$) and three final states ($2p^5 3d^5$, $2p^5 3d^6 \underline{L}$ and $2p^5 3d^7 \underline{L}^2$) are considered for the mixing. The parameters needed in this step are Δ, U_{dd}, U_{pd} and T. U_{dd} and U_{pd} are the COULOMB interactions between two $3d$ electrons and between one $3d$ electron and a $2p$ core hole, respectively. Both of them are included in g_{dd} and g_{pd} in Equation (2.20). For XPS it is commonly assumed that U_{pd} is slightly larger than U_{dd}, the values are taken to be in the range $5-10\,\mathrm{eV}$. The charge transfer energy Δ is defined by

$$\Delta \equiv E[3d^{N+1}\underline{L}] - E[3d^N] \tag{4.1}$$

where the energies are averaged for the configurations. With this definition one can formulate correlations between the averaged energies and the parameters mentioned above

$$
\begin{aligned}
\Delta + U_{dd} &= E[3d^{N+2}\underline{L}^2] - E[3d^{N+1}\underline{L}] \\
\Delta - U_{pd} &= E[2p^5 3d^{N+1}\underline{L}] - E[2p^5 3d^N] \\
\Delta + U_{dd} - U_{pd} &= E[2p^5 3d^{N+2}\underline{L}^2] - E[2p^5 3d^{N+1}\underline{L}].
\end{aligned}
\tag{4.2}
$$

The parameters and relations given here have already been illustrated in Figure 2.4, which explains the significance of charge transfer for photoemission spectroscopy. The last parameter T is the hybridization energy $V(\Gamma)$ from Equation (2.20). In an octahedral crystal field the $3d$ orbitals split into e_g and t_{2_g} orbitals separated by the crystal field Dq. The hybridization is in this case given by two parameters $T(e_g)$ and $T(t_{2_g})$. A tetrahedral crystal field induces a further splitting $e \Rightarrow a_1, b_1$ and $t_2 \Rightarrow b_2, e$. As mentioned above, here the former e orbitals are lower in energy. The charge transfer energy Δ and the hybridization energy T are typically $\approx 1-3\,\mathrm{eV}$.

To obtain the final result the software now has to perform seven calculations: three dipole transitions between the initial and final states in the three charge transfer configurations,

and four monopole transitions between the first and second and between the second and third configuration in the initial and final state, respectively. The result of this full multiplet calculation at this point is a stick spectrum of transition energies with their respective strengths for a single cluster with one ion.

Each stick spectrum must now be calibrated to a known energy value for the considered orbital. This introduces a certain error as experimental values describe a complete solid, not distinct clusters of single ions, so one must choose the energy values very carefully. Each cluster spectrum then has to be broadened artificially to imitate the lifetime and instrumental broadening in a real measurement. This is usually done by applying a combined Lorentzian-Gaussian function to the sticks. Again, this is a source for errors as the experimental line shapes can not be accurately known. As a last step all cluster spectra needed for a certain solid must be summed up to obtain the final theoretical multiplet spectrum. For instance, for maghemite one needs two clusters of Fe^{3+}, one with octahedral and one with tetrahedral symmetry, the ratio between the two being 5:3 (cf. Section 3.3).

4.4 Analysis of XPS data

Prior to any analysis satellites due to non-$K_{\alpha_{1/2}}$-radiation are subtracted from the experimental spectra. Afterwards all photoemission spectra have to be energy-calibrated. The substrate used in this work is an insulator, therefore under x-ray illumination the sample will become positively charged because there is no sufficient electron flow to balance the electron emission. The positive charge creates an additional potential for every electron orbital, which increases the measured binding energies. By setting the binding energy of a measured photoemission peak to its literature value, this effect can be partially compensated. This also applies to the thin metal films prepared in this work because the films often do not have sufficient electrical contact to the sample holder. As a reference point in this work the binding energy for the oxygen $1s$ peak of $530\,\mathrm{eV}$ was used. The energy shift due to charging was about $10\,\mathrm{eV}$. This calibration method assumes that all electron orbitals are effected evenly by the charge potential. In reality the shift of binding energies is slightly different for each orbital, therefore a precise binding energy for a given orbital can not be obtained. A related problem is the splitting of peaks due to inhomogeneous charging of the sample surface. Thus, for a quantitative analysis of XPS data one needs to be very careful with the assignment of a peak to respective electron orbitals. In addition, the splitting caused by charges may lead to an overlap of peaks that otherwise would be separated, leading to additional intensity in some peaks that should be counted for another peak. The combination of peak shifts and splittings causes an uncertainty for the energy calibration that strongly affects the analysis of photoemission spectra. Figure 4.7 shows an example of this effect. The residual oxygen $1s$ peak on a conductive silver substrate (black line) is completely regular, while on an insulating MgO substrate (blue line) the peak is split by about $10\,\mathrm{eV}$.

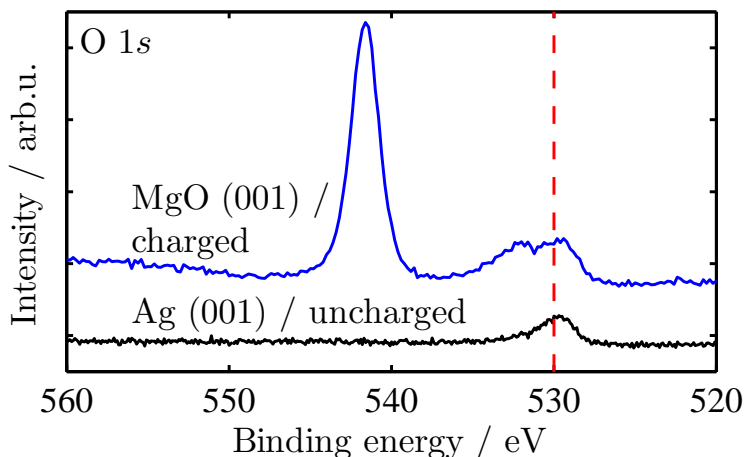The next step in the analysis of photoemission spectra is the subtraction of a suitable

Figure 4.7: *O 1s photoemission spectrum of residual oxygen on Ag (100) (black line) and of MgO (100) (blue line). The literature value for the O 1s peak is indicated by a dashed red line. The spectrum of the conductive material is not shifted, while the spectrum of the insulator is shifted and splitted.*

background from the measured intensity as discussed in Section 2.1.2.6. In this work a background of the SHIRLEY type is applied to all XPS data. Although not theoretically sound, this is widely accepted in literature and has the advantage of not requiring any new parameters. The energy interval chosen for a peak plays an important role in the quantitative analysis because the background intensity is very sensitive to the boundary points of the interval. A deviation of a few data points ($\approx$ meV) can lead to a difference in the background intensity of about 5% due to the noise on the signal intensity. This directly influences the resulting peak area for an element.

By comparing the processed data and the calculated multiplet spectra one can now determine the composition of the iron oxide samples. All spectra are normalized to the integrated peak intensities to allow a direct comparison between experiment and theory. A weighed summation of the calculated spectra is fitted to the experimental spectrum by adjusting the ratios of the individual oxide species in the summation. The best fit to the experimental data thus gives the ratios of the oxide species in the sample.

4.5   Alternative method of fitting photoemission spectra

In order to control the results of the fitting method described in the last Section they have to be checked against other methods with reliable results. For this purpose the same samples have been analyzed previously in this group by a different approach to the

analysis of photoemission spectra. In [51] the same experimental data as in this work were at first compared to reference spectra containing only Fe^{2+} or Fe^{3+} ions. Here the reference spectra of Fe_2SiO_4 (pure Fe^{2+}) and α-Fe_2O_3 (pure Fe^{3+}) from [52] were used. Afterwards, the spectra identified to best resemble the literature data were taken as new reference spectra for the fitting of all other photoemission measurements. A similar procedure has already successfully been used in [53]. Figure 4.8 shows the experimental spectra (left) that were in this way identified as our new reference spectra for the iron ions. They are in good agreement with the original reference spectra of the single-valency iron compounds (right).
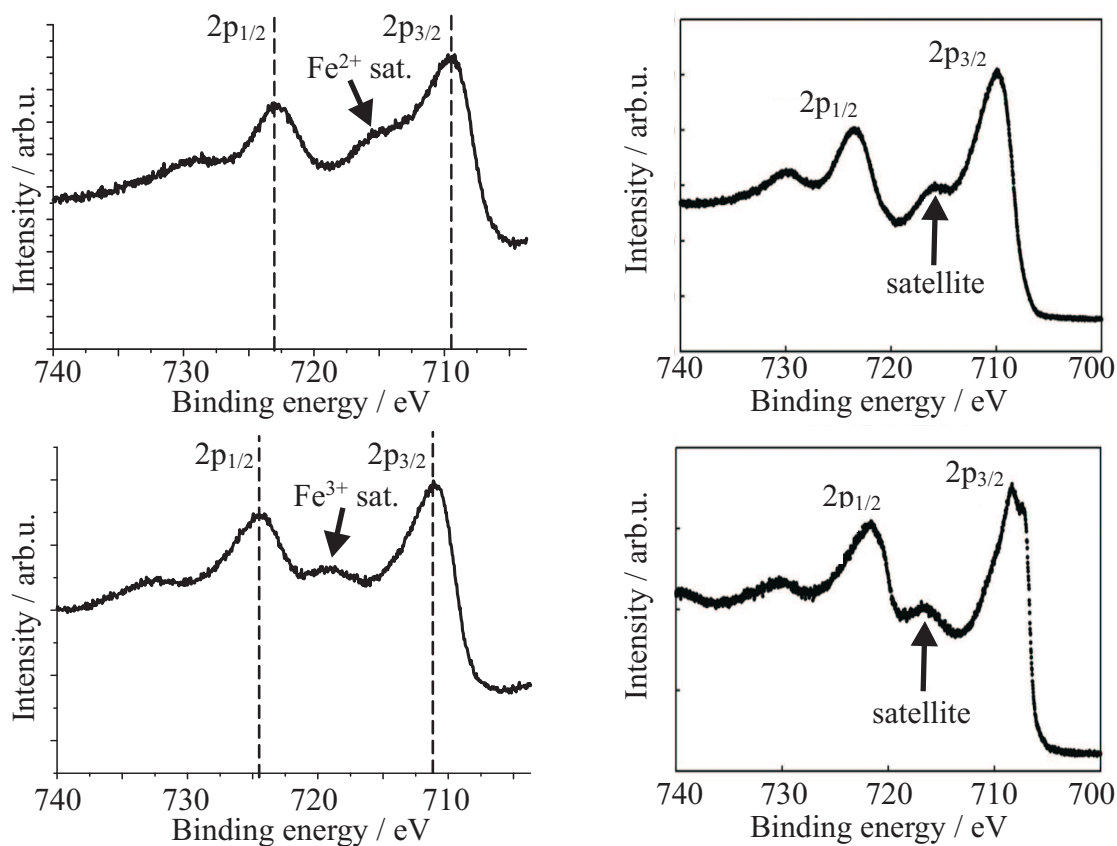
Figure 4.8: *Experimental Fe 2p reference spectra for Fe^{2+} (top left) and Fe^{3+} (bottom left) obtained in [51]. The spectra show good agreement to literature spectra of Fe_2SiO_4 (top right) and Fe_2O_3 (bottom right) from [52].*

With the help of the new reference spectra for Fe^{2+} and Fe^{3+} the composition of our samples at all preparation steps was then analyzed. The fitting algorithm is already described in the last Section. A weighted summation of the individual reference spectra was adjusted to the experimental data by a least-squares-fit of the ion ratios in the summation. In this way the ratios for the best agreement between the references and the experimental data were obtained.

In this work the same approach is adjusted again. The reference spectra are no longer experimental data of single-valency compounds but are taken from the multiplet calculations for each oxide species instead. An agreement between the values obtained in this work and the reference values would prove that the calculations are an appropriate way to describe the sample. In the following Sections ion ratios labeled "reference" always refer to the method described in this Section as performed in this group [51].

4.6   Calculation of XRR data

XRR data are used to obtain values for the thickness of the films prepared in this work. As stated above in Section 2.5, for the simplest case of only one layer on a substrate the layer thickness D can be approximated by

$$D = \frac{2\pi}{\Delta q},\tag{4.3}$$

where Δq is the difference of the scattering vector for two neighboring maxima of the reflected intensity.

Another approach to the analysis of XRR data is fitting the data with theoretical calculations. This is also done here using the software *iXRR* described in [54]. The software is based on an algorithm proposed by PARRATT (cf. Section 2.5). The user can simulate a system with any number of layers and, if needed, columns with different layer properties for species coexisting laterally. Each layer has four parameters that can be edited: the index of refraction, given by the dispersion δ and the absorption β, the layer thickness D and the roughness σ of the top surface of the layer. The software then calculates the reflectivity of the system and compares it to an imported data set. By variation of the four parameters within the limits given by the user the agreement between calculation and experiment can then be optimized. For this purpose the software offers three different algorithms of which in this work only the *differential evolution* algorithm was used. This algorithm belongs to the class of evolutionary algorithms, details are described in [55].

4.7   Analysis of XRD data

XRD data in this work consist of measurements in Θ-2Θ-geometry along the L direction of the reciprocal space, which is normal to the sample surface. The measured intensity profiles are analyzed by assigning a Lorentzian function to substrate peaks and Gaussian functions to peaks created by the film. This distinction is caused by the infinite thickness of the substrate compared to the film. Afterwards the superposition of all functions is fitted to the data. In this way the position of every peak can be obtained from the position of the maximum of its function. By comparing the values for the film peaks to the one for the substrate peak, one can calculate the vertical layer distance of the film as $d = d_{MgO}/L$

where L is the position of the peak in reciprocal space units. The vertical lattice constant of the film is then simply $n_l \cdot d$ with n_l layers per unit cell.

This method is a very simple way capable only of providing values for the vertical lattice constant of crystalline films. It is applicable only when the intensity profiles do not show intensity oscillations (fringes) near to the substrate peak caused by interference of waves diffracted at neighboring atomic layers in the sample. The existence of these fringes hints to a homogeneous film thickness. If fringes in the XRD data are not neglectable a more sophisticated analysis using theoretical formula for the calculation of XRD profiles can be performed. In this work the software *RodsNPlots* described in [56] was used for this purpose. It is very similar to the software for XRR analysis described in Section 4.6 as both are based on the same source code [57]. The sample can be modeled by a system of different layers each with a set of parameters the user can adjust. The software calculates the theoretical diffraction profile for the model, then the parameters of the model can be optimized to fit the experimental data. The most interesting parameters obtained from this analysis are the vertical layer distance and the number of atomic layers in the sample.

4.8 Samples investigated in this work

In the course of this work iron oxide films were prepared using different parameters. A first set of samples consisted of films of pure iron deposited on MgO(001) substrates at room temperature (RT). Afterwards the films were treated in an 1×10^{-6} mbar oxygen atmosphere at different sample temperatures. Several such treatments, each lasting 60 minutes, were performed on each sample. One treatment in oxygen corresponded to an exposure of 2.7 kL. After completion of these oxidation treatments some samples were annealed at different temperatures without oxygen. The annealing steps also lasted one hour each. After each step XPS and LEED measurements were performed.

A second set of samples consisted of iron oxide films where iron was deposited under an 1×10^{-6} mbar oxygen atmosphere at different substrate temperatures. These samples were also investigated by LEED and XPS after the preparation process.

If possible, the samples were capped with an amorphous layer of silicon before being taken out of the UHV chamber. Table 4.1 gives an overview over the investigated samples. The first four samples are iron films oxidized after deposition, the other four samples have been prepared by reactive deposition in oxygen atmosphere. In the second column the substrate temperature during the deposition of iron is given. The temperature of the film during oxidation is given in the fourth column.

sample	evaporation temp. (°C)	oxygen exposure (kL)	oxidation temp. (°C)	annealing steps	annealing temp. (°C)	Si cap
1	RT	10.8	RT	3	1×200, 2×300	yes
2	RT	13.5	100	7	1×200, 6×300	no
3	RT	16.2	200	-	-	no
4	RT	13.5	300	-	-	no
5	RT	-	-	-	-	yes
6	100	-	-	-		yes
7	200	-	-	-	-	no
8	300	-	-	-	-	yes

Table 4.1: *Overview of the samples investigated in this work. For the samples 1 to 4 iron films were oxidized after deposition, for the samples 5 to 8 iron was deposited reactively in oxygen atmosphere.*

5   Experimental results

This Section will present the experimental results obtained in this work. The first chapter deals with the investigation of the crystal properties by XRR and XRD. Afterwards the photoemission data and the multiplet calculations that give insight into the chemical state of the films during the oxidation process are presented. Finally the LEED results and the investigations on sample annealing are presented.

5.1   Characterization by XRR and XRD

As mentioned before all synchrotron measurements are performed at the beamlines W1 and BW2 of the DORIS III synchrotron at HASYLAB in Hamburg with energies of $10.5\,\text{keV}$ and $10\,\text{keV}$, respectively. If possible the samples have been capped by an amorphous Si layer to preserve the film properties after removal from UHV. It must be noted at this point that the following XRR and XRD data describe only the final state and composition of the samples, all other steps of oxidation or annealing are not accessible by XRR or XRD.

The film thickness is evaluated by XRR. Considering the amount of iron used in the preparation of the films, it is expected that the iron film oxidized at RT is the thinnest with only $1750\,\text{Hz}$ as read from the oscillating quartz of the evaporator. The four samples deposited in oxygen atmosphere should be about fourty percent thicker ($2500\,\text{Hz}$). The iron films oxidized at $100\,^{\circ}\text{C}$, $200\,^{\circ}\text{C}$ and $300\,^{\circ}\text{C}$ should be the thickest with $5000\,\text{Hz}$. This tendency is reflected by the experimental data in Figure 5.1. Here the results for the samples oxidized at RT, $100\,^{\circ}\text{C}$ and $200\,^{\circ}\text{C}$ and deposited reactively at RT are compared. It can be seen that the two samples treated at RT show very narrow intensity oscillations superimposed on larger oscillations. The narrow oscillations are caused by the Si capping layer that is very thick compared to the films. The other two samples are not capped by a Si layer. The periodicity corresponding to the films is indicated by vertical lines. The values $\Delta q \approx 0.13\,\text{Å}^{-1}$, $\Delta q \approx 0.082\,\text{Å}^{-1}$ and $\Delta q \approx 0.037\,\text{Å}^{-1}$ for the sample oxidized at RT, deposited reactively at RT and oxidized at $200\,^{\circ}\text{C}$ are obtained from the data. The irregularity of the oscillations for the sample oxidized at $200\,^{\circ}\text{C}$ suggests that the film is composed of parts with slightly different thicknesses. This can be taken into account by a detailed analysis described below. The values obtained for the scattering vectors here correspond to film thicknesses of $D \approx 48\,\text{Å}$, $D \approx 77\,\text{Å}$ and $D \approx 170\,\text{Å}$. These values agree reasonably well with the expectations stated above. XPS results further support the obtained values (cf. Section 5.2.4). For the sample oxidized at $100\,^{\circ}\text{C}$ oscillations are too weak to estimate a layer thickness. The similar deposition parameters of the samples oxidized at $100\,^{\circ}\text{C}$ and $200\,^{\circ}\text{C}$ suggest a similar film thickness. But because of the additional annealing performed with the former, it is assumed that this sample is slightly thinner than the one oxidized at $200\,^{\circ}\text{C}$. This is confirmed by a lower intensity of the photoemission peaks of the film oxidized at $100\,^{\circ}\text{C}$. The sample oxidized at $300\,^{\circ}\text{C}$ was not investigated by either XRR or XRD, but the deposition parameters and the photoemission intensity

suggest a film thickness similar to the sample oxidized at 200 °C.
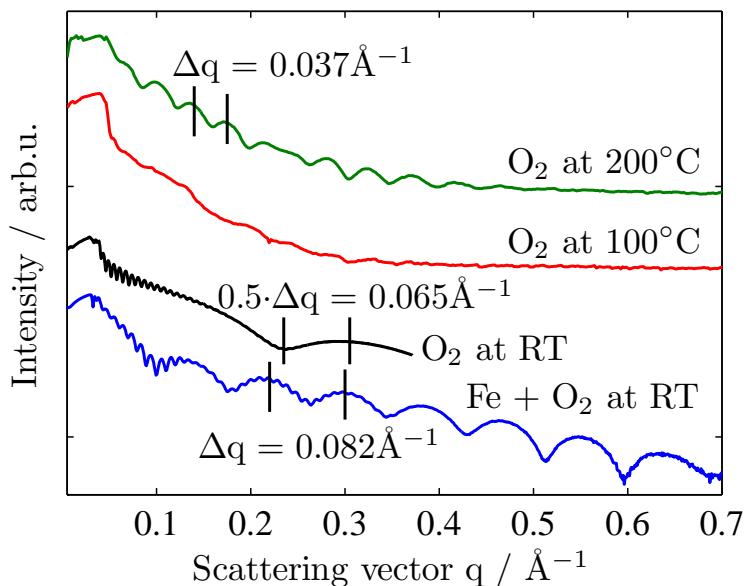
Figure 5.1: *XRR results for the samples deposited reactively at RT, oxidized at RT, oxidized at 100 °C and oxidized at 200 °C (from bottom to top). The periodicity corresponding to the film thickness is indicated by vertical lines.*

The four films deposited in oxygen atmosphere are expected to have similar thicknesses. The results for these samples are shown in Figure 5.2. The absence of a capping layer is observable for the sample prepared at 200 °C by the lack of small intensity oscillations. With increasing temperature the intensity oscillations of the films become more uneven, hinting at a varying thickness in the film. At 300 °C intensity oscillations caused by the film thickness can not be observed anymore, but a comparison of the photoemission intensity confirms that similar amounts of Fe are present on the all substrates. For the sample prepared at 100 °C the periodicity is obtained as $\Delta q \approx 0.085\,\text{Å}^{-1}$, for the sample prepared at 200 °C the periodicity is $\Delta q \approx 0.084\,\text{Å}^{-1}$. These values correspond to a thickness of $D = 74\,\text{Å} \pm 1\,\text{Å}$. This is in good agreement with the expectations and the estimation for the sample prepared at RT mentioned above.

The values estimated above for the thickness of the films are supported by the results of a more detailed analysis based on the PARRAT algorithm (cf. Section 4.6). For this method the interface roughness is described by a NEVOT-CROCE factor. Figure 5.3 shows the fitting of a calculated reflectivity (red lines, bottom) to the x-ray reflectivity data (blue lines, top) for the iron film oxidized at RT (left) and for the film oxidized at 200 °C (right). The small oscillations in the data are again caused by the very thick silicon capping layer. The large oscillation is caused by the oxide film thickness. For the iron film oxidized at
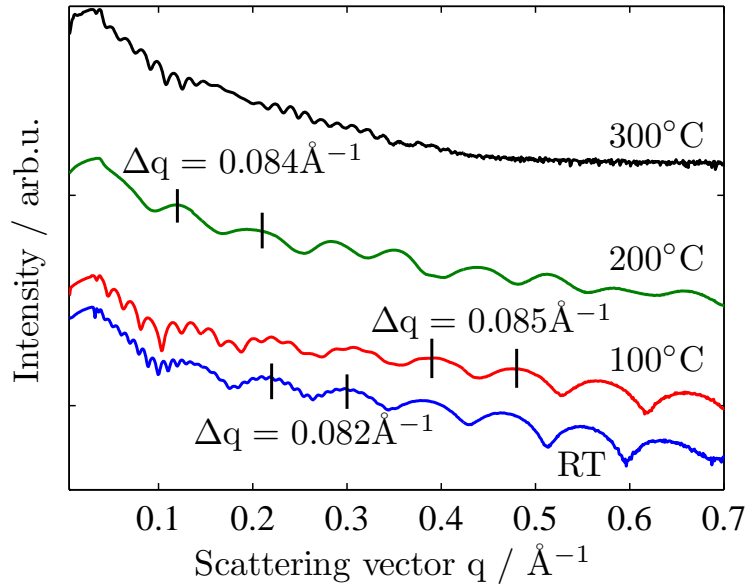
Figure 5.2: *XRR results for the samples deposited reactively in oxygen atmosphere at RT, 100 °C, 200 °C and 300 °C (from bottom to top). The periodicity corresponding to the film thickness is indicated by vertical lines.*

RT the film thickness is evaluated to be $D = 28\,\text{Å}$. The sample oxidized at 200 °C exhibits very irregular oscillations, therefore in this case two columns of iron oxide with slightly different thicknesses had to be used in the model. The resulting average thickness is about $D = 134\,\text{Å}$. For the samples deposited reactively in oxygen atmosphere values of around 70 Å have been obtained (not shown here). These values correspond well to the preparation parameters and the estimated values given above.

XRD data are used to determine the vertical lattice constants corresponding to crystalline parts of the samples. The specular diffraction rod (00L) is calibrated to the vertical layer distance of the substrate MgO(001). Sharp diffraction spots for MgO can therefore be seen at integer L-values. Additional diffraction spots for the film are expected close to the substrate spots because all iron oxides relevant in this work have only a small lattice mismatch to MgO. Figure 5.4 shows linescans in L-direction of the (001) and (002) diffraction spots for the sample oxidized at 100 °C. The experimental data are given by blue lines. Two individual functions are necessary to obtain an acceptable fit to the data. One belongs to the diffraction spot of the substrate (red line) and one additional peak, created by the film, is indicated by a green line. This spot has a smaller L-value than MgO, indicating a larger vertical layer distance in the film. At the (001) diffraction spot the position of this additional peak is $L = 0.9954$, at the (002) diffraction spot the position is $L = 1.984$. The measured peak positions can be converted to a vertical layer distance
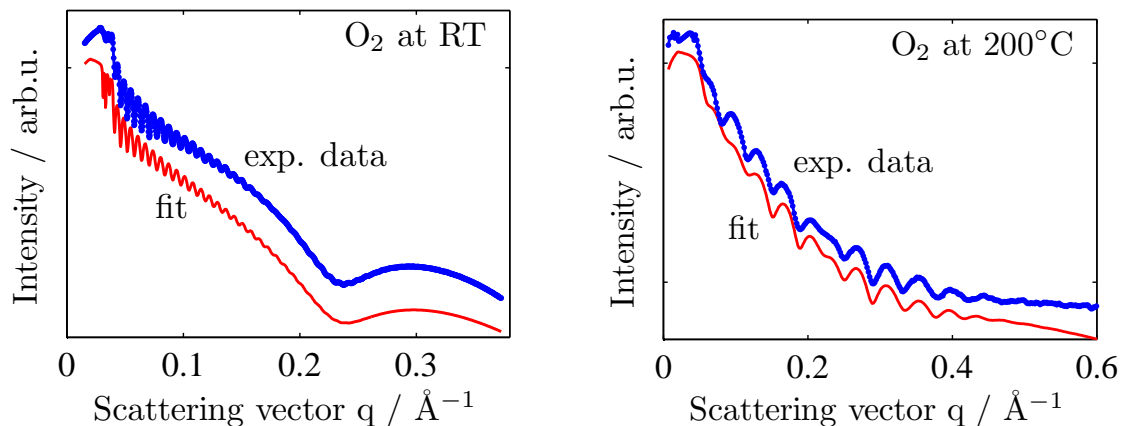
Figure 5.3: *Fitting of XRR results for the samples oxidized at RT (left) and 200 °C (right). The calculated intensity (red lines) matches the experimental data (blue lines) reasonably well.*

for the film. In this case the spot positions convert to the vertical layer distance $d = 2.122\,\text{Å} \pm 0.004\,\text{Å}$. Considering the unit cells possible for the different iron oxide species, such a value is closest to the one expected for a wustite structure, where the layer distance would be $2.165\,\text{Å}$. In the spinel structure the layer distance would have to be slightly smaller than for MgO, which is not the case here. It follows that the bulk unit cell observed in this sample has a vertical lattice constant of $a_0 = 4.245\,\text{Å} \pm 0.008\,\text{Å}$ measured at the (001)- and (002) diffraction spots.
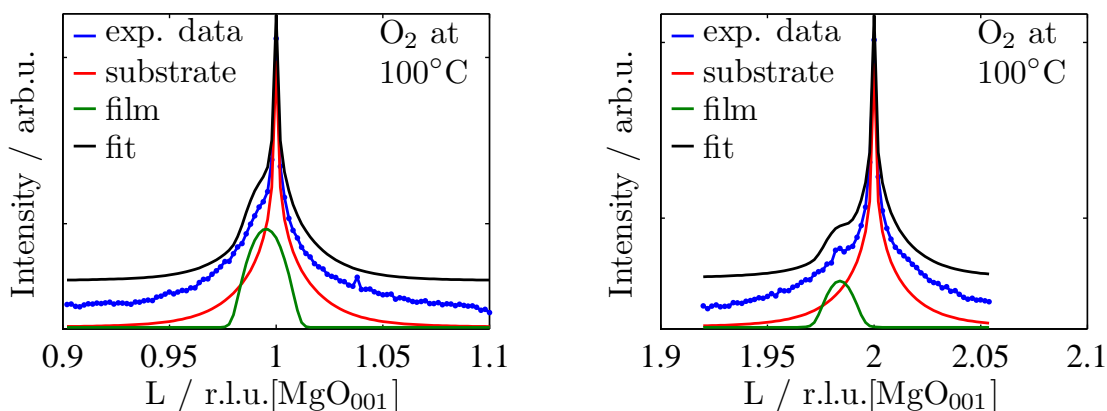
Figure 5.4: *XRD results of the (001) and (002) diffraction spots for the sample oxidized at 100 °C. The blue line represents the experimental data, the red line the substrate spot and the green line the film spot. The resulting intensity (black line) matches the experimental data well.*

In Figure 5.5 the same linescans for the sample oxidized at 200 °C are shown. In this

case one additional peak (green line) to the right of the substrate peak (red line) can be seen. The measured peak positions are $L = 1.006$ and $L = 2.016$. The corresponding vertical layer distance is $d = 2.095\,\text{Å} \pm 0.003\,\text{Å}$. This layer distance is smaller than that of the substrate, which can only be the case if the film consists of either maghemite or magnetite. Both of these oxides have layer distances slightly smaller than MgO. Therefore it is assumed that the peaks are higher-order diffraction spots from one of these oxide species. With this assumption the peak positions convert to the vertical lattice constant $a_0 = 8.379\,\text{Å} \pm 0.01\,\text{Å}$. These values are indeed close to the values for magnetite $8.39\,\text{Å}$ and maghemite $8.33\,\text{Å}$.

Both samples presented here show only weak fringes near the diffraction spots. The fringes are slightly stronger for the sample prepared at $200\,°\text{C}$. This indicates that the thickness of the oxide films is rather inhomogeneous. The XRR data presented above agree with this as the oscillations of the film thickness in these cases are irregular.
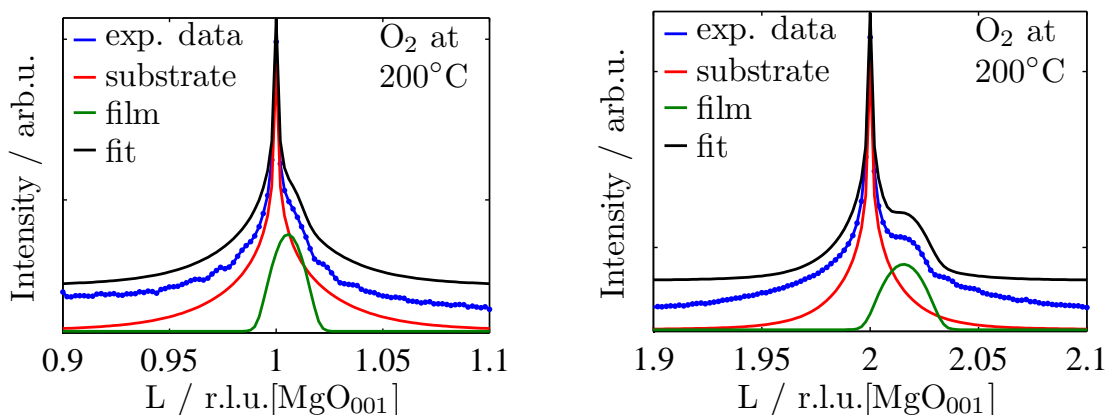
Figure 5.5: *XRD results of the (001) and (002) diffraction spots for the sample oxidized at $200\,°\text{C}$. The blue line represents the experimental data, the red line the substrate spot and the green line the film spot. The resulting intensity (black line) matches the experimental data well.*

The sample oxidized at RT does not show any additional peaks close to the substrate (001) and (002) diffraction spots (not shown here). This suggests that there is no crystalline order within this iron oxide film.

The four samples deposited in oxygen atmosphere exhibit strong fringes close to the diffraction spots. In these cases the data are therefore analyzed by using theoretical formula for the diffraction process as described in Section 4.7. The results are shown exemplarily in Figure 5.6 for the (001) diffraction spots of the samples deposited in oxygen atmosphere at $100\,°\text{C}$ and at $200\,°\text{C}$. It should be noted that the model used for the calculations is kept very simple with only one oxide layer on the substrate. The actual film may exhibit a more complicated structure, but as all experimental data are calibrated to the substrate, obtained values for layer distances can be used to characterize the film.
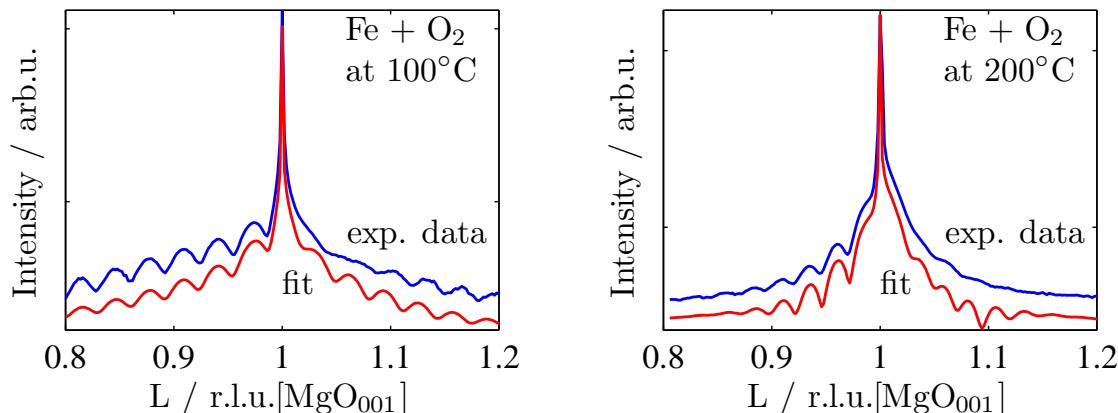
Figure 5.6: *XRD results for the (001) diffraction spots of the samples deposited reactively in oxygen atmosphere at* 100 °C *(left) and at* 200 °C *(right). The calculated intensity (red lines) matches the experimental data (blue lines) reasonably well.*

The results for the vertical layer distances of the films are given in Figure 5.7. The values are $d = 2.115$ Å, $d = 2.120$ Å and $d = 2.088$ Å for the samples prepared at RT, 100 °C and 200 °C, respectively. At 300 °C the film peak is too near the substrate peak to allow a useful analysis of the layer distance. In this case a probable range for the layer distance of the film is given. For temperatures below 200 °C the films exhibit a layer distance larger than MgO, while at 200 °C the value is smaller than for the substrate. Together with the number of layers obtained from the fitting we obtain film thicknesses of $D = 76.1$ Å, $D = 65.7$ Å and $D = 77.3$ Å, which agree well with the value $D = 74$ Å obtained by XRR for the film grown in oxygen atmosphere at RT. The viability of these results can be checked by estimating the film thickness from the distance between two fringes as $D \approx \Delta L / d_{MgO}$. The values obtained in this way are $D \approx 70.3$ Å, $D \approx 65.9$ Å and $D \approx 84.4$ Å, confirming the results of the calculations. This analysis can also be applied to the sample deposited at 300 °C, which shows clear fringes near the substrate spot although XRR showed no periodicity
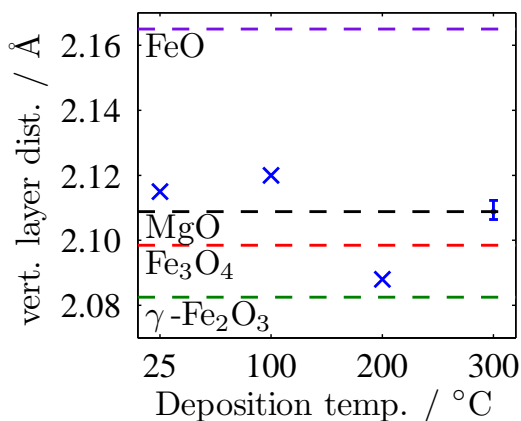
Figure 5.7: *Vertical layer distance d obtained by XRD for the samples deposited reactively in oxygen atmosphere at RT,* 100 °C *and* 200 °C. *Marked by dashed lines are theoretical values for MgO (black), wustite (purple), magnetite (red) and maghemite (green).*

46

corresponding to a film on a substrate. This shows that the interface between film and substrate has vanished in this case. The value obtained from the fringes $D \approx 60.3\,\text{Å}$ confirms that all samples in this set have a similar thickness.

5.2 XPS analysis of oxide formation

The chemical composition of the samples at each preparation step is investigated by XPS. Survey spectra over the complete energy range of the x-ray anode are recorded to check the cleanliness of the surfaces. High-resolution spectra of the Fe $2p$, Fe $3p$ and O $1s$ regions are recorded to investigate the composition of the films. The Fe $2p$ region is used to differentiate between iron oxide species in the film. By comparing the experimental data to spectra calculated with the help of Charge Transfer Multiplet theory the ratios of different oxide species can be determined. In principle this can also be done for the Fe $3p$ region, but in that case the analysis is exacerbated by the superposition of Fe and Mg peaks. Therefore the Fe $3p$ region and the O $1s$ peak are used only for the investigation of Mg and O ratios in the samples.

5.2.1 Survey spectra of cleaned substrates and pure iron films

The purity of all substrate surfaces before deposition of iron and of the iron films before oxidation is checked by a wide-range spectrum for each sample. This is shown exemplarily in Figure 5.8 for the iron film afterwards oxidized at $200\,^\circ$C. All substrates used in this work (blue line) show nearly no remaining carbon contamination on the surface (around $285\,$eV). A small trace of argon is detected at about $245\,$eV. This originates from the manufacturing process of the MgO substrates. Both signals amount to contaminations of $2-3\,\%$ of C and Ar at the substrate surface. A molybdenum signal can be seen at $227\,$eV in some cases, this is caused by the sample holder and does not affect the films. The deposited iron films (red line) are pure with only a very small amount of oxygen visible at $530\,$eV. Apart from the Fe film oxidized afterwards at RT all Fe films completely suppress the Mg photoemission and AUGER peaks, indicating that the films are at least as thick as the electron escape depth of about $5\,$nm [58].

5.2.2 Multiplet calculations of iron oxide Fe $2p$ spectra

Fe $2p$ photoemission spectra of three different iron oxide species are calculated with the method described in Section 4.3. Wustite is represented by one cluster of Fe^{2+} in octahedral symmetry. Magnetite consists of the three clusters Fe^{2+}_{oct}, Fe^{3+}_{oct} and Fe^{3+}_{tet} with the ratios 1:1:1. Maghemite consists only of Fe^{3+} ions, one cluster with octahedral and one with tetrahedral symmetry. The ratio between Fe^{3+}_{oct} and Fe^{3+}_{tet} is 5:3. Distortions of the crystal lattice which alter the symmetry state of an ion are not taken into account. The crystal field strength $Dq = 1\,$eV has been chosen. Figure 5.9 demonstrates that a calculation using this crystal field value (red line) agrees well with spectra from literature [8]. Small deviations are present because the exact values for Dq and the artificial broadening of the spectrum in literature is unknown.

The energy calibration of the cluster spectra is done with respect to the main line of the Fe
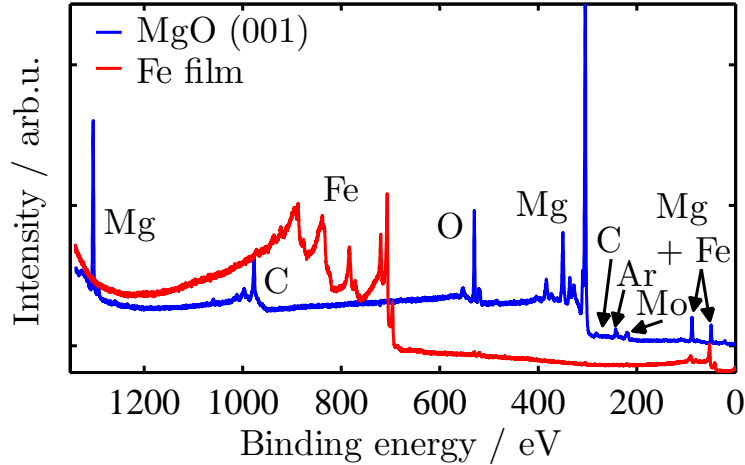
Figure 5.8: *Photoemission spectra of a cleaned MgO (001) substrate (blue line) and of a pure iron film (red line). The substrate shows residual traces of C (285 eV) and Ar (245 eV), a small Mo signal (227 eV) originates from the sample holder. The deposited iron film shows only a very small amount of oxygen (530 eV).*

$2p_{3/2}$ peak. For maghemite both clusters are calibrated to the literature value 710.7 eV [8]. The Fe^{3+} clusters in magnetite are taken to have the same binding energy as in maghemite. By subtracting an experimental spectrum of maghemite from one of magnetite a binding energy of 708.5 eV for the remaining Fe^{2+}_{oct} cluster in magnetite is obtained. The same value is also applied to the Fe^{2+} cluster in wustite.
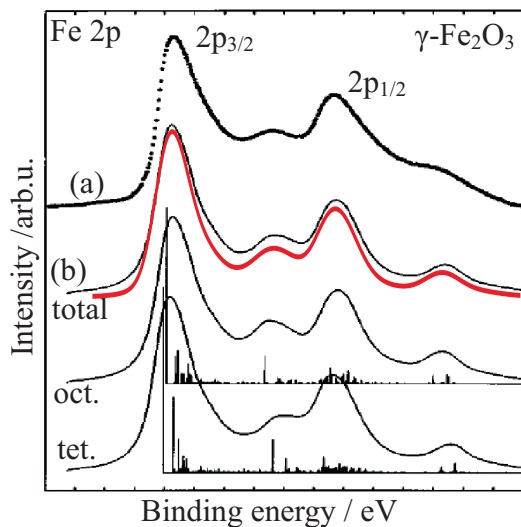
Figure 5.9: *Calculation of a maghemite Fe 2p photoemission spectrum from [8]. A calculation from this work using a crystal field value of 1 eV (red line) shows good agreement, deviations are caused by the unknown values of crystal field and artificial broadening in literature.*
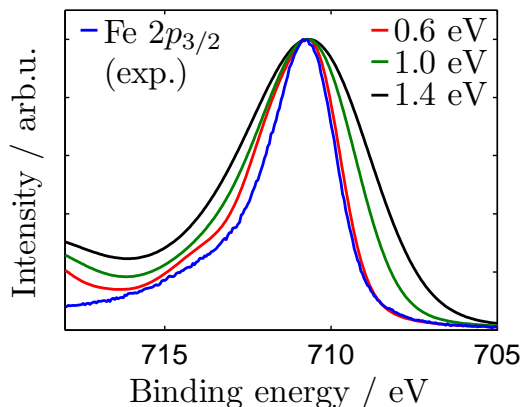
Figure 5.10: *Experimental Fe $2p_{3/2}$ photoemission peak of metallic iron (blue). The calculated spectra using a Gaussian broadening of $1.4\,\text{eV}$ (black line), $1.0\,\text{eV}$ (green line) and $0.6\,\text{eV}$ (red line) are shown. A width of $1.0\,\text{eV}$ gives the best approximation of the data.*

The broadening of photoemission peaks is usually attributed to two factors. The first contribution is the natural broadening caused by the limited lifetime of electron states. This factor is described by a Lorentzian function. It is assumed to have a width of $0.3\,\text{eV}$ [19]. The second contribution is the broadening caused by the experiment via the radiation source and the spectrometer. This factor is described by a Gaussian function. The realistic broadening of the calculated spectrum can be obtained by a folding of the two contributing functions. In Figure 5.10 calculations using a Gaussian broadening of $1.4\,\text{eV}$ (black line), $1.0\,\text{eV}$ (green line) and $0.6\,\text{eV}$ (red line) are compared to an experimental $2p_{3/2}$ spectrum of metallic Fe. This spectrum was chosen as reference because no satellite structures distorting the peak should be present. A broadening of $0.6\,\text{eV}$ results in a peak slightly thinner than the data, while a broadening of $1.4\,\text{eV}$ is clearly too much. Considering that an experimental peak of a metal oxide is always broader than the peak of the pure metal, a Gaussian function with width $1.0\,\text{eV}$ is used to approximate the experimental broadening. This is in good agreement with the specifications of the spectrometer (cf. Section 4.1.2).

The results of a multiplet calculation of the iron clusters in maghemite are shown in Figure 5.11. The calculated transitions (black sticks) are artificially broadened to gain the final spectra (blue lines).

The spectra of an iron oxide are made up of a weighted summation of the respective cluster spectra. In magnetite the three clusters Fe_{oct}^{2+}, Fe_{oct}^{3+} and Fe_{tet}^{3+} have equal ratios 1:1:1. The octahedral and tetrahedral Fe^{3+} clusters in maghemite have a ratio of 5:3. The results obtained for the oxides magnetite, wustite and maghemite are shown in Figure 5.12. The parameter values used for the calculation are taken from [8], they are summarized in Table 5.1. The calculated spectrum for magnetite is plotted in red (lowest line), wustite in purple (middle line) and maghemite in green (top line). This color coding will always be used in the following.

All three spectra show satellites on the high binding energy sides of the main Fe $2p_{3/2}$ peak. The splitting between main peak and satellites is $\Delta E \approx 6\,\text{eV}$ for wustite and $\Delta E \approx 8\,\text{eV}$ for maghemite. These values correspond well to experimental values from literature [59].
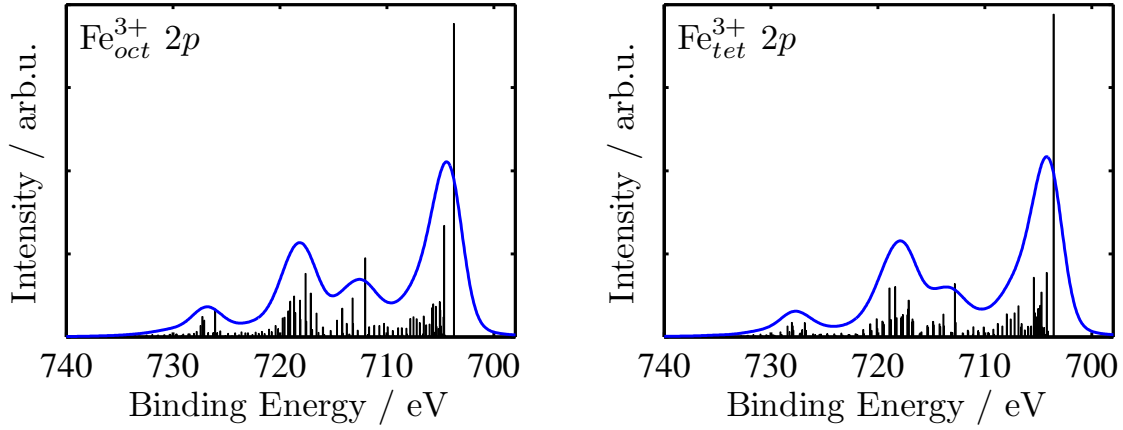
Figure 5.11: *Calculated Fe 2p photoemission spectra of an octahedral Fe^{3+} cluster (left) and a tetrahedral Fe^{3+} cluster (right) in maghemite. Black sticks mark the calculated transitions, the blue line is the artificially broadened spectrum.*

In the spectrum of magnetite a superposition of the satellites for Fe^{2+} and Fe^{3+} results in a plateau of constant intensity between the main Fe $2p_{3/2}$ and $2p_{1/2}$ peaks. The intensity ratio between main Fe $2p_{3/2}$ peak and satellite is about 2:1 for wustite and 3:1 for maghemite.
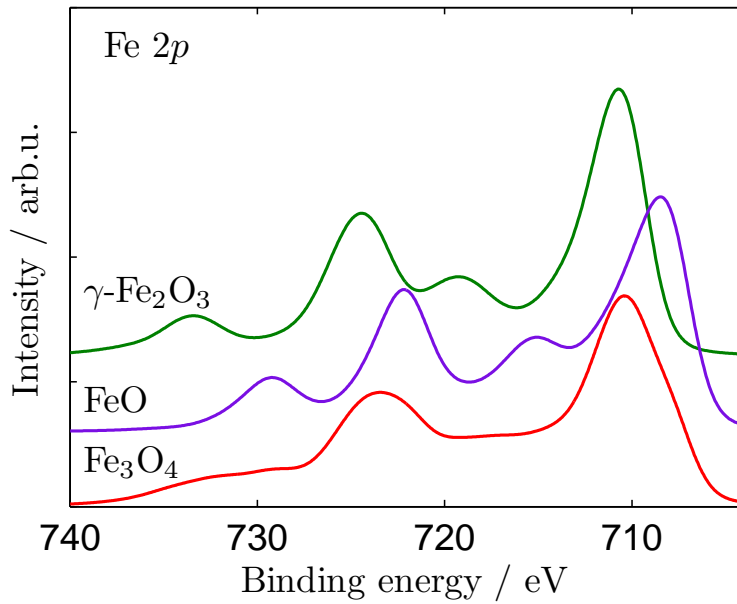
Figure 5.12: *Calculated Fe 2p photoemission spectra of iron oxides: magnetite (red), wustite (purple) and maghemite (green).*

oxide	cluster	Δ (eV)	$Te_{(g)}$ (eV)	$Tt_{2(g)}$ (eV)	U_{dd} (eV)	U_{pd} (eV)
FeO	Fe^{2+}_{oct}	4.0	2.3	-1.15	7.0	7.5
γ-Fe_2O_3	Fe^{3+}_{oct}	2.0	2.7	-1.35	7.0	7.5
	Fe^{3+}_{tet}	2.0	1.35	-2.7	7.0	7.5
Fe_3O_4	Fe^{2+}_{oct}	4.0	2.3	-1.15	7.0	7.5
	Fe^{3+}_{oct}	2.0	2.2	-1.1	7.5	8.0
	Fe^{3+}_{tet}	2.0	1.35	-2.7	7.0	7.5

Table 5.1: *Parameter values used for the cluster calculations of Fe 2p photoemission spectra of different iron oxides. The parameters are taken from [8], they are explained in Section 4.3*

5.2.3 Analysis of iron oxide Fe $2p$ spectra

The sample composition is investigated by fitting the experimental XPS data with a summation of the calculated spectra shown in the previous Section. All spectra are normalized to their integrated intensity. Therefore the weight of a spectrum in the summation is exactly the percentage of the respective oxide species in the film. The measured spectra are analyzed by changing the ratios of the calculated spectra in the summation until the experimental spectrum is reproduced well. A numerical least-squares fit is not adequate for application in this method because of the unclear energy calibration of the spectra. The absolute positions of peaks in the data as well as in the calculations can not be known (cf. Section 4.4). A slight shift of one spectrum changes the result of the fitting considerably. This is illustrated in Figure 5.13, where the same data set is fitted twice. The binding energy of the experimental data has been shifted by 0.2 eV to lower values in the right. In the left case the best fit is with 95 % magnetite and 5 % wustite, whereas in the right case it is with 77 % magnetite and 23 % wustite. This arbitrariness renders a numerical fitting routine more or less useless.

In addition to the uncertainty introduced by a numerical fitting Figure 5.13 also shows that a numerical least-squares fit does not necessarily reproduce the spectral features of the experimental data. The influence of satellites often is not taken into account by this method. Therefore the agreement between the shapes of the experimental spectra and the summed up calculations is used as an indication of an appropriate fit. The composition of the summation is altered manually until an optimum in the agreement is achieved. This criterion has the advantage of being independent of the energy calibration of the involved spectra. In addition this method assures that the presence of an oxide species in the sample, indicated by the appearance of the respective satellite, is reproduced correctly by the fit. This is a huge advantage over the numerical fitting which often ignores satellite peaks.
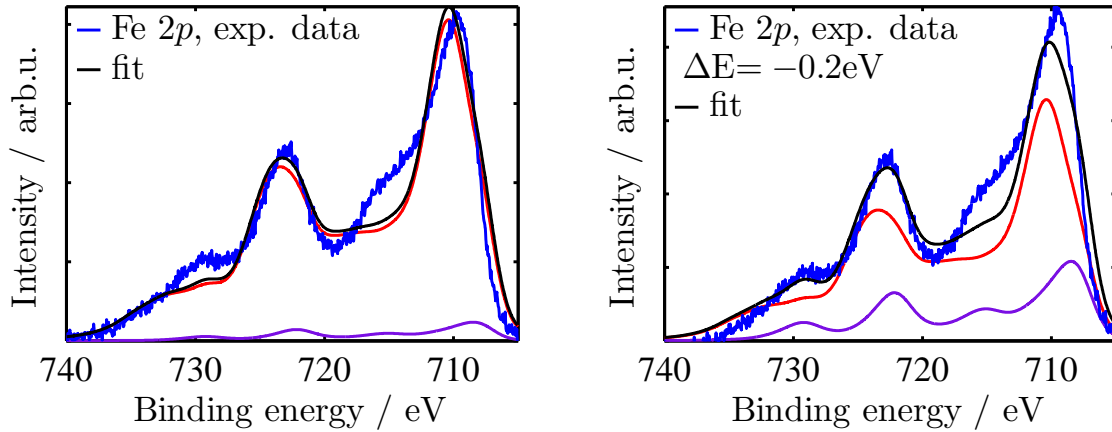
Figure 5.13: *Influence of energy shifts on the fitting of photoemission spectra. The experimental data (blue line) have been shifted by* $0.2\,\text{eV}$ *to lower binding energies in the right, altering the result of the fitting considerably.*

The percentages in the summation are altered in steps of $10\,\%$ in this analysis because smaller changes are practically undetectable in the resulting spectrum. The changes in the experimental spectra are mostly also very small. Therefore in some cases the superposition of experimental Fe $2p$ spectra at several preparation steps acts as a guideline to the changes in the data. With this help the fitting method reproduces ratios between oxide species in the spectrum and the development of the ratios during preparation of the sample very well. The accuracy of the resulting percentages must nevertheless be assumed to be about $20\,\%$ due to the limited changes in the summed-up spectrum.

In the following the colors of the spectra will always be the same: blue lines for the experimental data, black lines for the summation of the calculated spectra, red lines for the calculated spectrum of magnetite, green lines for maghemite, purple lines for wustite and, where necessary, light blue lines for metallic iron. The individual contributions to the summation will be scaled down to their respective percentages so that their influence on the spectral features of the summation is better visible. It has to be noted that the intensity of the Fe $2p_{3/2}$ peak in the calculation is always higher than in the experimental spectrum. This effect is caused by an overestimation of the background intensity for the experimental spectra at lower binding energies. The calculation does not include any background intensity and therefore can not reproduce this deviation.

5.2.3.1 Oxidation at RT

The Fe $2p$ photoemission spectra of the iron film oxidized in $1 \cdot 10^{-6}\,\text{mbar}$ O_2 at RT for one hour (left) and for two hours (right) are shown in Figure 5.14. The result of the fitting (black line) matches the form of the measured spectrum (blue) reasonably well. A signal
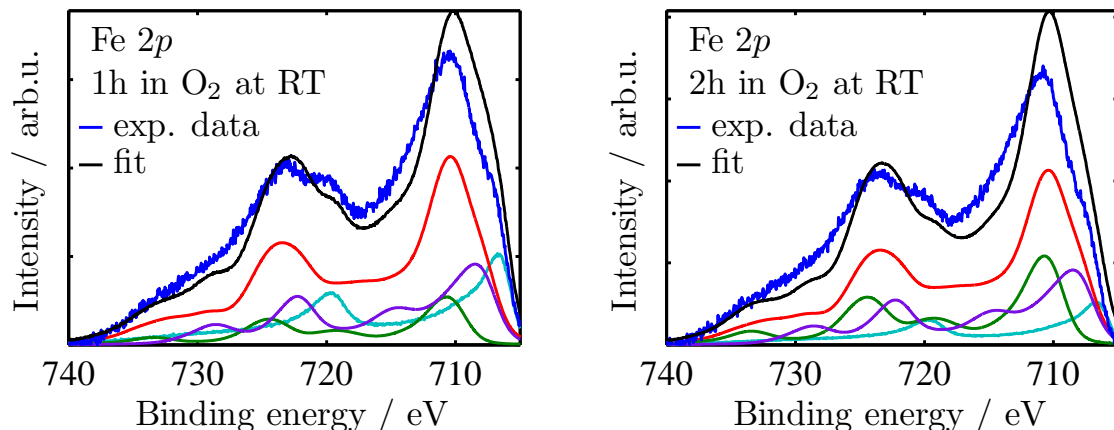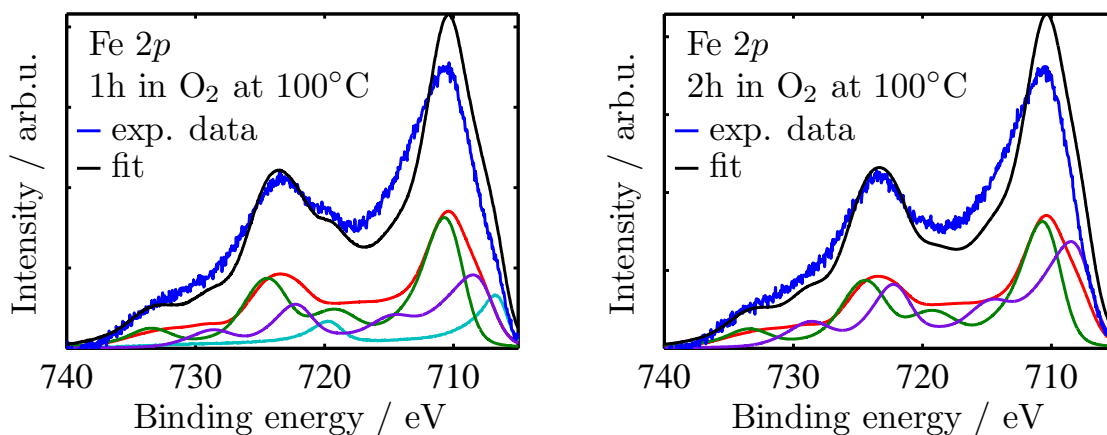
Figure 5.14: *Fitting of the Fe 2p photoemission spectra of the sample oxidized at RT after the first (left) and after the second treatment in $1 \cdot 10^{-6}$ mbar O_2 (right). The calculated spectra of magnetite (red), maghemite (green) and wustite (purple) and the experimental spectrum of metallic iron (light blue) are scaled down to their respective ratios in the fit.*

of pure Fe can be seen as a low-binding-energy shoulder of the main Fe $2p_{3/2}$ peak during the oxygen treatment. The satellite showing at about 9 eV to higher binding energy from the main peaks is mainly due to this Fe^0 signal. Other satellite structures can not be observed. Longer exposure to oxygen changes the shape of the spectrum only marginally
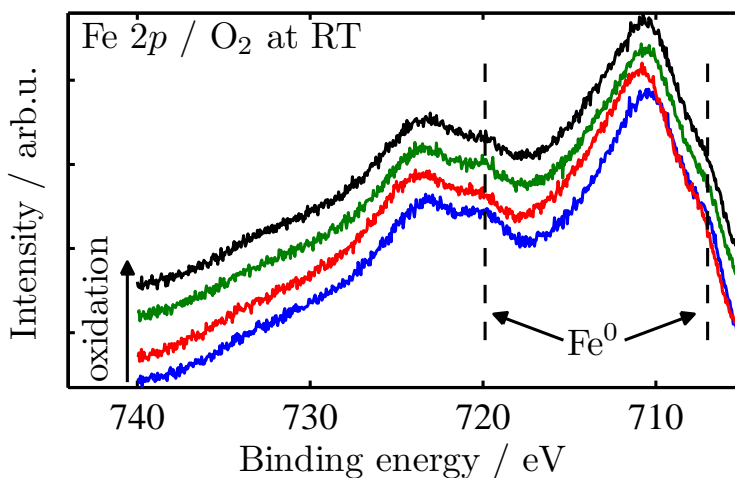
Figure 5.15: *Superposition of the experimental Fe 2p photoemission spectra for the sample oxidized at RT. Satellite positions are marked by dashed lines. The spectrum after the first oxidation is at the bottom, the spectrum after the last oxidation is at the top.*

at this temperature.

The obtained ratios can be validated by observing the changes in the experimental spectra illustrated in Figure 5.15. Bottommost is the spectrum after the first oxidation, topmost the spectrum after the last oxidation. The intensity of the satellites, indicated by dashed lines, is decreasing slightly during oxidation, indicating a decreasing Fe content. These changes are taken as a guideline to the ratios in the fit.

The ratios resulting from the fitting process are illustrated in Figure 5.16. The initial step after deposition of iron is omitted as no information is gained at that step. The color code is the same as introduced in Figure 5.14. It can be seen that at this temperature the oxidation of the iron film is very slow, a strong signal of metallic iron is still present after four hours of exposure to oxygen. There is no clear majority of one oxide species during the treatments in oxygen atmosphere, all oxide phases have nearly even ratios. A saturation for the oxidation of the film is achieved after one hour of oxygen exposure already.
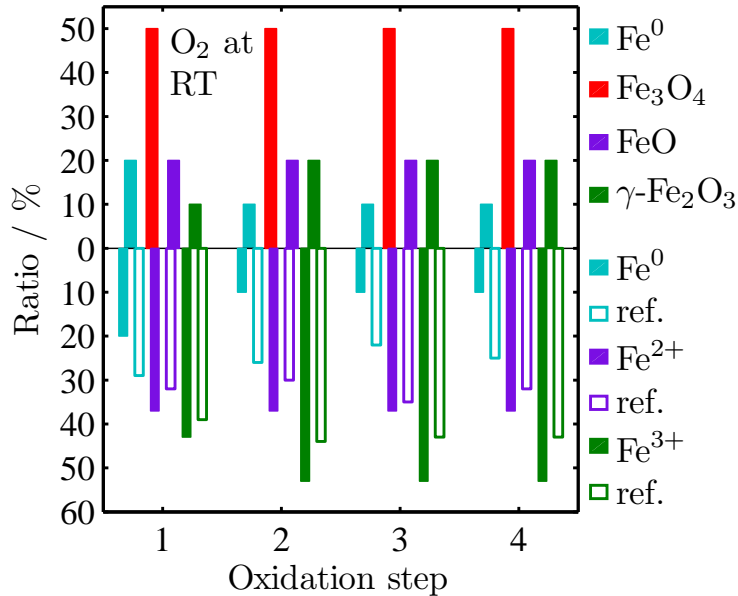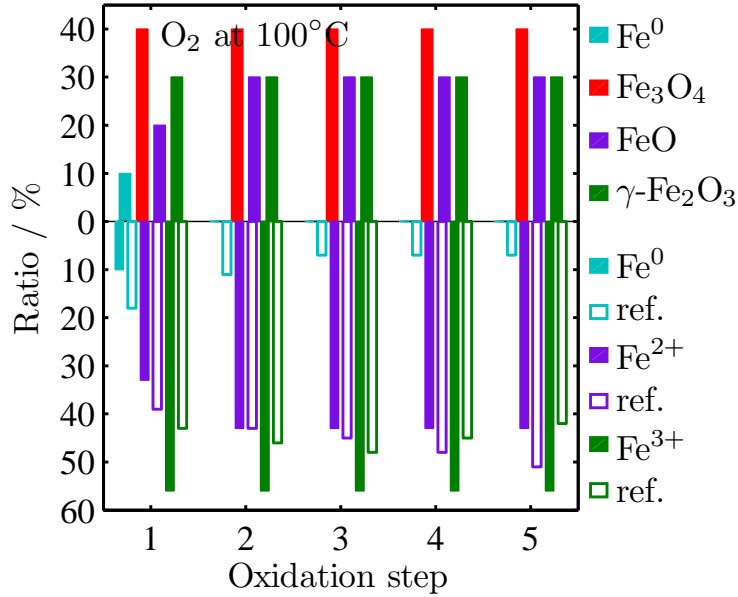

Figure 5.16: *Fe 2p fitting results for the sample oxidized at RT (upper part). From these values the ratios of Fe ions are calculated (lower part). The reference values for the ion ratios are taken from [51].*

The ratios of different iron ions can be calculated from the percentages obtained for the oxide species. Wustite contains only Fe^{2+}, maghemite only Fe^{3+}, and magnetite contains one third Fe^{2+} and two thirds Fe^{3+}. The values calculated in this way are shown in the lower part of Figure 5.16. They are compared to reference data presented in [51]. The reference data were obtained by fitting the experimental data of the films using reference

spectra of materials that contained only Fe^{2+} or Fe^{3+} ions, as described in Section 4.5. The colors are the same as before, purple bars denote Fe^{2+}, green bars Fe^{3+} and light blue bars metallic Fe^0. It can be seen that the development of the ratios is quite similar for both fitting methods. The ratios themselves are within acceptable agreement if one takes into account the relatively large error for the fitting with calculated spectra as mentioned in Section 5.2.3. The amount of metallic iron decreases only slowly during oxidation at this temperature. The majority of iron in the film has a Fe^{3+} valency even at this temperature.

5.2.3.2 Oxidation at $100\,°C$

The results for the iron film oxidized at $100\,°C$ are shown in Figure 5.17. After the first treatment in $1 \cdot 10^{-6}$ mbar O_2 (left) a small signal of Fe^0 is still visible. This leads to a small satellite at $9\,eV$ higher binding energy from the main Fe $2p_{3/2}$ peak and a weak low binding energy shoulder of the Fe $2p_{3/2}$ peak. These features vanish after the second oxidation step (right). No additional peak structures can be identified. With continued oxidation the spectrum does not change further to any visible degree.

Figure 5.17: *Fitting of the Fe 2p photoemission spectra of the sample oxidized at $100\,°C$ after the first (left) and second (right) treatment in $1 \cdot 10^{-6}$ mbar O_2. The calculated spectra of magnetite (red), maghemite (green) and wustite (purple) and the experimental spectrum of metallic iron (light blue) are scaled down to their respective ratios in the fit.*

The percentages obtained from the fitting of the spectra are summarized in Figure 5.18, displayed in the same colors as before. Apart from the disappearing Fe^0 content no visible change in the composition of the film can be observed. The decrease of the Fe^0 ratio at this temperature is faster than at RT, but the composition of the film is almost the same as for the sample oxidized at RT. Again the dominant valency in the film is Fe^{3+}.
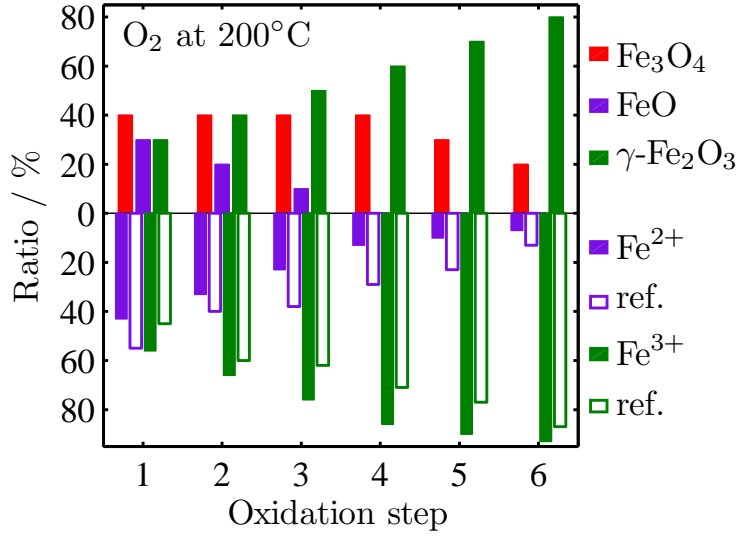
Figure 5.18: *Fe 2p fitting results for the sample oxidized at* 100 °C *(upper part). From these values the ratios of Fe ions are calculated (lower part). The reference values for the ion ratios are taken from [51].*
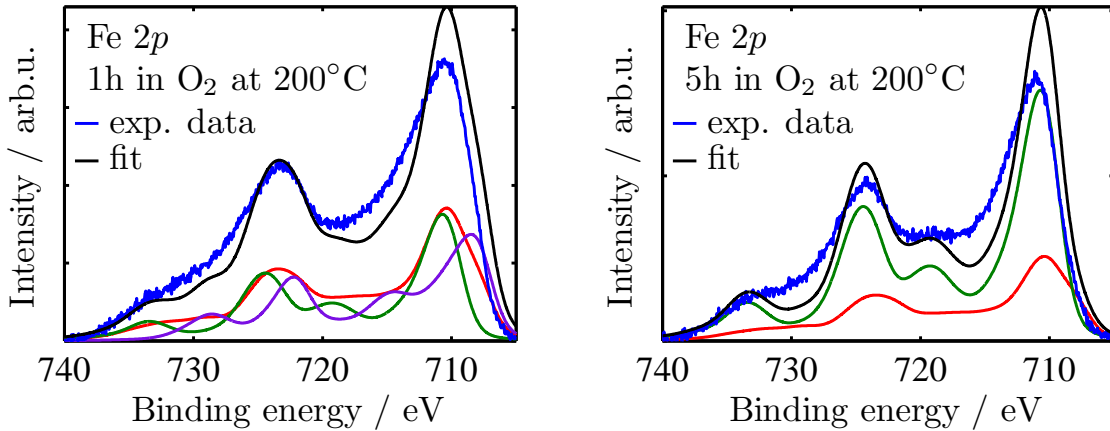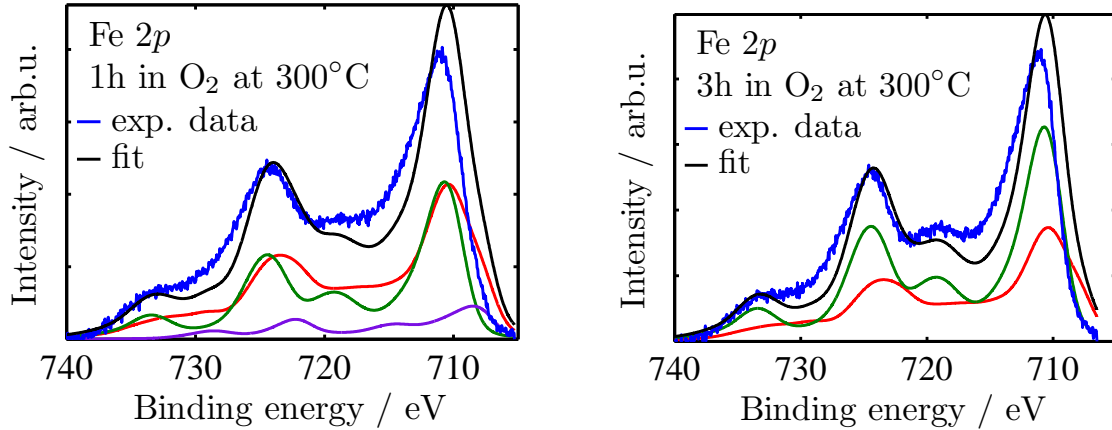

Figure 5.19: *Fitting of the Fe 2p photoemission spectra of the sample oxidized at* 200 °C *after the first (left) and fifth (right) treatment in* $1 \cdot 10^{-6}$ mbar O_2. *The calculated spectra of magnetite (red), maghemite (green) and wustite (purple) are scaled down to their respective ratios in the fit.*

5.2.3.3 Oxidation at $200\,°C$

Figure 5.19 shows the results for the iron film oxidized in $1 \cdot 10^{-6}\,$mbar O_2 at $200\,°C$ for one hour (left) and for five hours (right). At this temperature no signal of metallic iron is detected anymore. A gradually increasing satellite at about $8\,$eV higher binding energy from the main Fe $2p_{3/2}$ peak can be observed during the oxidation process. This satellite is characteristic for the formation of Fe^{3+} ions. The changes in the Fe $2p$ spectra are illustrated in the superposition of the experimental data shown in Figure 5.20. Between the first oxidation step (lowest line) and the last oxidation step (topmost line) the Fe^{3+} satellite increases while at the same time the weak low binding energy shoulder of the main Fe $2p_{3/2}$ peak caused by Fe^{2+} vanishes.
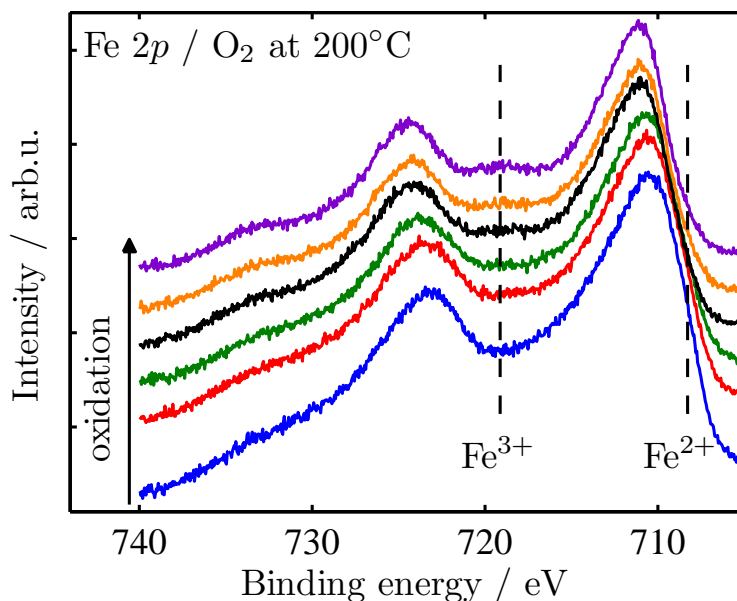
Figure 5.20: *Superposition of the experimental Fe 2p photoemission spectra for the sample oxidized at $200\,°C$. Satellite positions are marked by dashed lines. The spectrum after the first oxidation is at the bottom, the spectrum after the last oxidation is at the top.*

The percentages obtained from the fitting are illustrated in Figure 5.21. The ratio of Fe^{3+} ions rises constantly through all oxidation steps. Yet the film is not fully oxidized after six hours in oxygen atmosphere, a small amount of Fe^{2+} ions still remains in the film.

Figure 5.21: *Fe 2p fitting results for the sample oxidized at* $200\,^\circ\text{C}$ *(upper part). From these values the ratios of Fe ions are calculated (lower part). The reference values for the ion ratios are taken from [51].*

Figure 5.22: *Fitting of the Fe 2p photoemission spectra of the sample oxidized at* $300\,^\circ\text{C}$ *after the first (left) and third (right) treatment in* $1 \cdot 10^{-6}$ mbar O_2. *The calculated spectra of magnetite (red), maghemite (green) and wustite (purple) are scaled down to their respective ratios in the fit.*

5.2.3.4   Oxidation at $300\,°C$

The results for the iron film oxidized at $300\,°C$ are shown in Figure 5.22. The left image shows the result after one, the right after three treatments in $1 \cdot 10^{-6}$ mbar O_2. Similar to the results for the oxidation at $200\,°C$ a satellite at about $8\,eV$ higher binding energy from the main Fe $2p_{3/2}$ peak appears during the preparation, typical for Fe^{3+}. However, in this case the satellite appears faster and is slightly larger. The fitting results in Figure 5.23 demonstrate that at this temperature the iron film oxidizes very fast and almost completely within a few hours. Only small amounts of wustite (Fe^{2+}) are found in the film, the majority is maghemite (Fe^{3+}) already after the second treatment in oxygen.
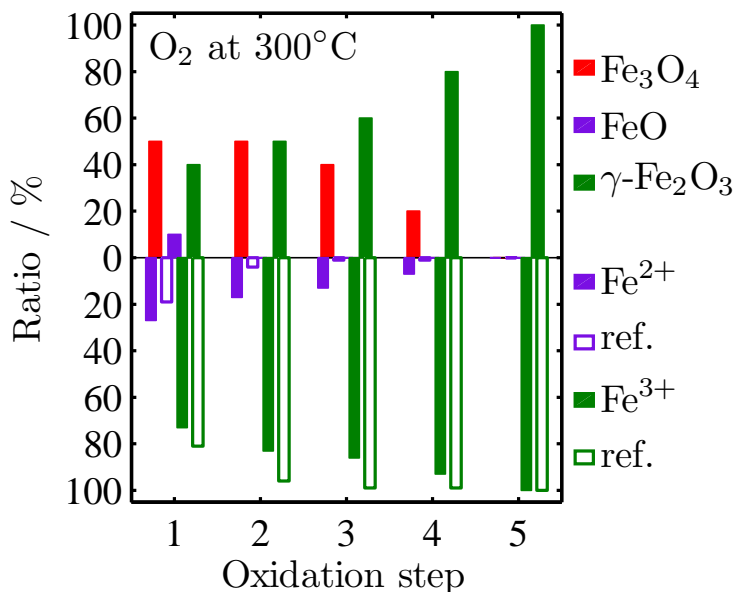
Figure 5.23: *Fe 2p fitting results for the sample oxidized at $300\,°C$ (upper part). From these values the ratios of Fe ions are calculated (lower part). The reference values for the ion ratios are taken from [51].*

5.2.3.5   Reactive growth in oxygen atmosphere

The photoemission spectra of the samples deposited in an oxygen atmosphere exhibit only a very weak dependence on the substrate temperature during the deposition. This is shown in Figure 5.24. In the left the result for the sample prepared at RT is presented. The only visible feature of the spectrum is a weak low binding energy shoulder of the main Fe $2p_{3/2}$ peak, other satellites can not be observed. With increasing temperature the shoulder of
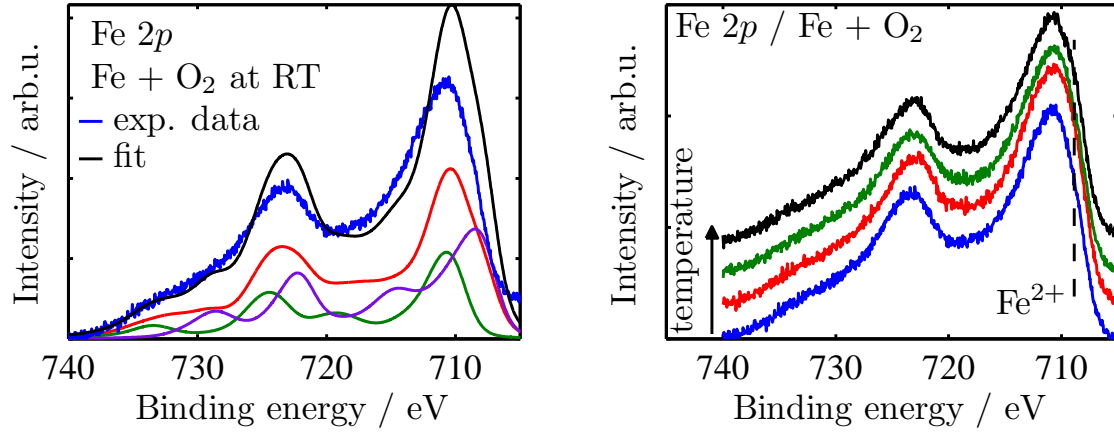
Figure 5.24: *Fitting of the Fe 2p photoemission spectrum of the sample deposited reactively in $1 \cdot 10^{-6}$ mbar O_2 atmosphere at RT (left). The calculated spectra of magnetite (red), maghemite (green) and wustite (purple) are scaled down to their respective ratios in the fit. The great similarity of the data can be seen in the superposition of the experimental Fe 2p photoemission spectra of all four samples of this set (right), from bottom to top at RT, $100\,°C$, $200\,°C$ and $300\,°C$. The position of the low binding energy shoulder is marked by a dashed line.*
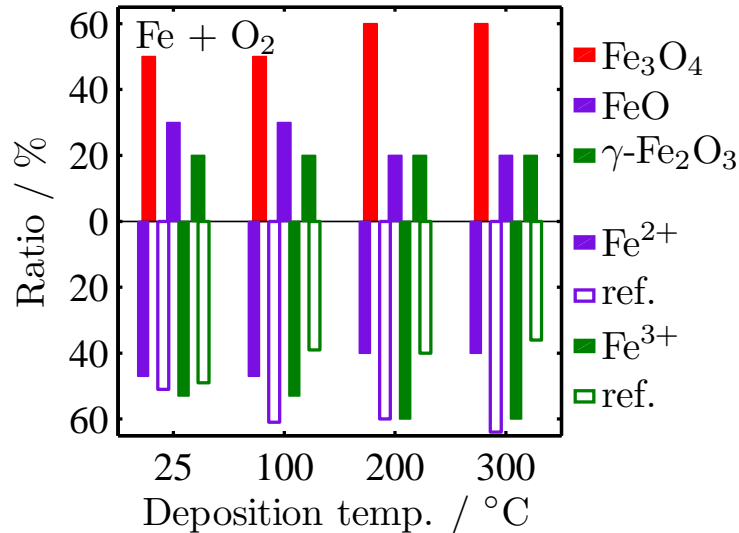
Figure 5.25: *Fe 2p fitting results for the samples deposited reactively in oxygen atmosphere at different substrate temperatures (upper part). From these values the ratios of Fe ions are calculated (lower part). The reference values for the ion ratios are taken from [51].*

the Fe $2p_{3/2}$ peak becomes slightly weaker. This indicates a decreasing content of Fe^{2+} in the sample. To illustrate this in the right of the Figure a superposition of the spectra of all four samples in this set is shown, from bottom to top for the temperatures RT, $100\,°C$, $200\,°C$ and $300\,°C$.

The results of the fitting are presented in Figure 5.25. A clear majority of one iron ion is not present, as seen from the absence of any satellites in the spectra. It is remarkable that the reference data show an increase in Fe^{2+} content rather than a decrease, as is to be expected for higher temperatures.

5.2.4 Analysis of oxygen and magnesium ratios

The Fe $2p$ photoemission spectra discussed in the last Sections give information about the changing ratios of iron valencies during the oxidation. To fully characterize the films other elements present in the sample must be investigated as well. For this purpose photoemission spectra of the oxygen O $1s$ peak and the Fe $3p$ region are analyzed.
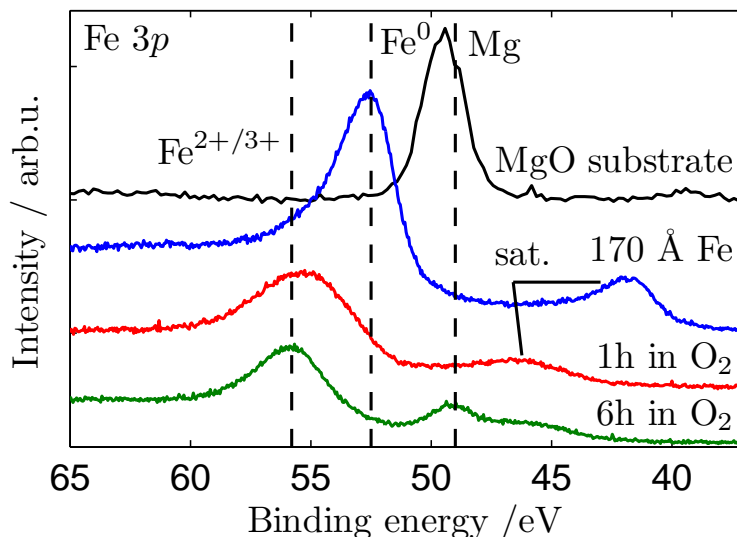
Figure 5.26: *Experimental photoemission spectra of the Fe $3p$ region for a clean MgO substrate (black line, top) and $170\,Å$ Fe (blue line) deposited on the substrate. After oxidation in $1 \cdot 10^{-6}$ mbar O_2 at $200\,°C$ for two hours (red line) and for six hours (green line, bottom) the spectra a shifted. The theoretical positions of photoemission lines for Mg, metallic Fe and Fe ions are indicated.*

The Fe $3p$ region consists of the Fe $3p$ peak at about $52 - 55\,eV$ and the Mg $2p$ peak at $49\,eV$. These two peaks overlap to a considerable degree, which makes a quantitative analysis of this region difficult. Figure 5.26 shows the changes that occur in this region

during sample processing. A clean MgO substrate (black line) shows only the Mg $2p$ peak. For a pure iron film of about $17\,\mathrm{nm}$ thickness the Mg signal is suppressed and only the Fe $3p$ peak can be seen (blue line). This shows that iron has grown in a closed film on the substrate. After one treatment in $1 \cdot 10^{-6}\,\mathrm{mbar}$ O_2 at $200\,^{\circ}\mathrm{C}$ (red line) a chemical shift from iron to iron oxide can be observed, and after six treatments in oxygen at this temperature (green line) a Mg signal is visible again. The Fe satellite at about $10\,\mathrm{eV}$ lower binding energy that is caused by charging of the sample overlaps with the Mg peak at this point and thus makes the quantitative analysis of the region considerably more complicated. The recurrence of Mg in the photoemission spectra can be caused either by a break-up of the film which leaves the MgO substrate exposed or by a segregation of Mg atoms into the film. The former process is unlikely because of the large film thickness. Additionally, the segregation of Mg to the surface of iron oxide films is already known in literature. This will be discussed in more detail later.
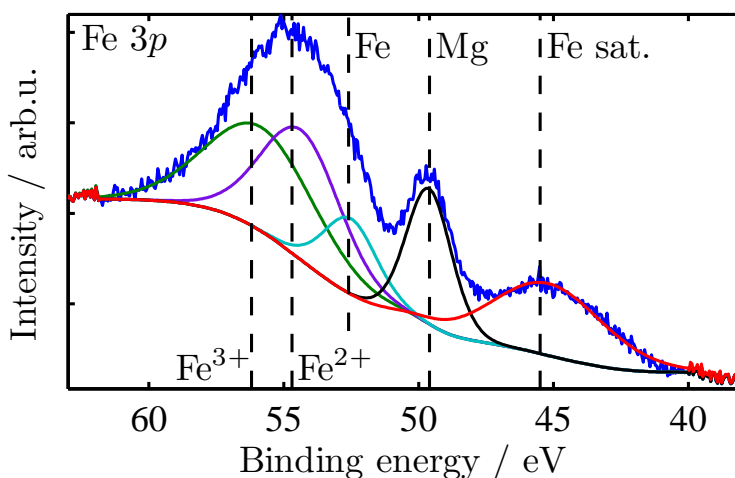
Figure 5.27: *Fitting of the photoemission spectrum of the Fe $3p$ region shown exemplarily for the sample oxidized for one hour at RT (blue line).* Pseudo-Voigt *functions are assigned to each contribution in the spectrum: Fe^{3+} (green), Fe^{2+} (purple), Fe^0 (light blue), Mg $2p$ (black) and the Fe satellite (red).*

The ratios of Mg and O in the samples are determined by assigning Pseudo-Voigt functions of the form

$$GL(E_B, E_0, m, w) \;=\; \frac{\exp\!\left(-4\ln 2(1-m)\frac{(E_B - E_0)^2}{w^2}\right)}{1 + 4m\frac{(E_B - E_0)^2}{w^2}} \tag{5.1}$$

to each peak in the O $1s$ and Fe $3p$ regions and then fitting the functions to the experimental data. In this definition E_B is the binding energy in the spectrum, E_0 the binding energy
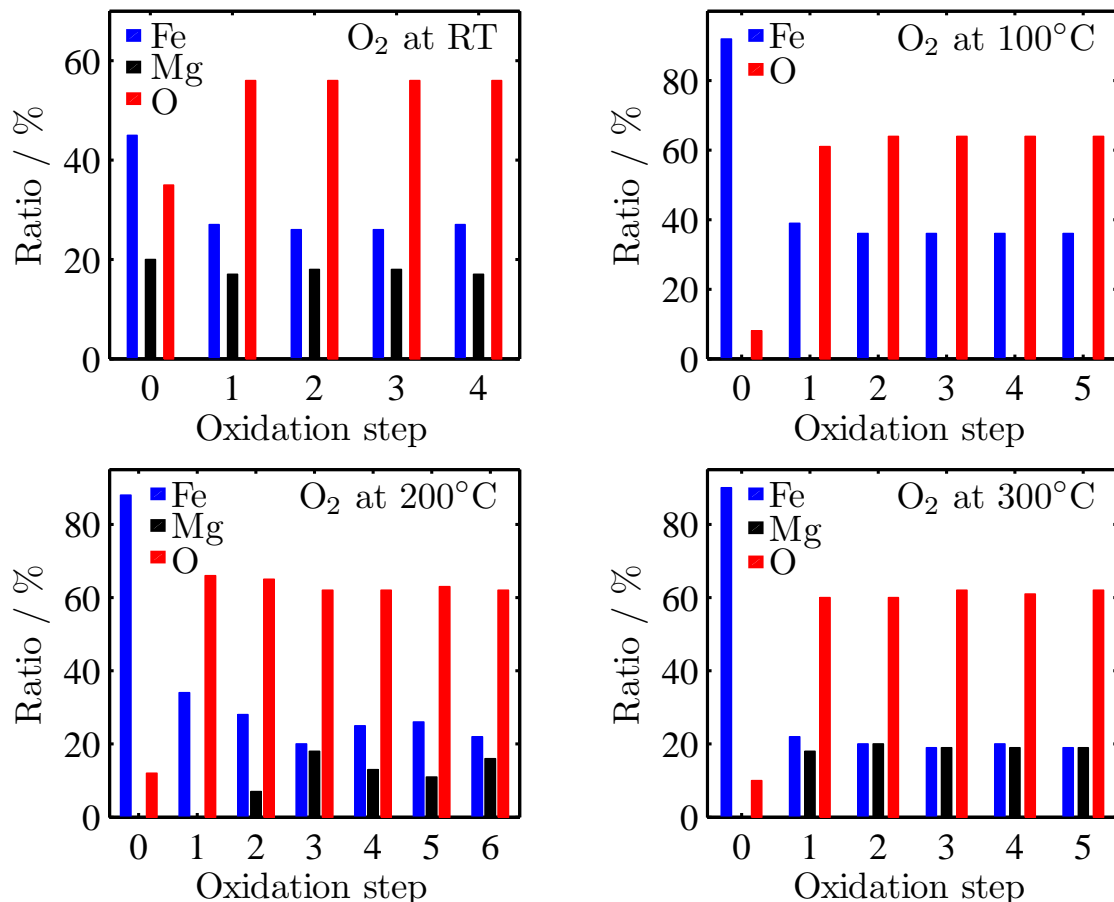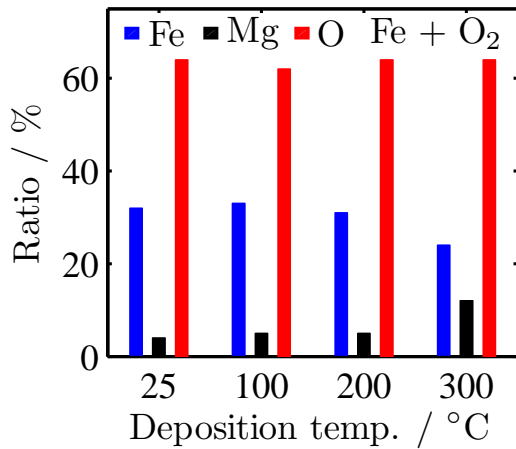
Figure 5.28: *Ratios of Fe (blue), Mg (black) and O (red) obtained from the Fe 3p region and the O 1s peak of the samples oxidized after deposition. The initial step is the pure iron film before exposure to oxygen.*

with maximum intensity of the peak, w is the FWHM of the function and m is a weighting factor between Lorentzian and Gaussian character of the function, $m = 0$ indicating pure Gaussian behavior and $m = 1$ pure Lorentzian. Because of the mixed valency of Fe as seen in the Fe $2p$ spectra in Section 5.2.3 three different functions for metallic iron, Fe^{2+} and Fe^{3+} ions are used and two more functions for the Mg $2p$ peak and the Fe satellite. Figure 5.27 shows an example of the fitted Fe $3p$ region for the sample oxidized at RT for one hour. From such a fit peak areas for each element are obtained. By considering a sensitivity factor for the respective electron orbitals the peak areas can then be converted to concentrations of the respective element in the sample (cf.Section 2.1.2.6).

The results of the analysis for the samples oxidized after deposition of iron are summarized in Figure 5.28. The initial step 0 is always the pure iron film before exposure to oxygen. In the case of the sample oxidized at RT the initial iron film is thin enough so that the signal of the MgO substrate is not fully suppressed. Subtracting the oxygen ratio arising from

the substrate in this case, the amount of oxygen contamination in the iron film is about 10 % for all iron films prior to oxidation. After oxidation for one hour the ratio of oxygen has increased to about 60 % in all cases. A further increase of the oxygen content of the films can not be observed here. It can well be seen that for temperatures above 100 °C Mg is starting to appear again during the oxidation. This effect is enhanced for increasing temperatures. At 300 °C the film contains the same amounts of Fe and Mg after oxidation.

Figure 5.29 shows the compositions of the samples deposited reactively in oxygen atmosphere. The content of oxygen is comparable to the other set of samples. For different deposition temperatures the ratios of the elements are very similar. The film thickness of about 75 Å obtained by XRR is only a little larger than the photoelectron escape depth of 53 Å found in [58]. Therefore a small amount of MgO is still visible in the spectra. Only for a temperature of 300 °C the Mg ratio is increased compared to the background seen for lower temperatures, which means that Mg has diffused into the film also.

Figure 5.29: *Ratios of Fe (blue), Mg (black) and O (red) obtained from the Fe 3p region and the O 1s peak of the samples deposited reactively in oxygen atmosphere.*

5.3   LEED characterization of the oxidation process

LEED measurements were performed after every preparation step. The reflected beam is concealed by the electron source in the images. All LEED images shown in the following Sections were taken at an electron energy of 170 eV. For some samples prepared later in the course of this work a dark area can be seen in the lower right corner of the LEED screen. This does not originate from the samples but is caused by a defect in the fluorescence screen of the LEED optics.
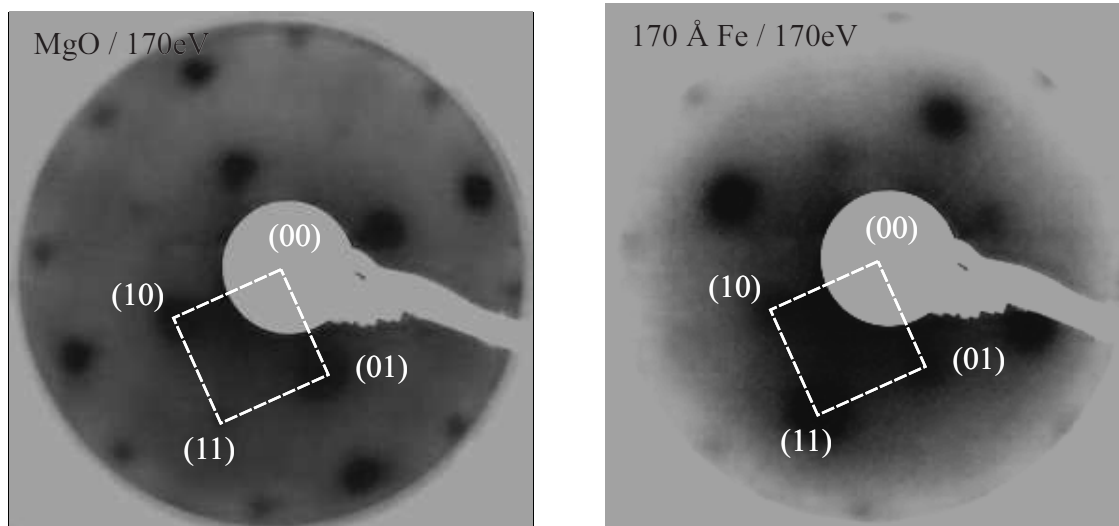
Figure 5.30: *LEED patterns of a clean MgO substrate (left) and a 170 Å thick Fe film (right). Both show a (1 × 1) structure. Substrate and iron film can be distinguished by the differing brightness of the diffraction spots. Images were taken at an electron energy of 170 eV.*

All pure iron films prepared in this work exhibit the expected (1 × 1) structure shown exemplarily in Figure 5.30 for the iron film later oxidized at 100 °C. On the left the image of a clean MgO substrate is shown, on the right the image of the 170 Å thick iron film. The diffraction spots for the substrate and the iron film are at the same positions because the surface unit cell of iron has almost the same size as the surface unit cell of MgO. But due to the differences in the crystal structures the diffraction spots of the two materials are visible at different electron energies, so that substrate and film can be distinguished by comparing the patterns taken at the same electron energy. In the following the pattern of the clean substrate will be denoted as $(1 \times 1)_{MgO}$ in order to distinguish it from the patterns of iron oxides with a spinel structure.

5.3.1   Oxidation at RT and $100\,°C$

The oxidation of an iron film at RT does not result in any observable LEED spots. After deposition of $30\,\text{Å}$ of iron a very weak LEED pattern can be seen (cf. Figure 5.31). However, compared to the images in Figure 5.30, the positions of the bright spots resemble more the pattern of the MgO substrate in the left of the Figure than the pattern of the iron film in the right. This indicates that either the iron film is thin enough for the substrate structure to show, or that no iron has been deposited on the investigated spot of the sample. After one hour of treatment in $1 \cdot 10^{-6}\,\text{mbar}$ O_2 at RT the LEED pattern vanishes completely, the oxidizes film shows no surface structure at this temperature.
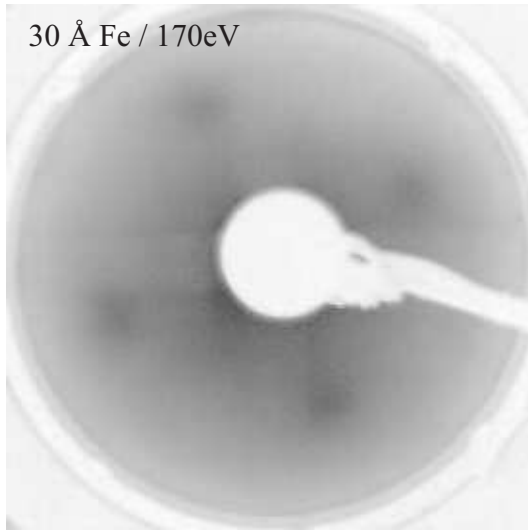
Figure 5.31: *LEED pattern of a pure iron film of thickness $D \approx 30\,\text{Å}$. A very weak $(1 \times 1)_{MgO}$ pattern can be observed. The pattern vanishes after exposure to oxygen at RT. Image was taken at an electron energy of $170\,\text{eV}$.*

Oxidation at $100\,°C$ for a $170\,\text{Å}$ thick iron film is illustrated in Figure 5.32. The pure iron film (top) shows a simple $(1 \times 1)_{MgO}$ pattern. After five hours in $1 \cdot 10^{-6}\,\text{mbar}$ O_2 atmosphere at this temperature (bottom) the pattern clearly changes. Along both unit cell directions additional spots appear that correspond to two perpendicular (2×1) domains with one unit cell direction twice as long as for MgO (or FeO). This is indicated by red markers in the right of the Figure. During the annealing of this sample without oxygen the pattern will become clearer, which will be shown in a later Section.

5.3.2   Oxidation at $200\,°C$

This sample was treated six times in $1 \cdot 10^{-6}\,\text{mbar}$ O_2 at $200\,°C$. Figure 5.33 shows the LEED patterns after the second (top) and the sixth (bottom) treatment. After two hours of oxygen exposure additional spots are visible between the ones of the initial $(1 \times 1)_{MgO}$ pattern. A doubled periodicity along both unit cell directions compared to MgO can be identified. These spots define a new (1×1) unit cell with twice the size of MgO, as is the case for iron oxides with a spinel structure. Other spots form a $(\sqrt{2} \times \sqrt{2})R45°$
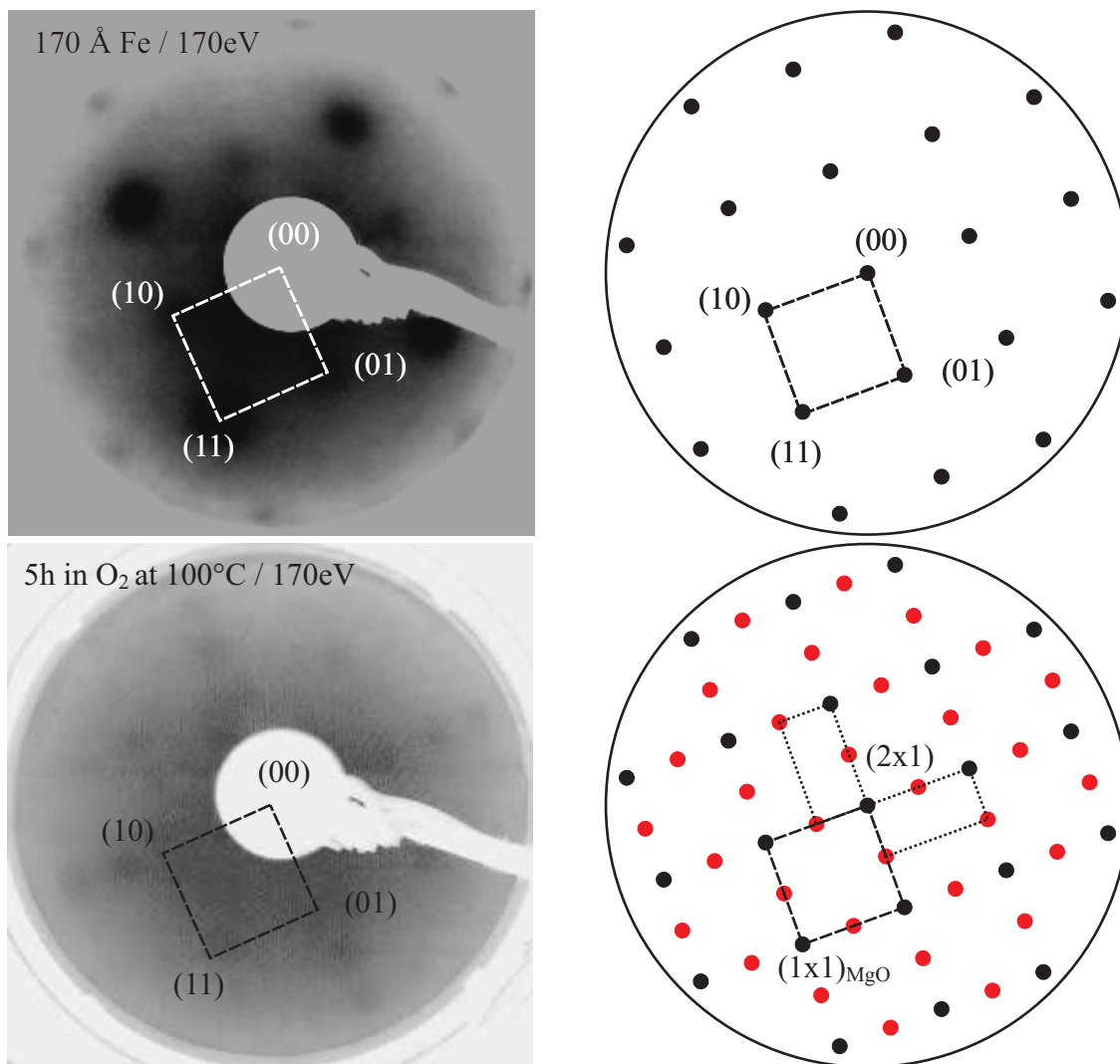
Figure 5.32: *LEED patterns of the pure $D \approx 170\,\text{Å}$ iron film (top) and the same film after five treatments in oxygen atmosphere at $100\,°C$ (bottom). The oxide film shows a (2×1) pattern in two orthogonal domains. The pattern is illustrated in the right half of the Figure. Black markers indicate the underlying $(1 \times 1)_{MgO}$ pattern, red markers indicate the additional spots. Images were taken at an electron energy of $170\,eV$.*
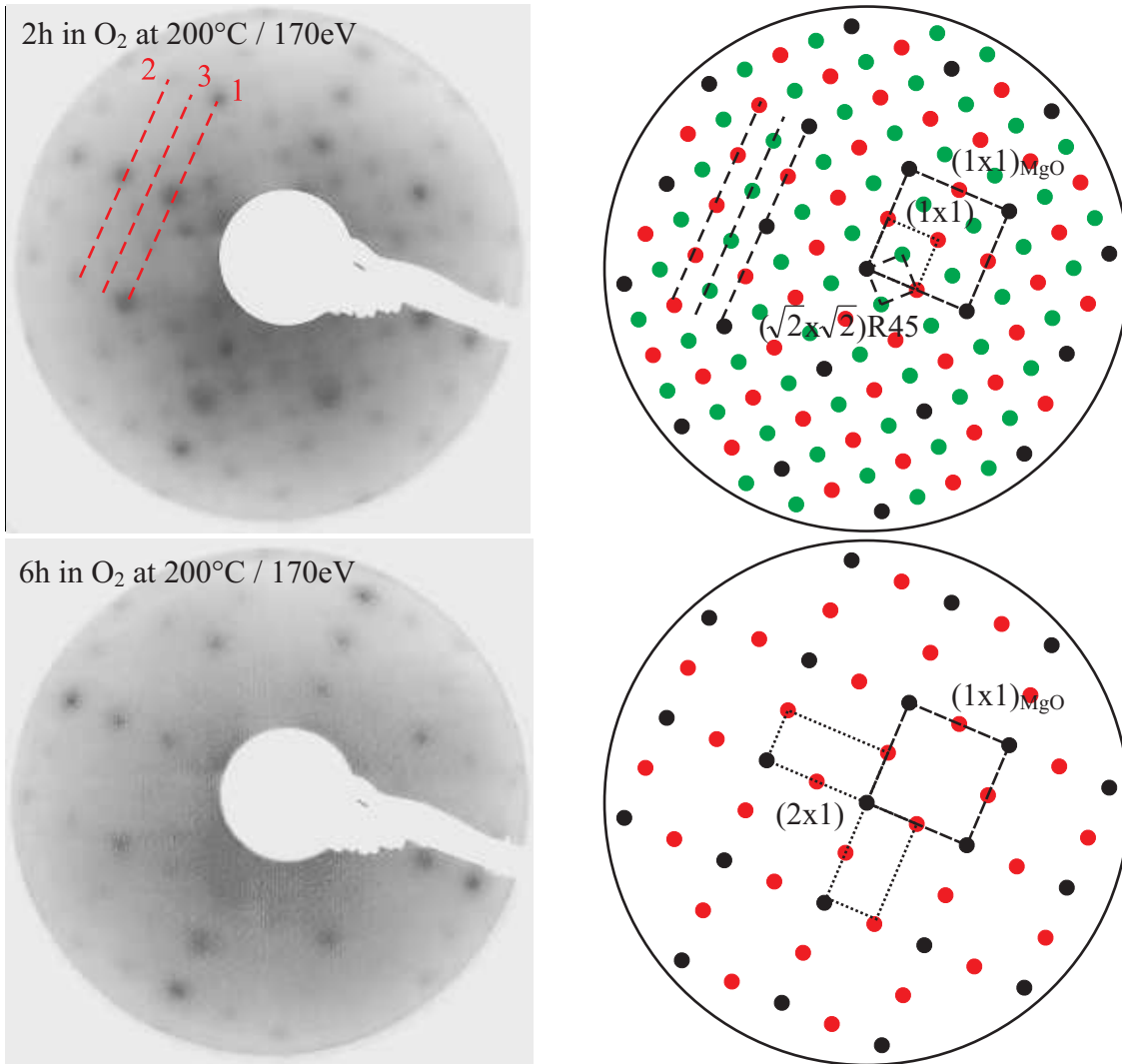
Figure 5.33: *LEED patterns of the sample oxidized at $200\,°C$ after two (top) and after six treatments in oxygen atmosphere (bottom). The upper image shows a $(\sqrt{2} \times \sqrt{2})R45°$ reconstruction, the lower image two perpendicular $(2{\times}1)$ structures. The lines in the upper image indicate the positions of the line profiles in Figure 5.34. In the right half the observed patterns are illustrated. Black markers indicate a $(1 \times 1)_{MgO}$ pattern, red markers define the larger (1×1) pattern in the upper image and the (2×1) domains in the lower image. Green markers in the upper image show the reconstruction spots. Images were taken at an electron energy of $170\,eV$.*

reconstruction with respect to this new unit cell. In the right of the Figure the pattern is illustrated. Black markers form the $(1 \times 1)_{MgO}$ unit cell, red markers the doubled (1×1) unit cell and green markers represent the reconstruction spots.
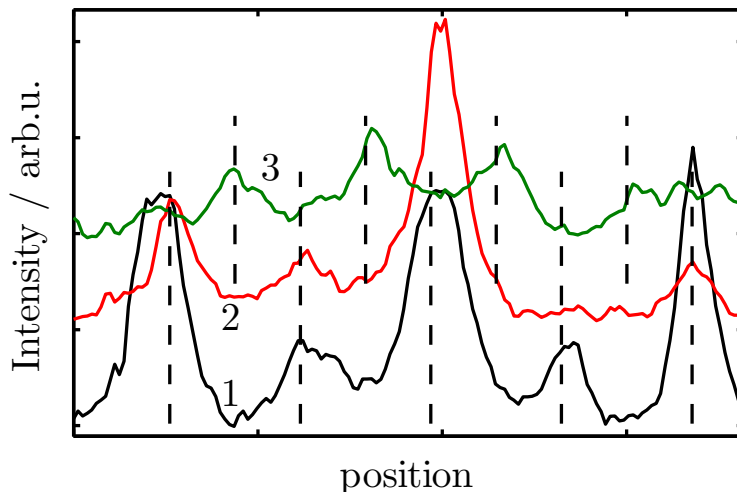
Figure 5.34: *Line profiles from the LEED pattern of the sample oxidized for* 2h *at* 200 °C. *The positions of the lines are indicated in the top left in Figure 5.33. Line 3 shows spots between those on the other two lines, forming a* $(\sqrt{2} \times \sqrt{2})R45°$ *reconstruction.*

The LEED pattern can be confirmed by the line profiles shown in Figure 5.34. The profiles were taken at the positions indicated in the top left of Figure 5.33. Lines 1 and 2 show spots defining the (1×1) pattern, line 3 shows spots at intermediate positions belonging to the reconstruction. After another four hours of exposure to oxygen the LEED pattern is reduced again to two perpendicular (2×1) structures that have already been observed for the iron film oxidized at 100 °C. This time the pattern is much more clearer at this temperature.

5.3.3 Oxidation at $300\,°C$

The LEED pattern for the sample oxidized in $1 \cdot 10^{-6}\,$mbar O_2 at $300\,°C$ is shown in Figure 5.35. The film shows a $(\sqrt{2} \times \sqrt{2})R45°$ reconstructed surface already after the first exposure to oxygen. This again indicates a surface unit cell twice as large as for MgO. The observed pattern becomes slightly weaker with each successive oxygen treatment.
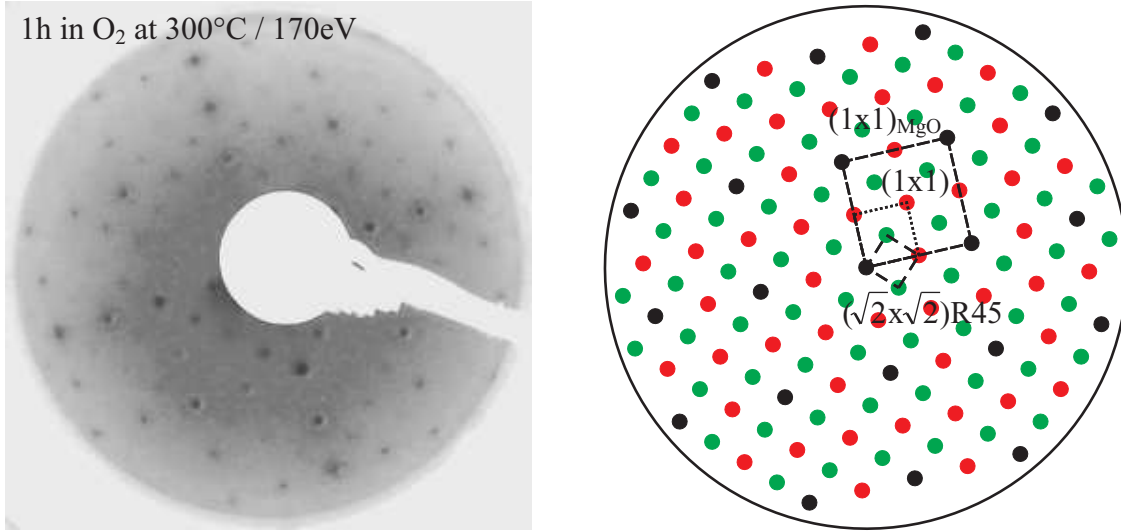
Figure 5.35: *LEED pattern of the sample oxidized at $300\,°C$ after one treatment in oxygen atmosphere (left). The pattern is a $(\sqrt{2} \times \sqrt{2})R45°$ reconstruction illustrated in the right. Black markers indicate a $(1 \times 1)_{MgO}$ pattern, red markers belong to the doubled surface unit cell and green markers show the reconstruction spots. Image was taken at an electron energy of $170\,$eV.*

5.3.4 Reactive growth in oxygen atmosphere

All four samples deposited in oxygen atmosphere are about 70 Å thick. The LEED results of these films are similar to that of the iron films oxidized after deposition at corresponding temperatures. Figure 5.36 shows the LEED patterns for the samples prepared at RT (top) and at 100 °C (bottom). The diffraction patterns consist of two orthogonal (2×1) domains. For the higher temperature the pattern is considerably clearer, indicating a higher degree of order of the film surface. In the illustration in the right of the Figure the $(1 \times 1)_{MgO}$ pattern is indicated by black markers, red markers represent the (2×1) domains.
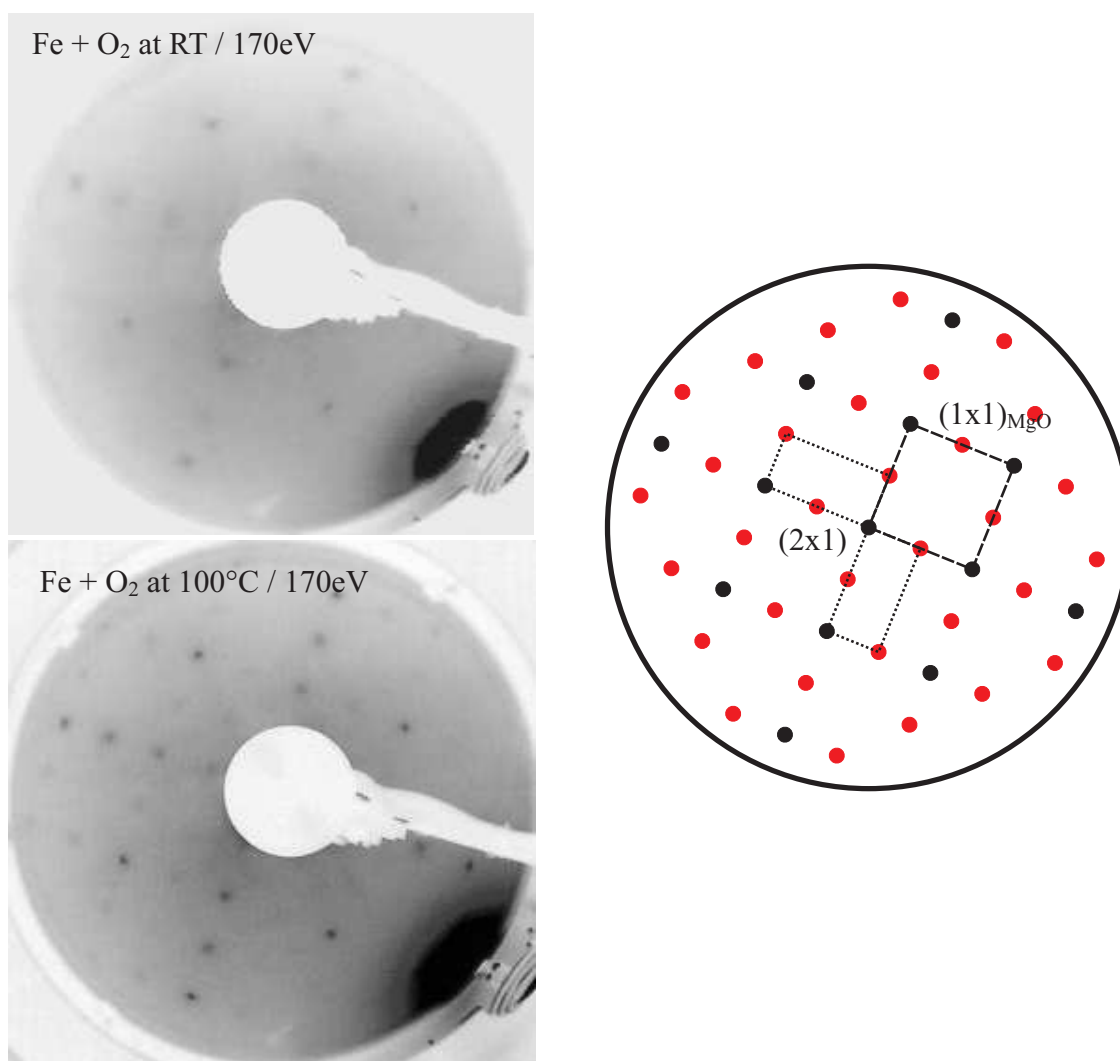
Figure 5.36: *LEED patterns of the samples deposited reactively in oxygen atmosphere at RT (top left) and at 100 °C (bottom left). The oxide films show two perpendicular (2 × 1) domains, the pattern is illustrated in the right half of the Figure. Black markers indicate the spots of a (1 × 1)$_{MgO}$ pattern. Images were taken at an electron energy of 170 eV.*
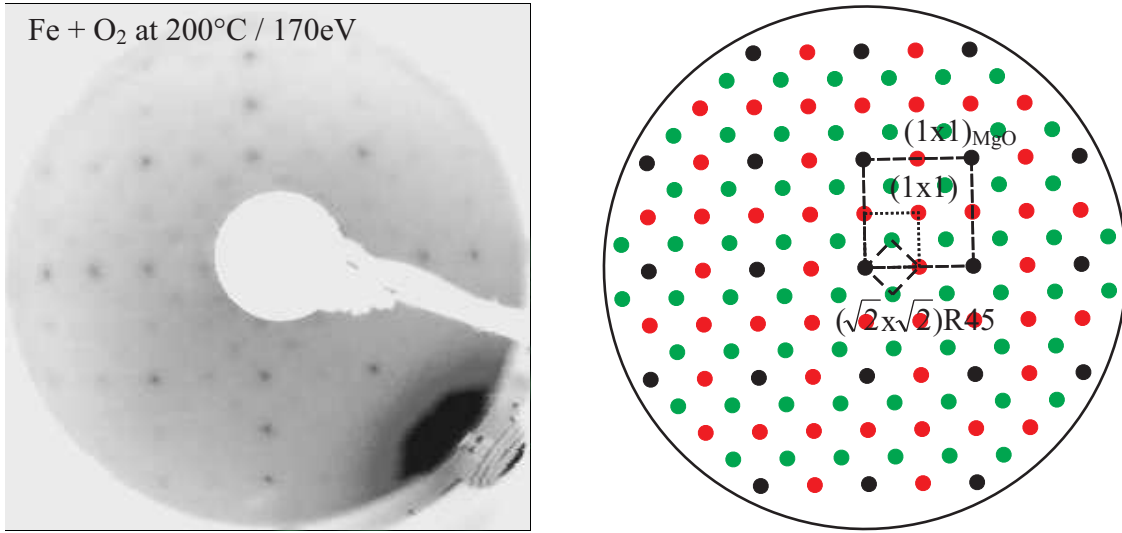
Figure 5.37: *LEED pattern for the sample deposited reactively in oxygen atmosphere at* 200 °C. *A* $(\sqrt{2} \times \sqrt{2})R45°$ *reconstruction can be seen. The pattern is illustrated in the right. Black markers indicate a* $(1 \times 1)_{MgO}$ *pattern, red markers belong to the doubled surface unit cell and green markers show the reconstruction spots. Image was taken at an electron energy of* 170 eV.
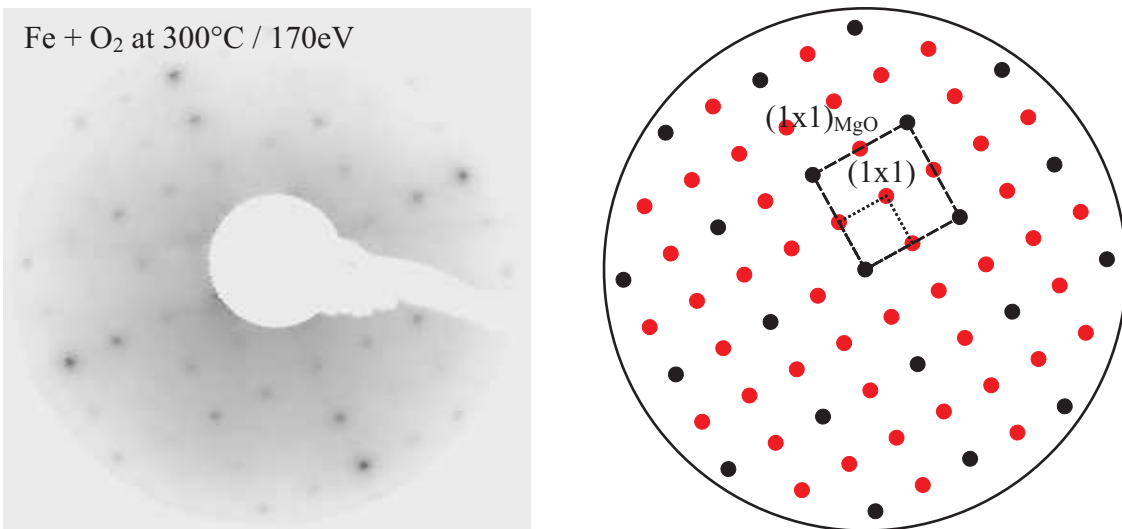
Figure 5.38: *LEED pattern for the sample deposited reactively in oxygen atmosphere at* 300 °C. *The image shows a* (1×1) *pattern illustrated in the right. Black markers indicate a* $(1 \times 1)_{MgO}$ *pattern. Image was taken at an electron energy of* 170 eV.

Deposition in oxygen atmosphere at $200\,°C$ leads to the pattern shown in Figure 5.37. The image shows a $(\sqrt{2} \times \sqrt{2})R45°$ reconstruction, the (1×1) surface unit cell has twice the size of MgO. The pattern is illustrated in the right of the Figure with the same colors for the markers as before.

The LEED pattern for the sample prepared at $300\,°C$ is presented in Figure 5.38. The image shows a (1×1) structure without any additional spots as illustrated in the right of the Figure.

5.4 Post-Oxidation Annealing

The annealing of the samples oxidized after deposition at RT and at $100\,°C$ is investigated for two different reasons. For the first sample no LEED pattern can be observed after the oxidation. In this case annealing without oxygen atmosphere is done in order to achieve a crystalline structure of the film. The second sample is annealed to produce an iron oxide film with a stoichiometry as near as possible to FeO.
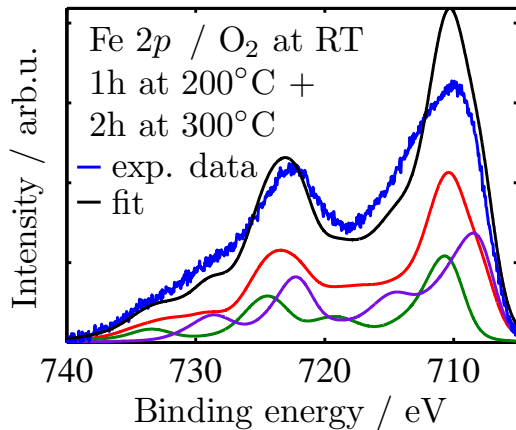
Figure 5.39: *Fitting of the Fe 2p photoemission spectrum of the sample oxidized at RT after three annealing steps at $200\,°C$ and $300\,°C$. The calculated spectra of magnetite (red), maghemite (green) and wustite (purple) are scaled down to their respective ratios in the fit.*

The sample oxidized previously at RT is annealed for one hour at $200\,°C$ and then for two more hours at $300\,°C$. The fitting of the Fe 2p photoemission spectrum after the third step is presented in Figure 5.39. No characteristic satellite is visible, but the low binding energy shoulder of the main Fe $2p_{3/2}$ peak is increased compared to the spectrum after oxidation. This indicates an increased ratio of Fe^{2+} in the film. Figure 5.40 summarizes the ratios obtained from the fitting of the Fe 2p photoemission spectra. The last step of the oxidation described in Section 5.2.3 is shown again as initial step 0 for comparison. The dashed line marks the change in the annealing temperature. The only change in the photoemission spectrum is the vanishing signal of metallic iron. The composition of the film remains almost the same during all steps and temperatures.

The ratios of the elements in the sample during the annealing are given in Figure 5.41. After three hours of annealing no change in the concentrations of elements in the film can be observed.

The observed LEED pattern of the sample after the third annealing step is shown in Figure 5.42. By looking at the line profiles in Figure 5.43 the pattern can be identified as a (1×1) structure with a unit cell twice as large as MgO. This is illustrated in the right of Figure 5.42. Black markers indicate the original $(1 \times 1)_{MgO}$ pattern, red markers belong to the new doubled unit cell. For clarity some characteristic spots are marked in both Figures.
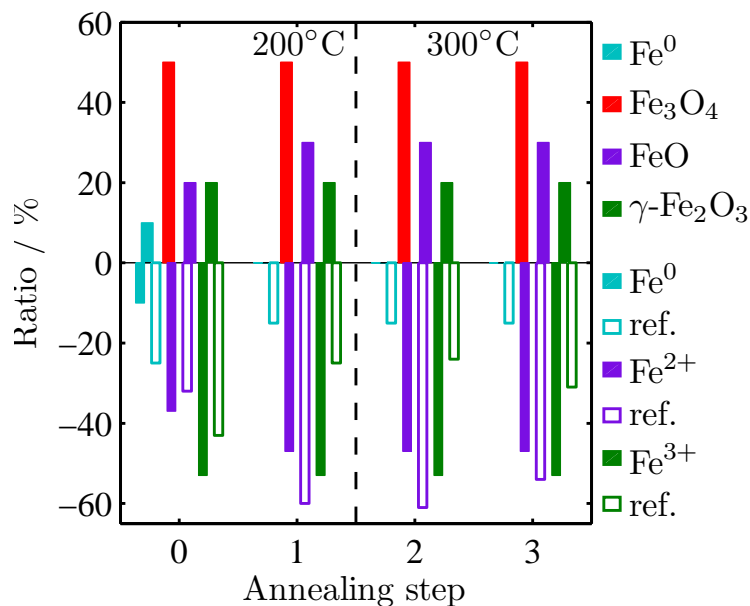
Figure 5.40: *Fe 2p fitting results for the annealing process of the sample oxidized at RT (upper part). From these values the ratios of Fe ions are calculated (lower part). The reference values for the ion ratios are taken from [51]. The annealing temperature is $200\,^{\circ}\mathrm{C}$ at the first step and $300\,^{\circ}\mathrm{C}$ for the following two steps.*
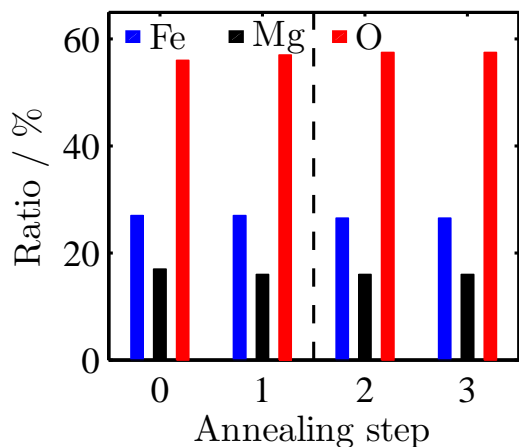
Figure 5.41: *Ratios of Fe (blue), Mg (black) and O (red) obtained from the Fe 3p region and the O 1s peak for the annealing process of the sample oxidized at RT. The initial step is the same as the last step of the oxidation shown in Figure 5.16.*
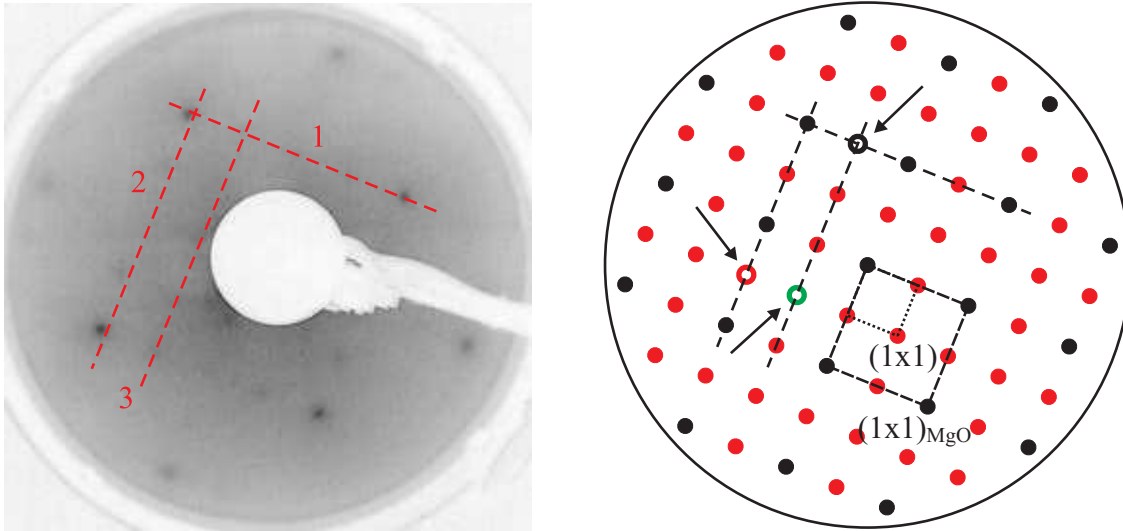
Figure 5.42: *LEED pattern of the sample oxidized at RT after three hours of annealing at 200 °C and 300 °C. The film shows a (1 × 1) structure. The observed pattern is illustrated in the right. Black markers indicate a (1×1)$_{MgO}$ pattern, red markers belong to the doubled surface unit cell. The highlighted spots mark points in the line profiles in Figure 5.43 taken at the positions indicated in the left image. Image was taken at an electron energy of 170 eV.*
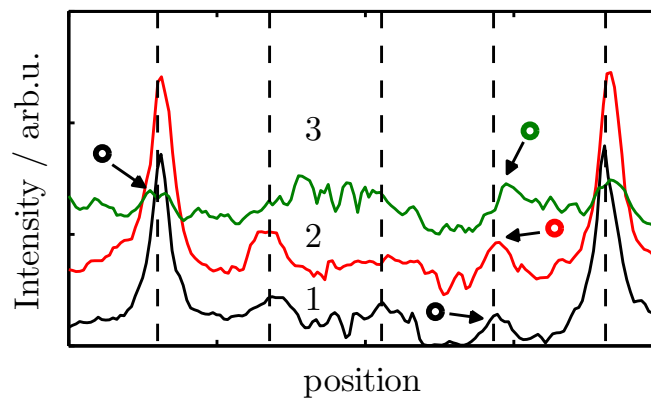
Figure 5.43: *Line profiles from the LEED pattern of the iron film oxidized at RT after annealing. The positions of the lines are indicated in the left in Figure 5.42. Interesting spots are marked by colored circles, they refer to the spots indicated in the right of Figure 5.42. They confirm a (1 × 1) structure.*

The second sample that has been annealed is the iron film oxidized at $100\,°C$. This sample is treated seven times for one hour, the first step at $200\,°C$, and the other six steps at $300\,°C$. Figure 5.44 shows the results of the fitting for the Fe $2p$ photoemission spectra. After the first annealing step at $200\,°C$ the spectrum remains the same as before. Only after raising the temperature to $300\,°C$ for the following steps a gradually increasing content of wustite is visible in the data. A characteristic satellite at $6\,eV$ higher binding energy from the main Fe $2p_{3/2}$ peak is growing continually with each treatment. The ratios of the oxide species resulting from the fits are presented in Figure 5.45. After the first annealing at $300\,°C$ a small amount of metallic Fe reappears in the film, but the signal vanishes again with further treatments at high temperature.
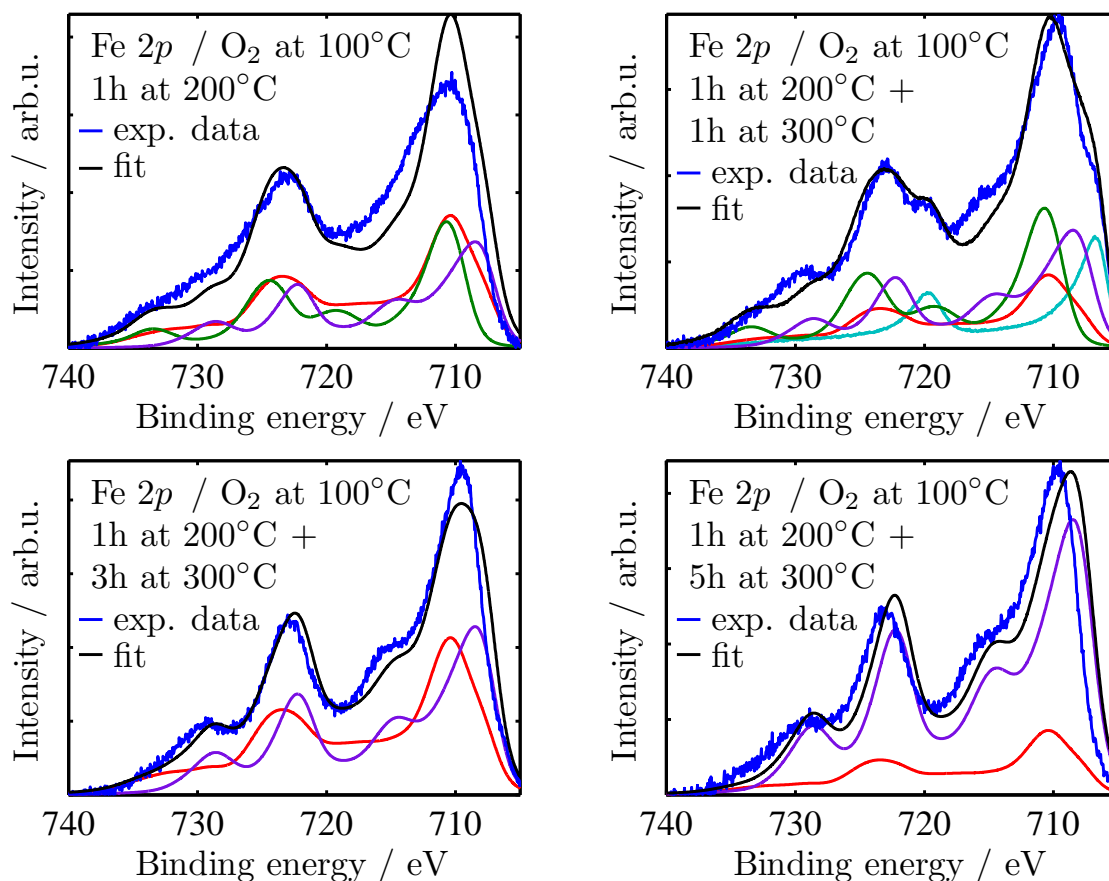
Figure 5.44: *Fitting of the Fe $2p$ photoemission spectra of the sample oxidized at $100\,°C$ after the first (top left), second (top right), fourth (bottom left) and sixth (bottom right) treatment in $1 \cdot 10^{-6}\,mbar\ O_2$. The calculated spectra of magnetite (red), maghemite (green) and wustite (purple) are scaled down to their respective ratios in the fit.*

From the Fe $3p$ and O $1s$ spectra the ratios of iron, magnesium and oxygen in the sample are obtained, the values are given in Figure 5.46. Again a temperature of $200\,°C$ is not sufficient to alter the composition of the sample in a significant way. Only for an annealing
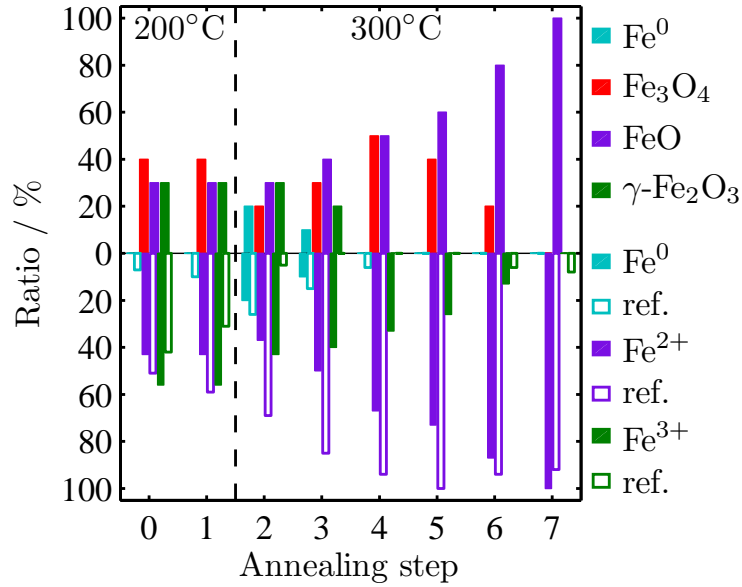
Figure 5.45: *Fe 2p fitting results for the annealing process of the sample oxidized at* 100 °C *(upper part). From these values the ratios of Fe ions are calculated (lower part). The reference values for the ion ratios are taken from [51]. The annealing temperature is* 200 °C *at the first step and* 300 °C *for the following steps.*

temperature of 300 °C changes are visible in the spectra. A signal for Mg appears and increases evenly. At the same time the Fe ratio decreases with a similar slope, while the ratio of oxygen decreases once after the first step at 300 °C and then remains constant.

The LEED results for the annealing of this sample are presented in Figure 5.47. In the top,
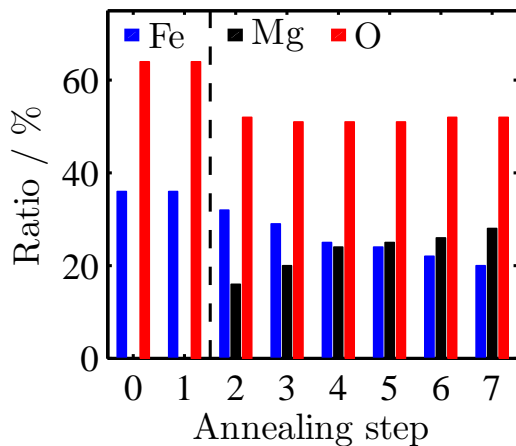
Figure 5.46: *Ratios of Fe (blue), Mg (black) and O (red) obtained from the Fe 3p region and the O 1s peak for the annealing process of the sample oxidized at* 100 °C. *The initial step is the same as the last step of the oxidation shown in Figure 5.18.*

showing the pattern after the first annealing step at 200 °C, the structure already visible during the oxidation (cf. Section 5.3.1) is now enhanced in quality. Two perpendicular (2×1) patterns domains can be observed. After raising the temperature to 300 °C (bottom) the LEED pattern changes to a sharp $(1 \times 1)_{MgO}$ structure with a surface unit cell of the same size as the substrate. For repeated annealing at this temperature the LEED pattern vanishes completely, indicating that the crystalline structure of the film surface is destroyed.
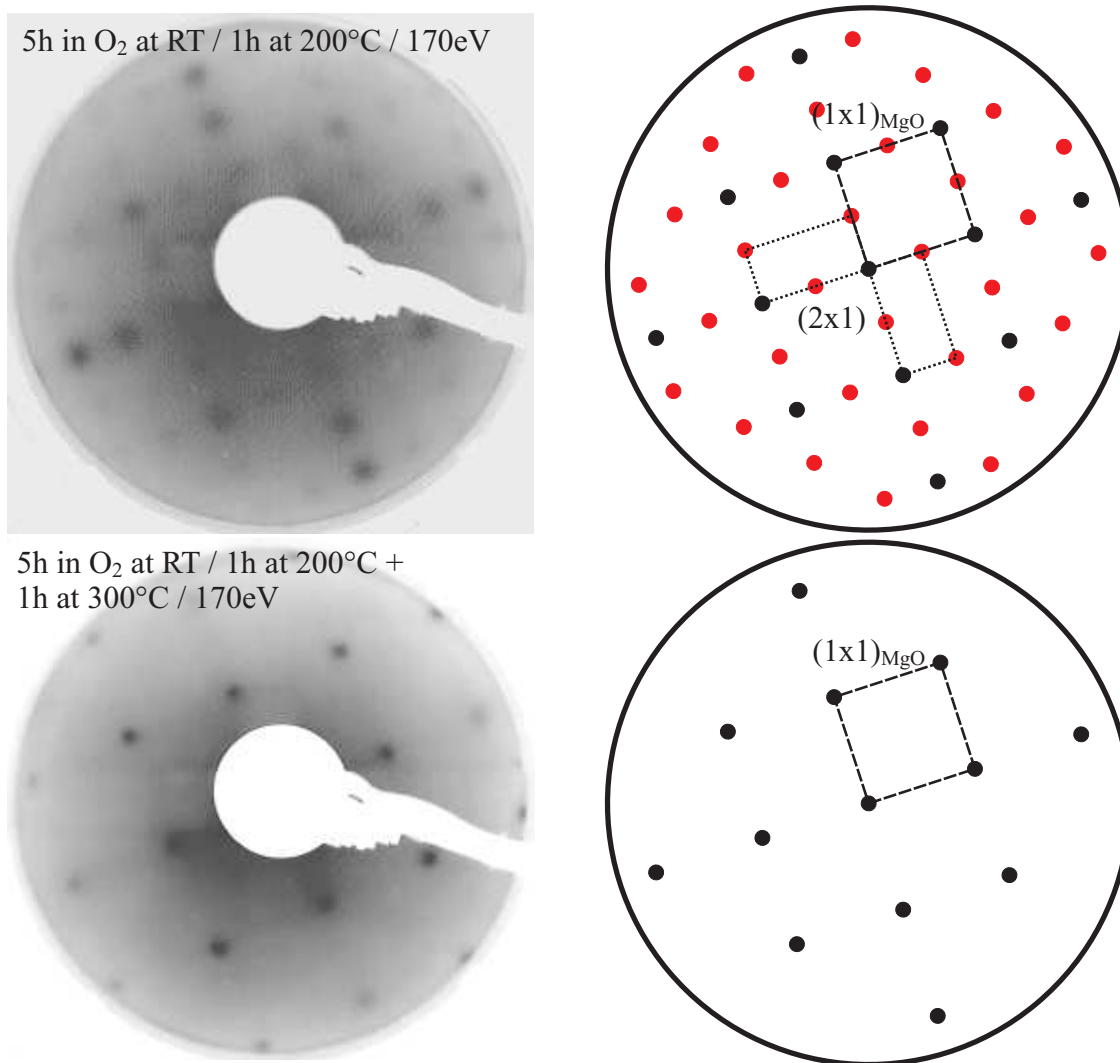
Figure 5.47: *LEED patterns of the sample oxidized at* 100 °C *after one annealing step at* 200 °C *(top) and after a second step at* 300 °C *(bottom). The perpendicular (2×1) patterns created during oxidation first become more clear, then change to a $(1 \times 1)_{MgO}$ pattern. The patterns are illustrated in the right half of the Figure. Black markers indicate a $(1 \times 1)_{MgO}$ pattern, red markers belong to the larger surface unit cell of the (2×1) domains. Images were taken at an electron energy of* 170 eV.

6 Discussion of the experimental results

All films examined during this work were prepared with a deposition rate for iron of $10\,\mathrm{Hz/s}$ (as read from the oscillating quartz on the evaporator) for the pure iron films and $5\,\mathrm{Hz/s}$ for the films deposited in oxygen atmosphere. Using the XRR data that were taken for the samples this can be estimated to correspond to a deposition rate of less than $0.2\,\text{Å/s}$ for the samples deposited in oxygen atmosphere. This value is near to values already reported in literature for the preparation of iron oxide films [14, 12]. The preparation of iron oxide by oxidizing pure iron films can not be described by a deposition rate since the films are not formed while depositing material. The oxygen incorporated into the film later can not be quantified in this way.

The formation of different iron oxide phases is influenced by the substrate temperature during the film preparation. Not only the stoichiometry but also the structures of the films change for varying temperatures. For the interpretation of the experimental results one must bear in mind that XRR and XRD probe the structure of the complete film while LEED probes only the surface of the samples. Similarly only the upper parts of the films thicker than $10\,\mathrm{nm}$ are probed by XPS, while for the thinner samples even the substrate contributes to the spectrum.

The iron film oxidized at RT is only about $38\,\text{Å}$ thick (after the following annealing of the sample), thus for all preparation steps a large photoelectron signal of the substrate must be expected. This can indeed be seen in the Fe $3p$ region. When determining the ratios of elements in the film, the contribution of oxygen from the substrate must be taken into account. After subtraction of the substrate signal the ratio between oxygen and iron in the film is 1.45. This value is lower than for the oxidation at higher temperatures, as is to be expected (cf. Figure 5.28). In spite of the small film thickness a considerable signal of iron in the metallic state is visible. It follows that the diffusion depth of oxygen atoms adsorbing on the surface of the iron film is considerably less than the film thickness of about $4\,\mathrm{nm}$. The adsorption of oxygen does not result in an ordered film surface, the LEED image shows no diffraction spots at all. In addition, XRD shows that the film shows no crystalline structure. This implies that the results of the fitting of the Fe $2p$ photoemission spectra in this case are questionable, because they are achieved by reference spectra for highly ordered oxides. Although the development of the ion ratios in Figure 5.16 seems similar to the reference data, the deviation between the two methods is rather high in this case. The oxidation at higher temperatures leads to samples with a clear crystalline structure together with a better agreement between the fit results. The applicability of the fitting method for XPS used in this work should therefore be restricted to crystalline samples.

The values obtained for the vertical lattice constants (cf. Section 5.1) of the following samples deviate rather strongly from expected bulk values of stoichiometric oxide phases. This can only partly be explained by strain imposed on the films by the substrate. If, for example, magnetite was pinned to the larger lateral lattice constant of MgO a relaxation of the vertical lattice constant to smaller values would be expected. This is indeed observed

for the films prepared at $200\,^\circ$C. For wustite on MgO one would expect an increase of the vertical lattice constant because the unit cell is compressed in the lateral direction. Neither of these effects is observed here for any sample. This suggests that for temperatures below $200\,^\circ$C the films grow in a non-stoichiometric oxide phase between FeO and Fe_3O_4 [58].

The oxidation of iron at $100\,^\circ$C results in a film that shows no signal of metallic iron in XPS after two hours. Thus the oxidation of the iron film extends at least to a depth equal to the IMFP of the photoelectrons at this temperature, about $5\,$nm. No satellite features are visible in the Fe $2p$ photoemission spectra during the oxidation, the broadness of the main Fe $2p_{3/2}$ peak is a sign of both Fe^{2+} and Fe^{3+} contents in the film. The fitting likewise indicates almost equal ratios of the different oxide species in the film, with a slight excess of Fe^{3+} ions compared to Fe^{2+}. This composition of the film remains unchanged after the second hour in oxygen atmosphere. The appearance of a LEED pattern makes the fitting result more reliable compared to the oxidation at RT. Considering the mixed ratios of oxides in the film, the observed LEED pattern can be attributed to different surface terminations of the non-stoichiometric spinel structure described above. The (001) surface of the spinel structure is highly polar. The crystal lattice perpendicular to this surface consists of alternating A and B layers. In the B layer oxygen forms an fcc lattice with metal ions occupying the octahedral sites between the oxygen atoms. The A layer consists of tetrahedral metal sites. In literature different models describing this surface and its reconstructions under varying conditions are discussed using either a B termination [16] or an A termination [15, 17] of the surface. Both models can result in the characteristic $(\sqrt{2} \times \sqrt{2})\mathrm{R}45^\circ$ reconstruction also observed in this work. The models can be adapted to explain the (2×1) patterns observed in this work. This is illustrated in Figure 6.1. The A termination proposed in [17] (left) assumes a half filled ordered A layer that forms the usual reconstruction (dotted square). By moving every second tetrahedral ion from the I positions to the II positions the surface structure is changed to a (2×1) pattern (dashed rectangle). The B termination described in [16] (right) assumes one oxygen vacancy per surface unit cell to give the characteristic reconstruction (dotted square). Refilling every second vacancy I and II gives the new reconstruction (dashed rectangle). The same may be achieved by doubling the number of oxygen vacancies from every second atom in (100) or (010) direction to completely empty rows. However this explanation seems unlikely because of the strong oxygen $1s$ signals in XPS. In both cases the (2×1) pattern will be possible in two orthogonal orientations because of the cubic basis of the structure. An alternative model with B termination is introduced in [18], where wavelike dislocations of the octahedral rows at the surface are proposed. This model can not explain the rectangular LEED pattern because of the fourfold symmetry of the calculated dislocations of the surface atoms.

The weakness of the LEED pattern for this sample suggests that the film still exhibits a large number of defects or disorder at this temperature. An influence of Mg from the substrate on the film can not be observed. XPS shows no signals for Mg after five hours of oxidation, which confirms the assumed film thickness of about $170\,$Å and demonstrates clearly that the onset for the segregation of Mg into the film lies at a higher temperature.
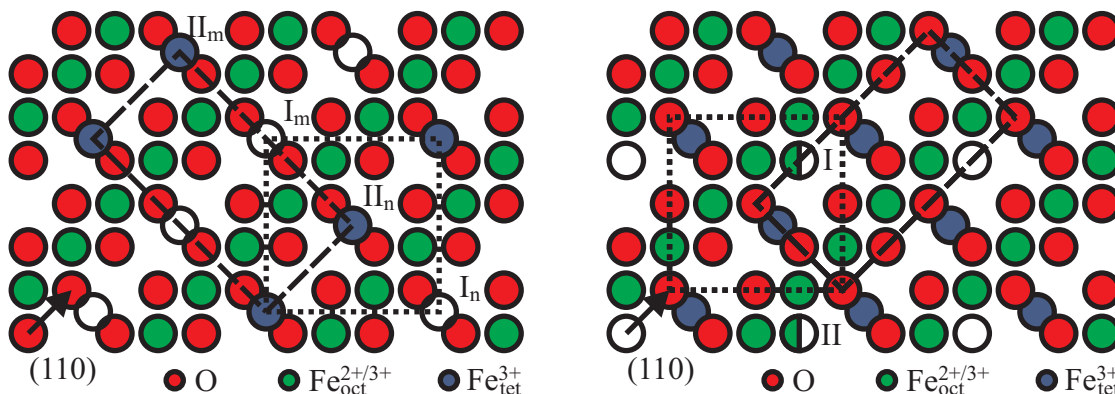
Figure 6.1: *Models for a (2 × 1) surface reconstruction of a spinel (001) surface with A termination (left) and with B termination (right). Open circles represent tetrahedral ion vacancies or oxygen vacancies, respectively. In A termination the characteristic ($\sqrt{2} \times \sqrt{2})R45°$ reconstruction (dotted squares) of magnetite can change to a (2 × 1) structure (dashed rectangles) if every second tetrahedral ions moves from a I_n to a II_n site. In B termination the same can be achieved by filling every second oxygen vacancy I and II.*

This sample has been annealed without oxygen afterwards to achieve a stoichiometric and crystalline wustite film. At 200 °C a reduction of the sample is not observed in XPS, the spectra and ratios are completely unaffected by the annealing at this temperature. The (2 × 1) LEED patterns are slightly more clearer than before, indicating an increased order of the film surface. Raising the annealing temperature to 300 °C instantly changes the surface structure to a $(1 \times 1)_{MgO}$ pattern expected for wustite. XRD shows that the film exhibits a crystalline bulk structure with a vertical lattice constant between MgO and FeO, demonstrating that despite the obvious wustite structure at the surface the film still is in a non-stoichiometric mixed phase between FeO and Fe_3O_4. Photoemission spectra demonstrate that the reduction of the film happens very fast, the ratio of oxygen decreases only once for the first treatment at 300 °C, afterwards it is stable. At the end of the annealing process a strong Fe^{2+} satellite is visible in the Fe $2p$ spectrum, the film consists almost entirely of Fe^{2+} ions. However, during the annealing at 300 °C a signal for Mg appears in the photoemission spectra and increases constantly during the process. This Mg must have segregated into the film because prior to annealing the iron oxide film shows no such contamination. The intensities of the photoemission signals further show that the film thickness has not decreased significantly, demonstrating that the substrate is not exposed. Instead the absence of intensity oscillations caused by the film thickness in XRR suggest that the interface between substrate and film has vanished due to the mixing of Mg and Fe. The increasing incorporation of Mg into the film leads to a reduction of the surface structure, showing that the arrangement of Mg in the crystal lattice is random. The annealing process of this sample shows that the onset of Mg segregation into the film lies between 200 °C and 300 °C. This value is low compared to literature where interdiffusion of Fe and Mg is observed at 450 °C [14] and 520 °C [15], which supports the assumption

from Section 4.1.1 that the temperature measurements in our UHV chamber are rather inaccurate.

Increasing the temperature during oxidation to $200\,°C$ results at first in almost the same stoichiometry as before. XPS shows that after one hour the film consists of more Fe^{3+} than Fe^{2+}, the dominant structure is magnetite. After two hours of oxidation LEED shows a very clear $(\sqrt{2} \times \sqrt{2})R45°$ reconstructed surface that additionally suggests a highly ordered magnetite structure. But unlike before at lower temperatures, with further exposure to oxygen Mg starts to appear at the film surface. This Mg must have segregated into the film, because for the pure Fe film the Mg signal was completely suppressed in XPS, and XRR shows the film to have a thickness of about $170\,Å$. The process is not very fast at this temperature, but after six hours the amounts of Fe and Mg at the top of the film are almost equal. The presence of Mg affects the film structure in a way that the original surface reconstruction is altered into the already observed (2×1) domains. The fact that the same pattern has been observed without the presence of Mg for the oxidation at $100\,°C$ shows that the surface structure of the iron oxide film depends only on the ordering of the film surface and not on the elements in the terminating layer. In this case the existence of the characteristic surface reconstruction shows that the film initially has a spinel structure, and XRD confirms that this structure is preserved after the change to the (2×1) surface structure. Although the crystal structure of the film does not change the fitting of the XPS data is affected by the replacement of Fe for Mg in the film. It has been stated in literature that Mg atoms replace some of the Fe^{2+} on octahedral sites during the segregation into an iron oxide film [15], but also compositions of $(Mg_{1-x}Fe_x)_{tet}[Mg_xFe_{2-x}]_{oct}O_4$ with $0 \leq x \leq 1$ are possible [60]. The charge transfer calculations for magnetite at this point always assume an equal ratio of the three different Fe ions in the crystal lattice. A replacement of some Fe ions by Mg will change these ratios and thereby also the spectral shape produced by the characteristic satellites. Therefore the fitting method attributes the observed satellite to maghemite, which exhibits a very similar spectrum. The application of the charge transfer calculations to the formation of magnesium-iron composites will be discussed in more detail later.

The sample oxidized at $300\,°C$ shows very clearly the segregation of Mg from the substrate to the film surface. The initial iron film is free of any Mg components, confirming the assumption that the film is about $170\,Å$ thick. But after only one hour in oxygen the contents of Mg and Fe in the oxidized film are almost equal, the incorporation of Mg into the film proceeds much faster at this temperature then before. The ratio of Fe^{3+} ions is increased compared to the other samples and the increase of the Fe^{3+} ratio is much faster than at lower temperatures. The fitting results for XPS indicate that the film is almost fully oxidized after only two hours of exposure to oxygen with nearly no Fe^{2+} remaining. But as already stated above, the presence of Mg suggests the formation of magnesium ferrite rather than maghemite. The LEED pattern supports this conclusion, the $(\sqrt{2} \times \sqrt{2})R45°$ reconstruction characteristic for a magnetite structure can be well observed and gets only slightly weaker during five hours of oxidation. Compared to the film oxidized at $200\,°C$, where Mg was build into the structure over a long period of time, in this case the highly

increased segregation rate acts as a stabilizing factor for the surface structure. It must be concluded that at this temperature structural changes occur mainly in the first hour of exposure to oxygen.

The results for the second set of samples, prepared by deposition of iron in an oxygen atmosphere, are quite similar to the other preparation method discussed above, with one remarkable difference: Regardless of substrate temperature the photoemission Fe $2p$ spectra are nearly identical for all samples. Although the oxide films grow with different crystal structures for increasing substrate temperatures, the stoichiometry of the samples does barely change. No satellite features can be observed in the Fe $2p$ photoemission spectra, but the broadness of the main $2p_{3/2}$ peak indicates a mixture of Fe^{2+} and Fe^{3+} in the films. As seen from XRR data, the samples have a thickness of about $74\,\text{Å}$, which is just sufficiently thin to allow a small remaining signal of the substrate in the $3p$ region. Only for a temperature of $300\,°\text{C}$ the film shows an increased content of Mg compared to lower temperatures, which shows that at this temperature Mg segregates into the growing oxide film during deposition. The increased temperature for the segregation of Mg compared to the first set of samples can be due to the small time scale of the growth process in this case. While the oxidation in the first case lasted several hours, here the film is deposited in only a few minutes, which can impede the incorporation of Mg. The ratios of oxygen in the films are comparable to the other set of samples.

For temperatures lower than $200\,°\text{C}$ the films tend to exhibit a vertical layer distance between MgO and FeO. As described above this suggests a non-stoichiometric spinel structure. This is supported by the results of the fitting of the Fe $2p$ photoemission spectra that show similar ratios for Fe^{2+} and Fe^{3+}. The (2×1) LEED patterns follow the model proposed in Figure 6.1. This explanation is supported by the results for the sample deposited at $100\,°\text{C}$. The increased temperature does not change the structure or the composition of the film, but enables a better ordering of the film surface, resulting in a clearer LEED pattern.

The deposition of iron oxide at a substrate temperature of $200\,°\text{C}$ results in a film with a vertical layer distance of almost the magnetite bulk value, indicating that the film has grown in a stoichiometric spinel structure without any distortion. This is supported by XPS and LEED. The fitting of the Fe $2p$ photoemission spectrum shows a slightly decreased ratio of wustite with respect to lower temperatures, the absence of any satellites confirms a majority of magnetite in the film. The LEED pattern shows a $(\sqrt{2} \times \sqrt{2})R45°$ surface reconstruction that is also typical for magnetite.

Raising the substrate temperature further to $300\,°\text{C}$ results in the segregation of Mg into the growing iron oxide film. The interface between substrate and film can not be observed in XRR anymore. Apart from that the ratios of the iron ions and the oxygen content of the film are unchanged to the preparation at $200\,°\text{C}$. The XPS results suggest that the majority of the film consists of magnetite, but unlike other samples with this composition in this case no surface reconstruction has taken place. LEED shows a simple (1×1) pattern with a unit cell twice the size of MgO. This too indicates a spinel structure of

the film. An unreconstructed (1×1) surface is usually associated with maghemite, but for this sample the absence of a characteristic Fe^{3+} satellite in the Fe $2p$ photoemission spectrum argues against this. As stated above the replacement of Fe for Mg can lead to satellites uncharacteristic for the observed crystal structure, but it is evident from the cluster spectra of maghemite in Figure 5.11 that without the presence of octahedral Fe^{2+} the satellite at about 8 eV higher binding energy from the main Fe $2p_{3/2}$ peak can not be completely suppressed. Therefore the observed (1×1) pattern must be attributed to an unreconstructed magnetite surface. Compared to the sample deposited at 200 °C, in this case the influence of Mg segregated into the film prevents the formation of a surface reconstruction.

A similar (1×1) structure is obtained by the annealing of the iron film oxidized at RT. After three hours of annealing without oxygen at 200 °C and 300 °C the photoemission spectra for this sample have changed only slightly compared to the oxidation process. The increased ratio of Fe^{2+} is to be expected for annealing, the remaining signal for metallic Fe has vanished, indicating that now the complete film is oxidized. The reduction of the film to a higher Fe^{2+} ratio is surprisingly small after three hours of annealing. Additional segregation of Mg into the film can not be distinguished from the underlying substrate signal in this case. Although the accuracy of the fit results must still be considered as low, a comparison of the photoemission spectra for this sample and the one deposited reactively at 300 °C shows that the composition of the films is almost equal. The annealed film shows a very weak (1×1) LEED pattern, indicating that a surface unit cell with twice the size of the MgO unit cell has formed. This ordering of the film is restricted to the film surface because no diffraction peak of the film is observed by XRD. Nevertheless the observed surface structure can be explained in the same way as above because of the similarities between the two samples.

To summarize the structural analysis of the samples we can say that for temperatures below 200 °C the oxide films grow with a non-stoichiometric phase between FeO and Fe_3O_4. At higher temperatures the films show slightly distorted stoichiometric spinel structures. This behavior is consistent with literature where the formation of magnetite is demonstrated at temperatures above 250°C [13, 15, 17]. The size of the surface unit cell in the LEED patterns is not necessarily the same as the one of the bulk unit cell. The observed (2×1) surface structures have not yet been described in literature. Our preparation method and experimental results do not suggest explanations for this altered surface structure. The surface reconstructions can be explained by both an A or a B termination of the (001) spinel surface, the results do not support the preference of any one model. The presence of Mg in the iron oxide films is not the critical factor determining the surface structure. A temperature of at least 200 °C is needed to encourage the segregation of Mg into the oxide film, the process is accelerated for higher temperatures. This temperature is lower than reported in [15, 14] (450°C) for film growth in oxygen plasma. The lowered onset for Mg segregation in this work may be caused by the use of molecular oxygen for sample preparation, also observed in [13]. Oxygen plasma is more reactive than molecular oxygen and may therefore result in oxide films with a higher structural order, impeding easy Mg

segregation into the film. The oxidation of iron films is saturated after one hour of oxygen exposure for temperatures lower than $200\,°C$ although the films are not fully oxidized by that point. A complete oxidation of a thin iron films requires temperatures well above $200\,°C$ or very periods of exposure to oxygen. The deposition of Fe in an oxygen atmosphere results in oxide films with a higher degree of order, demonstrated by the fringes in the XRD data and the low background in the LEED images. The substrate temperate influences only the structure but not the stoichiometry of the films for this preparation method. Although the method of fitting Fe $2p$ photoemission spectra with calculated reference spectra can only be applied to samples with a good crystalline order, the results of the fitting agree well with the structures observed by XRD and LEED.

The formation of characteristic satellite structures for the oxide species containing only one iron valency demonstrates the importance of charge transfer states in these compounds. XPS is an ionizing process that leaves a core hole in the final state. This additional core hole potential has a strong influence on the ground state energies of electronic configurations by reordering the energy states in the final state configuration (cf. Figure 2.4). In the initial state the ground state configuration and the first charge transfer configuration are separated by Δ, meaning that for $\Delta = 0$ both configurations have the same weight in the mixing. With increasing Δ the charge transfer state gets less populated. In the calculations used in Section 5.2.3 for the analysis of the experimental Fe $2p$ photoemission spectra $\Delta = 2\,\mathrm{eV}$ for tetrahedral clusters and $\Delta = 4\,\mathrm{eV}$ for octahedral clusters. This results in ground states with a composition of 65% $3d^5$, 30% $3d^6\underline{L}$ and 5% $3d^7\underline{L}^2$ for the clusters in maghemite. The Fe^{2+} cluster in wustite has 79% $3d^6$, 20% $3d^7\underline{L}$ and 1% $3d^8\underline{L}^2$ character. Although the second charge transfer configurations $3d^{N+2}\underline{L}^2$ are almost unpopulated in both cases, their influence on the spectra is crucial, as can be seen in Figure 6.2. In this example the spectra (red lines) for wustite (left) and maghemite (right) are calculated using the same parameters as given in Table 5.1, only here the second charge transfer state $3d^{N+2}\underline{L}^2$ is omitted. In both cases the ground state now has 72% $3d^N$ and 28% $3d^{N+1}\underline{L}$ character. The resulting spectra show no satellite structures and do not resemble the experimental spectra (blue lines) at all. Without the second charge transfer state both calculations are very similar, demonstrating clearly that the nature of the characteristic satellites is charge transfer.

For the calculation of charge transfer multiplets only the three parameters Δ, $Te_{(g)}$ and U_{pd} are assumed to be adjustable, the remaining two parameters are obtained as $Tt_{2(g)} = -0.5\,Te_{(g)}$ and $U_{dd} = U_{pd} - 0.5\,\mathrm{eV}$. The three free parameters affect both the positions and the relative intensities of the satellites in the calculated spectrum. The satellite intensity follows from the transition matrix element between initial state $\langle\Psi_i|$ and final state $\langle\Psi_f|$ [8], which can be expressed as

$$\langle\Psi_i|1 - \frac{T^2}{\Delta\left(U_{pd} - \Delta\right)}\big|\Psi_f^*\big\rangle. \tag{6.1}$$

87
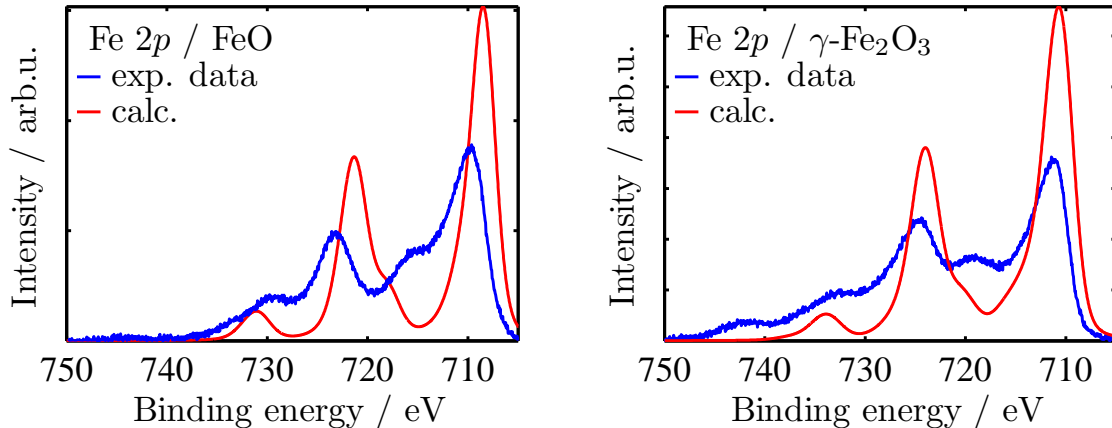
Figure 6.2: *Charge transfer calculations (red lines) for wustite (left) and maghemite (right) using only one charge transfer state. The parameters of the calculation are the same as given in Table 5.1. No satellite structures can be seen.*

The position of the satellite can be approximated by

$$\delta E \approx \sqrt{(\Delta - U_{pd})^2 + 4T^2} \tag{6.2}$$

as the energy splitting δE between main Fe $2p_{3/2}$ peak and satellite. An increase in T decreases the satellite intensity and increases the splitting between main peak and satellite. The effects of Δ and U_{pd} cancel each other almost out. The influence of the parameters on the spectrum is illustrated in Figure 6.3 for the Fe_{oct}^{2+} cluster of wustite. Here the spectrum of the sample oxidized at $100\,°C$ after the last annealing step is used as a reference because it has been shown in Section 5.4 that this spectrum consists almost purely of Fe^{2+}. For the sake of completeness the crystal field strength has been included in the Figure, because it is the only other adjustable parameter. A crystal field value of $1\,eV$ is a good approximation to the spectrum, a further decrease of the value does not alter the calculation while a greater increase to $1.2\,eV$ results in absurd satellite positions. It can easily be seen from the Figure that the parameters Δ and U_{pd} mainly affect the satellite intensity. The hybridization T has the strongest influence on the spectrum. An increase of T by $0.2\,eV$ affects the spectrum as much as increasing Δ and U_{pd} by $1\,eV$ and $2\,eV$, respectively.

The Fe_{oct}^{2+} cluster used for wustite in the fitting of the experimental Fe $2p$ photoemission spectra was assumed to be equal to the Fe_{oct}^{2+} cluster in magnetite. However, the lattice constant of wustite is larger than the one of magnetite, which will effect the charge transfer parameters of the calculation. The hybridization T should vary with the atomic distance as $T \propto r^{-3.5}$ according to Harrinson's relation [61]. With increasing distance a decrease of T can be expected. Similarly the screening of the core hole potential U_{pd} depends on the atomic distance as $\propto r^{-3}$ [62], which will result in an increased value of U_{pd} in wustite compared to magnetite. The charge transfer energy Δ is proportional to the MADELUNG energy described in Section 2.1.2.4. The MADELUNG energy increases with growing ionic
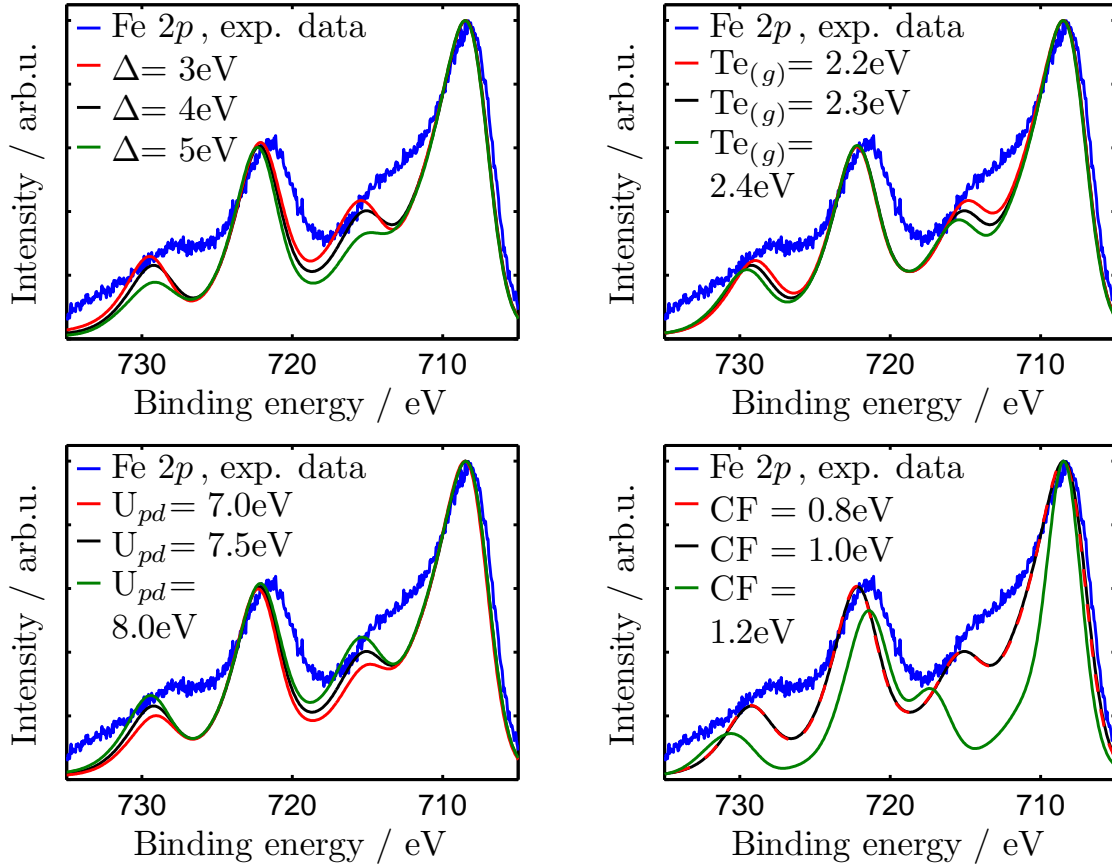
Figure 6.3: *Influence of the parameters Δ (top left), T (top right), U_{pd} (bottom left) and crystal field strength (bottom right) on the calculated Fe 2p photoemission spectrum of wustite. The blue line gives the experimental spectrum associated with wustite.*

character of the atomic bindings and decreases for larger atomic distances [63]. Both effects have a similar influence on the charge transfer energy and cancel each other out to a certain degree. Figure 6.4 illustrates the optimization of the parameters. First the hybridization strength is reduced to $Te_{(g)} = 2.1\,\mathrm{eV}$ as it has the strongest influence on the spectrum (left image). The position of the characteristic satellite is shifted to lower binding energies, the energy separation between main line and satellite is now about $6.0\,\mathrm{eV}$, agreeing well with literature [52]. The satellite intensity is also nearer to the experimental spectrum. In the right image in addition to the decreased hybridization the value of U_{pd} is increased to $8\,\mathrm{eV}$ as predicted by theory. This shifts the satellite position again to slightly higher binding energy ($\delta E = 6.2\,\mathrm{eV}$) and increases the satellite intensity. An increase in Δ to $5\,\mathrm{eV}$ can compensate these changes in the spectrum. The decreased hybridization T in wustite suggests that the Fe-O bonds in this oxide are more ionic than in magnetite, supporting an increasing value for Δ. In this case the increase due to the ionic character of the bonds must be greater than the decrease caused by the greater atomic distance in wustite.
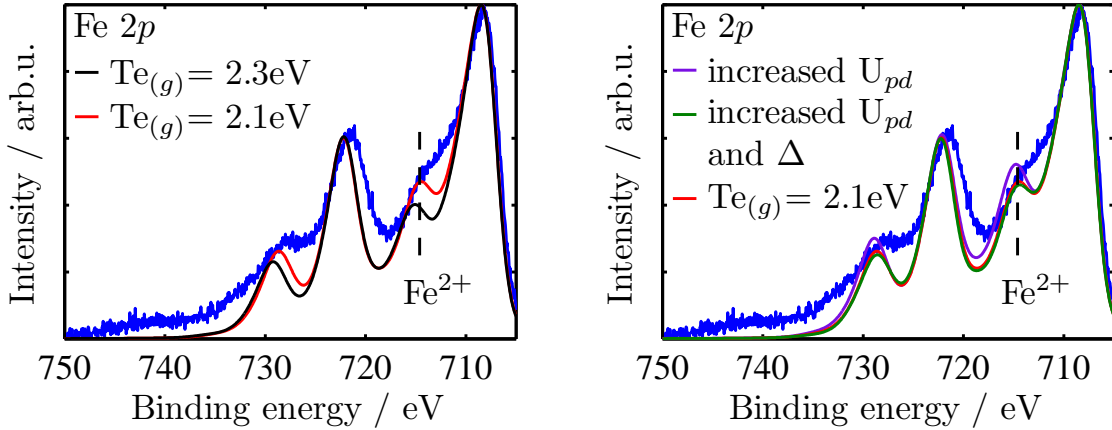
Figure 6.4: *Optimized Fe 2p photoemission calculation of an Fe^{2+}_{oct} cluster of wustite. The hybridization $Te_{(g)}$ is decreased to 2.1 eV (left). Complying to theoretical expectations U_{pd} and Δ are also increased (right). The new spectrum is in better agreement to the experimental data (blue line) than the original one.*

The distance between octahedral Fe^{2+} and oxygen in magnetite and wustite differs by about 4 % [8, 52]. Harrinson's relation therefore predicts a value of $T_{FeO} \approx 0.88 \cdot T_{Fe_3O_4} \approx 2.0$ eV for Fe^{2+}_{oct}. The value found above is larger, suggesting that the atomic distance in the film is smaller than the literature value. This result agrees well to the observations using XRD stated above, which shows that charge transfer calculations alone can determine lattice distortions in the film.

The formation of Fe^{3+} ions requires higher temperatures during the oxidation process. As shown above this encourages the segregation of Mg atoms into the iron oxide film, where Mg^{2+} ions are supposed to replace Fe^{2+} ions on octahedral sites. As a result the crystal structure and surface reconstruction of magnetite are preserved while the photoemission spectrum seems to indicate a maghemite film. Charge transfer calculations can reproduce this discrepancy by considering the varying ratios of the Fe clusters in a magnetite spectrum. This is illustrated in Figure 6.5. The topmost spectrum is the original calculation for magnetite used above. Going through the next spectra from top to bottom, the ratio of Fe^{2+}_{oct} has gradually been decreased in steps of 10 %, supposing that an increasing amount of Fe^{2+}_{oct} sites is occupied by Mg. In the lowest spectrum no Fe^{2+}_{oct} remains in the film. With decreasing Fe^{2+} content the calculated spectrum shifts slowly to the slightly higher binding energy of Fe^{3+} clusters and the main peaks become more narrow. As the intensity of the Fe^{2+} satellite decreases, the spectrum becomes dominated by the Fe^{3+} satellite. For comparison the experimental spectrum of the sample oxidized for five hours at 300 °C (blue line) is given, which was assumed to contain only Fe^{3+} ions. This spectrum is here calibrated to the binding energy of the calculations to clarify the changes in satellite position and intensity. Comparing the calculated spectra to the experimental data a ratio of about 30 % Fe^{2+} left on the octahedral sites gives the best agreement. Supposing that

all Fe^{2+} vacancies are occupied by Mg this gives a total ratio between Fe and Mg of about 3/1 instead of the 1/1 ratio obtained from the Fe $3p$ region.
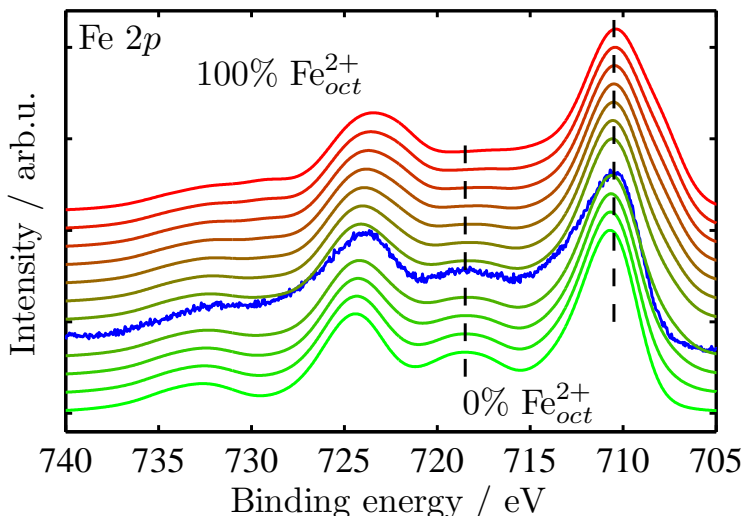
Figure 6.5: *Calculated Fe 2p photoemission spectra for magnetite. The ratio of Fe^{2+}_{oct} is decreased in steps of 10 % from top to bottom. For comparison the experimental spectrum of the sample oxidized for five hours at 300 °C (blue line) is shown.*

To account for the higher content of Mg in the film, it must therefore be assumed that additionally some of the Fe^{3+} sites are either also occupied by Mg or are unoccupied. Furthermore, the binding energies of the Fe peaks in the experimental photoemission spectra of this sample are much nearer to literature values for maghemite, indicating that the film contains almost no Fe^{2+} ions. With these considerations a calculated spectrum can be compiled for any ratio of Fe ions occupying the different Fe sites by scaling down the respective cluster calculation in the summation. This leads to a large number of possible combinations that give a correct satellite position and intensity. This is illustrated exemplarily in Figure 6.6. The calculations plotted in shades of green above the experimental spectrum (blue line) show good agreement. They refer to combinations of Fe ratios of 0%/80%/80%, 10%/60%/80%, 10%/70%/80% and 20%/70%/80% on the Fe^{2+}_{oct}, Fe^{3+}_{oct} and Fe^{3+}_{tet} sites, respectively (from top to bottom). The lower two calculations given in red do not match the data, they refer to combinations of Fe ratios of 40%/50%/60% and 10%/70%/50% (top to bottom). From these examples two general conclusions can be drawn. Firstly, that the ratio of Fe^{2+}_{oct} sites occupied by Fe must be at most 20%, and secondly that more tetrahedral than octahedral Fe^{3+} sites are occupied by Fe ions. For other combinations of ratios with higher Fe^{2+}_{oct} content or more Fe^{3+} ions on octahedral than on tetrahedral sites the satellite is either too weak or not visible at all, or it is shifted to much lower binding energy.

The optimization of the parameters in the charge transfer calculation in this case is more
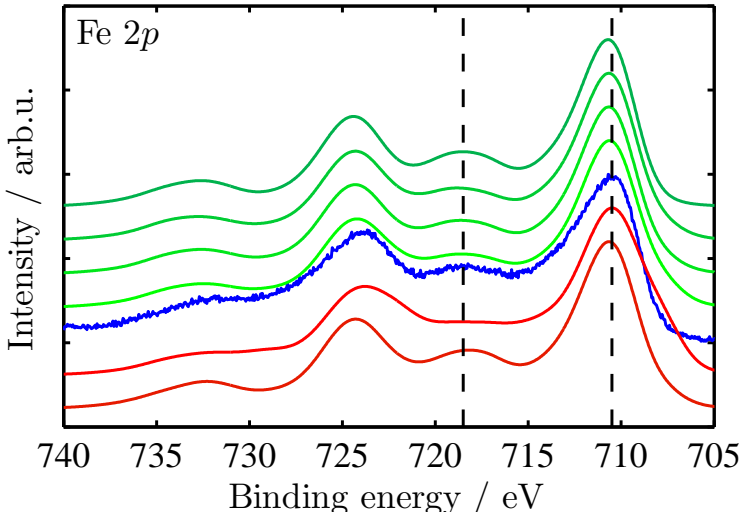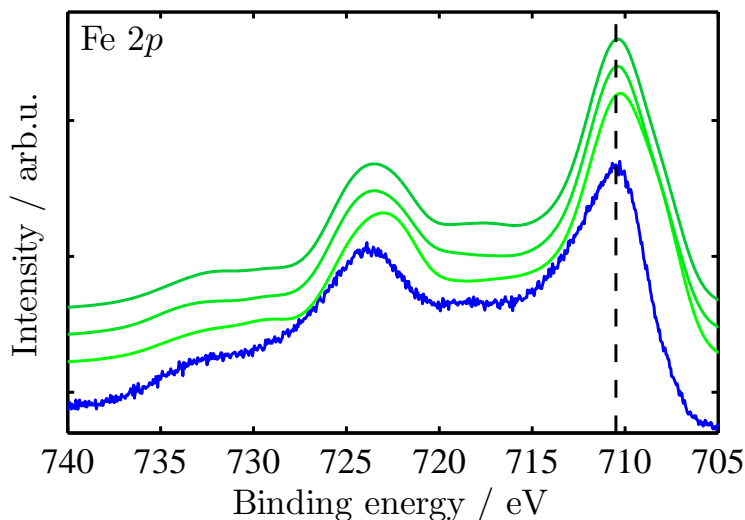
Figure 6.6: *Calculated Fe 2p photoemission spectra for magnetite with varying ratios of Fe ions on the respective Fe sites. The calculations plotted in shades of green refer to combinations of Fe ratios of 0%/80%/80%, 10%/60%/80%, 10%/70%/80% and 20%/70%/80% on the Fe_{oct}^{2+}, Fe_{oct}^{3+} and Fe_{tet}^{3+} sites, respectively (from top to bottom). The lower two calculations given in red refer to combinations of ratios of 40%/50%/60% and 10%/70%/50% (top to bottom). For comparison the experimental spectrum of the sample oxidized for five hours at 300 °C (blue line) is shown.*

difficult than for the wustite because here three different Fe clusters have to be considered. When going from pure magnetite to an increasing content of Mg in the crystal structure, it can be assumed that the atomic distance on octahedral sites decreases while it increases on tetrahedral sites [8, 64, 65]. As discussed above an increase in distance results in a decrease in hybridization and an increase in core hole potential. Calculations using these considerations are shown in Figure 6.7. For the octahedral clusters $Te_{(g)}$ is increased by 0.1 eV and U_{pd} is decreased by 0.5 eV. For the tetrahedral Fe^{3+} cluster $Te_{(g)}$ is decreased and U_{pd} increased by the same values. The same combinations of Fe ratios as in Figure 6.6 are shown. Although the changes in the cluster spectra are comparable to the optimization of wustite (cf. inset in Figure 6.7), the summed up spectra are mostly unchanged by the new parameter values. This is caused by the huge differences in the spectral shape between octahedral and tetrahedral symmetry, which causes the effects of changing parameter values to cancel each other out.

Only combinations of ratios that have about 50% of all Fe sites occupied by Fe ions result in a good agreement between the calculated spectrum and the experimental data. This does not necessarily imply that the other half of the sites are occupied by Mg, but considering the overall ratio between Fe and Mg observed in the Fe 3p spectrum this is very likely. It has
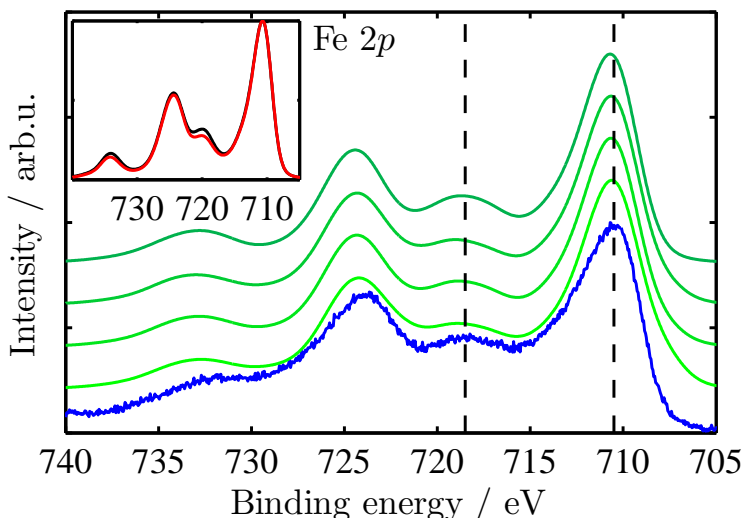
Figure 6.7: *Optimization of the charge transfer parameters for the calculated Fe 2p photoemission spectrum of magnetite with varying ratios of Fe ions occupying the respective Fe sites. For the octahedral clusters $Te_{(g)}$ is increased by 0.1 eV and U_{pd} is decreased by 0.5 eV, for the tetrahedral Fe^{3+} cluster $Te_{(g)}$ is decreased and U_{pd} increased by the same values. The same combinations of ratios as in Figure 6.6 are shown. For comparison the experimental spectrum of the sample oxidized for five hours at $300\,°C$ (blue line) is shown. The inset shows the difference between the original (red line) and optimized (black line) Fe^{3+}_{tet} calculations.*

been shown that the ratio of Mg in the film is saturated after the first treatment in oxygen atmosphere (cf. Section 5.2.4). Therefore the gradual appearance of the characteristic Fe^{3+} satellite for prolonged oxidation can not be attributed to an increasing Mg content of the film. Instead Figure 6.8 shows that the Fe $2p$ photoemission spectrum after one hour in oxygen at $300\,°C$ (blue line) can be well reproduced by calculations using different Fe ratios than before. The three given calculations refer to Fe ratios of 40%/50%/40%, 40%/40%/50% and 50%/40%/40% on the Fe^{2+}_{oct}, Fe^{3+}_{oct} and Fe^{3+}_{tet} sites, respectively (from top to bottom). Again only combinations with about 50% of the Fe sites occupied by Fe result in spectra similar to the experimental data.

These results strongly suggest that the composition of the film is near to $Mg_{1.5}Fe_{1.5}O_4$. In the initial oxidation step about one third of the Mg atoms occupy tetrahedral sites, during the oxidation this ratio gradually decreased to about 15%. As seen from the LEED patterns the surface structure of the film is barely affected by this exchange of Mg and Fe on tetrahedral sites, which suggests that the surface reconstructions are formed by the ordering of the film surface rather than by different elements occupying surface sites. The same effects can be observed for the sample oxidized at $200\,°C$. With prolonged treatment

Figure 6.8: *Calculated Fe 2p photoemission spectra for magnetite with varying ratios of Fe ions on the respective Fe sites. The calculations plotted in shades of green refer to combinations of Fe ratios of 40%/50%/40%, 40%/40%/50% and 50%/40%/40% on the Fe^{2+}_{oct}, Fe^{3+}_{oct} and Fe^{3+}_{tet} sites, respectively (from top to bottom). For comparison the experimental spectrum of the sample oxidized for one hour at $300\,°C$ (blue line) is shown.*

Mg tends to occupy more octahedral sites than initially, only in this case the overall ratio of Mg in the film is smaller. The Fe 2p photoemission spectrum therefore shows a weaker satellite, the spectrum is more similar to pure magnetite. The deposition in oxygen atmosphere takes place on a much shorter time scale. Accordingly, with this preparation method the segregation of Mg into the film at $300\,°C$ is even less pronounced, only about every fourth Fe site is occupied by Mg. The resulting deviations from a pure magnetite spectrum are very small and can not be detected by the calculations.

Although the original fitting of the Fe 2p photoemission spectra does not include the optimized parameter values and compositions in the calculated spectra, the comparison to the alternative fitting method shows good agreement between the obtained ratios of iron ions. This is an indication that the position and strength of the characteristic satellites derived from charge transfer calculations are a suitable way to analyze XPS data. The fitting results also support the structural information obtained from XRD and LEED. The optimization of the charge transfer parameters following theoretical predictions results in an improved agreement to experimental data. Photoemission spectra of Fe 2p and similar elements and peaks showing multiplet structures have been studied extensively in the past [66, 59, 67], but only few authors conduct Charge Transfer Multiplet calculations for the analysis of the spectra [68, 69, 8]. In these cases the calculations are used only to investigate the electronic properties of the compounds. In this work it is shown that

the analysis of photoemission data by Charge Transfer Multiplet calculations can give additional information about structure and composition of thin films. Deviations of the lattice constant from bulk values can be detected as well as changes in the occupation of atomic sites. Charge transfer calculations can describe the oxidation process of Fe very well and provide a useful tool in characterizing iron oxide films of unknown composition.

7 Summary and outlook

In the course of this work two sets of iron oxide films were prepared under UHV conditions. The first set of samples consisted of iron films deposited on a MgO(001) substrate with the substrate held at room temperature. These films were afterwards oxidized in $1 \cdot 10^{-6}$ mbar O_2 at different film temperatures between room temperature and $300\,°C$. The second set of samples was prepared by reactive deposition of iron in an oxygen atmosphere of 1×10^{-6} mbar. For these samples the substrate temperature during deposition was held constant at values between room temperature and $300\,°C$. The structural properties of the films were investigated X-ray Reflectivity (XRR), X-ray Diffraction (XRD) and Low Energy Electron Diffraction (LEED), while the chemical properties were determined by X-ray Photoelectron Spectroscopy (XPS). Charge Transfer Multiplet calculations of Fe $2p$ photoemission spectra were used to analyze XPS measurements.

The results showed that for preparation temperatures below $200\,°C$ the films tended towards vertical lattice distances between MgO and wustite, while at higher temperatures the vertical lattice distances was slightly smaller than for magnetite. The observed vertical layer distances deviated from expected bulk values, indicating both the formation of non-stoichiometric oxide phases and distortions of the unit cell. Only the deposition in oxygen atmosphere at $200\,°C$ resulted in a crystalline stoichiometric magnetite film, other preparation parameters either changed the crystal structure or led to contaminations with Mg segregated into the film from the substrate. This process could be observed for both preparation methods at high temperatures. Deposition in oxygen atmosphere showed a higher onset for this effect, which was attributed to the shorter time scale compared to the other preparation method. It was shown that the presence of Mg in the iron oxide films is not responsible for the different surface structures observed in LEED. In addition to the $(\sqrt{2} \times \sqrt{2})R45°$ surface reconstruction characteristic for magnetite a (2×1) reconstruction in two orthogonal domains was observed for both bulk structures and regardless of the presence of Mg in the film. Surface models involving A or B termination could both describe the surface reconstructions of the oxide films. Neither model was favored by the results of this work. A satisfying explanation for the previously unobserved (2×1) surface structures could not be found based on the current data.

Charge Transfer Multiplet theory was used to calculate Fe $2p$ photoemission spectra of the iron oxides wustite, magnetite and maghemite. Fitting the experimental Fe $2p$ photoemission data with the calculated spectra led to a good approximation of the spectral shape. The results agreed well with values determined by an alternative fitting method using experimental reference spectra. The charge transfer calculations could reproduce the spectral features of the experimental spectra at all preparation steps. The ratios of the iron oxide species obtained from the fitting matched the expectations and supported the observations from XRD and LEED. The charge transfer parameters were then optimized following theoretical predictions, which led to an improved agreement between calculation and experiment. For the simplest case of wustite the new parameter values indicated unit cell dimensions of the film deviating from expected bulk values in accordance with XRD

results. Furthermore the presence of Mg in the films could be well described by scaling down the influence of the respective Fe site in the calculation, assuming that the site is occupied by Mg. Only calculations including a ratio between Fe and Mg similar to the values obtained from the Fe $3p$ photoemission spectra produced reasonable results. It could be shown that Mg occupies all sites in the spinel structure, but with prolonged exposure to oxygen it tended to occupy octahedral sites.

Some aspects of the oxidation process remain unclear at this point. To further investigate the surface termination of iron oxides a combination of angle resolved XPS and Scanning Tunneling Microscopy (STM) may be able to determine which termination is present for our preparation methods, and whether the observed (2×1) reconstructions can be attributed to only one termination. Additional work [58] also showed that iron films tend to grow in mixed phases in a layer system. The determination of such systems can be done by using in-situ XRD measurements and investigating additional diffraction spots on other diffraction rods. Particularly in the case of films oxidized after the deposition of iron the uniformity of the oxidation needs to be checked in more detail. A combination of ion sputtering and XPS will give depth resolved data for the ratios between Fe, O and Mg in the film. This enables the characterization of the oxidation state of the film and the assignment of different layers in the film.

Additional work should also include the preparation parameters. An investigation of the influence of the oxygen pressure during the preparation is needed to gain more control over the film structure. For instance the preparation of pure maghemite is not possible under the current conditions. The undesired segregation of Mg into the film remains a huge problem when trying to achieve higher oxidation states. This may also be solved by increasing the oxygen pressure. Another technique applied in this respect is the use of a buffer layer between substrate and oxide film [70]. Unfortunately this method is restricted to the deposition in oxygen atmosphere. For a sequential deposition and oxidation this method needs to be adapted, possibly by using buffer layers of a third material.

Charge Transfer Multiplet calculations have been proven to be a useful tool for the characterization of iron oxide films. It can be used to determine oxidation states and lattice distortions without the drawback of having to remove the samples from UHV for synchrotron measurements. A detailed analysis of the oxidation process using calculated spectra can also give insight into the progression of structural changes between different oxide species. Extending the analysis to other transition metals or rare earth metals would be desirable in this respect.

The sensitivity of the calculations to the different metal sites in the crystal lattice could also be used to investigate doping effects in transition metal oxides or using transition metals as a dopant. The tuning of structural, electronic or magnetic properties by controlled doping plays an important role in current investigations and technological applications.

Bibliography

[1] A. Kafizas, S. Kellici, J. A. Darr, and I. P. Parkin. Titanium dioxide and composite metal/metal oxide titania thin films on glass: A comparative study of photocatalytic activity. *J. Photochem. Photobiol., A*, 204:183, 2009.

[2] K. Ueda, H. Tabata, and T. Kawai. Magnetic and electric properties of transition-metal-doped ZnO films. *Appl. Phys. Lett.*, 79:988, 2001.

[3] F. Huang, X. Lu, W. Lin, X. Wu, and Y. Kan. Effect of Nd dopant on magnetic and electric properties of $BiFeO_3$ thin films prepared by metal organic deposition method. *Appl. Phys. Lett.*, 89:242914, 2006.

[4] S. S. Shinde, R. A. Bansode, C. H. Bhosale, and K. Y. Rajpure. Physical properties of hematite α-Fe_2O_3 thin films: application to photoelectrochemical solar cells. *J. Semicond.*, 32:013001, 2011.

[5] M. Miyauchi, A. Nakajima, T. Watanabe, and K. Hashimoto. Photocatalysis and Photoinduced Hydrophilicity of Various Metal Oxide Thin Films. *Chem. Mater.*, 14:2812, 2002.

[6] R. Joerger, T. Klaus, and C. G. Granqvist. Biologically Produced Silver-Carbon Composite Materials for Optically Functional Thin-Film Coatings. *Adv. Mat.*, 12:407, 2000.

[7] D. Lee, M. F. Rubner, and R. E. Cohen. All-Nanoparticle Thin-Film Coatings. *Nano Lett.*, 6:2305, 2006.

[8] T. Fujii, F. M. F. de Groot, G. A. Sawatzky, F. C. Voogt, T. Hibma, and K. Okada. In Situ XPS analysis of various iron oxide films grown by NO_2-assisted molecular-beam epitaxy. *Phys. Rev. B*, 59:3195, 1999.

[9] A. Yanase and K. Siratori. Band Structure in the High Temperature Phase of Fe_3O_4. *J. Phys. Soc. Jpn.*, 53:312, 1984.

[10] Y. S. Dedkov, U. Rüdiger, and G. Güntherodt. Evidence for the half-metallic ferromagnetic state of Fe_3O_4 by spin-resolved photoelectron spectroscopy. *Phys. Rev. B*, 65:064417, 2002.

[11] W. E. Pickett and J. S. Moodera. Half Metallic Magnets. *Phys. Today*, 54:39, 2001.

[12] C. Ruby, B. Humbert, and J. Fusy. Surface and interface properties of epitaxial iron oxide thin films deposited on MgO(001) studied by XPS and Raman spectroscopy. *Surf. Interface Anal.*, 29:377, 2000.

[13] N.-T. H. Kim-Ngan, A. G. Balogh, J. D. Meyer, J. Brötz, S. Hummelt, M. Zając, T. Slęzak, and J. Korecki. Structure, composition and crystallinity of epitaxial magnetite thin films. *Surf. Sci.*, 602:2358, 2008.

[14] Y. Gao, Y. J. Kim, S. Thevuthasan, S. A. Chambers, and P. Lubitz. Growth, structure and magnetic properties of γ-Fe_2O_3 epitaxial films on MgO. *J. Appl. Phys.*, 81:3253, 1997.

[15] J. F. Anderson, M. Kuhn, U. Diebold, K. Shaw, P. Stoyanov, and D. Lind. Surface structure and morphology of Mg-segregated epitaxial Fe_3O_4(001) thin films on MgO(001). *Phys. Rev. B*, 56:9902, 1997.

[16] B. Stanka, W. Hebenstreit, U. Diebold, and S. A. Chambers. Surface reconstruction of Fe_3O_4(001). *Surf. Sci.*, 448:49, 2000.

[17] S. A. Chambers and S. A. Joyce. Surface termination, composition and reconstruction of Fe_3O_4(001) and γ-Fe_2O_3(001). *Surf. Sci.*, 420:111, 1999.

[18] R. Pentcheva, F. Wendler, H. L. Meyerheim, W. Moritz, N. Jedrecy, and M. Scheffler. Jahn-Teller Stabilization of a "Polar" Metal Oxide Surface: Fe_3O_4(001). *Phys. Rev. Lett.*, 94:126101, 2005.

[19] F. de Groot and A. Kotani. *Core Level Spectroscopy of Solids*. CRC Press, 2008.

[20] T. Koopmans. Über die Zuordnung von Wellenfunktionen und Eigenwerten zu den einzelnen Elektronen eines Atoms. *Physica*, 1:104, 1934.

[21] M. P. Seah and W. A. Dench. Quantitative Electron Spectroscopy of Surfaces: A Standard Data Base for Electron Inelastic Mean Free Paths in Solids. *Surf. Interface Anal.*, 1:2, 1979.

[22] M. F. Toney, T. C. Huang, S. Brennan, and Z. Rek. X-ray depth profiling of iron oxide thin films. *J. Mater. Res.*, 3:351, 1988.

[23] K. Oura, V. G. Lifshits, A. A. Saranin, A. V. Zotov, and M. Katayama. *Surface Science: An Introduction*. Springer Verlag Berlin, 2003.

[24] D. Briggs and M. P. Seah. *Practical Surface Analysis by Auger and X-Ray Photoelectron Spectroscopy*. John Wiley & Sons, 1983.

[25] D. A. Shirley. High-resolution X-Ray Photoemission Spectrum of the Valence Bands of Gold. *Phys. Rev. B*, 5:4709, 1972.

[26] S. Tougaard and P. Sigmund. Influence of elastic and inelastic scattering on energy spectra of electrons emitted from solids. *Phys. Rev. B*, 25:4452, 1982.

[27] S. Tougaard. Universality Classes of Inelastic Electron Scattering Cross-sections. *Surf. Interface Anal.*, 25:137, 1997.

[28] B. Schneider. *Untersuchungen zur elektronischen und geometrischen Struktur ausgewählter oxidischer und sulfidischer Materialien mittels Photoelektronen- und Röntgenspektroskopie.* PhD thesis, Universität Osnabrück, 2001.

[29] P. H. Butler. *Point group symmetry applications: methods and tables.* Plenum Press, 1981.

[30] B. Zimmermann. *Epitaktisches Wachstum und Charakterisierung ultradünner Eisenoxidschichten auf Magnesiumoxid(001).* PhD thesis, Universität Osnabrück, 2010.

[31] M. Henzler. LEED from epitaxial surfaces. *Surf. Sci.*, 298:369, 1993.

[32] C. Martínez Boubeta, J. L. Costa-Krämer, and A. Cebollada. Epitaxy, magnetic and tunnel properties of transition metal/MgO(001) heterostructures. *J. Phys.: Condens. Matter*, 15:1123, 2003.

[33] O. E. Taurian, M. Springborg, and N. E. Christensen. Self-consistent electronic structures of MgO and SrO. *Solid State Commun.*, 55:351, 1985.

[34] B. Phillips, S. Sōmiya, and A. Muan. Melting Relations of Magnesium Oxide-Iron Oxide Mixtures in Air. *J. Am. Ceram. Soc.*, 44:167, 1961.

[35] W. T. Peria. Optical Absorption and Photoconductivity in Magnesium Oxide Crystals. *Phys. Rev.*, 112:423, 1958.

[36] I. M. L. Billas, J. A. Becker, A. Châtelain, and W. A. de Heer. Magnetic Moments of Iron Clusters with 25 to 700 Atoms and Their Dependence on Temperature. *Phys. Rev. Lett.*, 71:4067, 1993.

[37] C. S. Yoo, P. Söderlind, J. A. Moriarty, and A. J. Cambell. dhcp as a possible new ϵ' phase of iron at high pressures and temperatures. *Phys. Lett. A*, 214:65, 1996.

[38] H. Fjellvåg, F. Grønvold, and S. Stølen. On the Crystallographic and Magnetic Structures of Nearly Stoichiometric Iron Monoxide. *J. Solid State Chem.*, 124:52, 1996.

[39] Y. Ding, J. Xu, C. T. Prewitt, R. J. Hemley, H. Mao, J. A. Cowan, J. Zhang, J. Qian, S. C. Vogel, K. Lokshin, and Y. Zhao. Variable pressure-temperature neutron diffraction of wüstite ($Fe_{1-x}O$): Absence of long-range magnetic order to 20 GPa. *Appl. Phys. Lett.*, 86:052505, 2005.

[40] W. H. Butler, X.-G. Zhang, T. C. Schulthess, and J. M. MacLaren. Spin-dependent tunneling conductance of Fe—MgO—Fe sandwiches. *Phys. Rev. B*, 63:054416, 2001.

[41] D. O. Smith. Magnetization of a Magnetite Single Crystal Near the Curie Point. *Phys. Rev.*, 1956:959, 102.

[42] M. E. Fleet. The Structure of Magnetite. *Acta Cryst.*, B37:917, 1981.

[43] E. J. W. Verwey. Electronic Conduction of Magnetite (Fe_3O_4) and its Transition Point at Low Temperatures. *Nature*, 3642:327, 1939.

[44] E. Wolska. The structure of hydrohematite. *Z. Kristallogr.*, 154:69, 1981.

[45] C. Pecharromán, T. González-Carreño, and J. E. Iglesias. The Infrared Dielectric Properties of Maghemite, γ-Fe_2O_3, from Reflectance Measurement on Pressed Powders. *Phys. Chem. Minerals*, 22:21, 1995.

[46] X. Ye, D. Lin, Z. Jiao, and L. Zhang. The thermal stability of nanocrystalline maghemite Fe_2O_3. *J. Phys. D: Appl. Phys.*, 31:2739, 1998.

[47] T. Becker. MOKE-Untersuchungen an ferromagnetischen Metallschichten. Master's thesis, Universität Osnabrück, 2008.

[48] M. Morita, T. Ohmi, E. Hasegawa, M. Kawakami, and M. Ohwada. Growth of native oxide on a silicon surface. *J. Appl. Phys.*, 68:1272, 1990.

[49] Thomas Weisemöller. *X-ray analysis of praseodymia*. PhD thesis, Universität Osnabrück, 2009.

[50] N. F. Lane and C. C. Lin. A Semiempirical Method for the Calculation of the Slater-Condon Parameters. *Ann. Phys.*, 20:234, 1962.

[51] T. Schemme. Oxidation von Eisenschichten auf MgO(001). Master's thesis, Universität Osnabrück, 2011.

[52] T. Yamashita and P. Hayes. Analysis of XPS spectra of Fe^{2+} and Fe^{3+} ions in oxide materials. *Appl. Surf. Sci.*, 254:2441, 2008.

[53] P. C. J. Graat and M. A. J. Somers. Simultaneous determination of composition and thickness of thin iron-oxide films from XPS Fe 2p spectra. *Appl. Surf. Sci.*, 100:36, 1996.

[54] F. Bertram. Röntgenreflektometrie an ultradünnen Schichten. Bachelor Thesis, Universität Osnabrück, 2007.

[55] M. Wormington, C. Panaccione, K. M. Matney, and D. K. Bowen. Characterization of structures from X-ray scattering data using genetic algorithms. *Phil. Trans. R. Soc. Lond. A*, 357:2827, 1999.

[56] A. Greuling. Röntgenstrukturanalyse von Isolatorschichten. Master's thesis, Universität Osnabrück, 2007.

[57] C. Deiter. *Röntgenstrukturanalyse von Halbleiter-Isolater-Schichtsystemen*. PhD thesis, Universität Bremen, 2005.

[58] F. Bertram, C. Deiter, O. Hoefert, T. Schemme, F. Timmer, M. Suendorf, B. Zimmermann, and J. Wollschläger. X-ray diffraction study on size effects in epitaxial magnetite thin films on MgO(001). *J. Phys. D: Appl. Phys.*, 45:395302, 2012.

[59] N. S. McIntyre and D. G. Zetural. X-ray Photoelectron Spectroscopic Studies of Iron Oxides. *Anal. Chem.*, 49:1521, 1977.

[60] M. Gateshki, V. Petkov, S. K. Pradhan, and T. Vogt. Structure of nanocrystalline $MgFe_2O_4$ from X-ray diffraction, Rietveld and atomic pair distribution function analysis. *J. Appl. Crystallogr.*, 38:772, 2005.

[61] W. A. Harrison. *Electronic Structure and the Properties of Solids.* W. H. Freeman and Company, 1980.

[62] D. K. G. de Boer, C. Haas, and G. A. Sawatzky. Exciton satellites in photoelectron spectra. *Phys. Rev. B*, 29:4401, 1984.

[63] J. van Elp, J. L. Wieland, H. Eskes, P. Kuiper, G. A. Sawatzky, F. M. F. de Groot, and T. S. Turner. Electronic structure of CoO, Li-doped CoO, and $LiCoO_2$. *Phys. Rev. B*, 44:6090, 1991.

[64] K. B. Modi, J. D. Gajera, M. C. Chhantbar, K. G. Saija, G. J. Baldha, and H. H. HJoshi. Structural properties of magnesium and aluminium co-substituted lithium ferrite. *Mater. Lett.*, 57:4049, 2003.

[65] I. S. A. Farag, M. A. Ahmed, S. M. Hammad, and A. M. Moustafa. Study of Cation Distribution in $Cu_{0.7}(Zn_{0.3-x}Mg_x)Fe_{1.7}Al_{0.3}O_4$ by X-ray Diffraction Using Rietveld Method. *Egypt. J. Sol.*, 24:215, 2001.

[66] S. P. Kowalczyk, L. Ley, F. R. McFeely, and D. A. Shirley. Multiplet splitting of the manganese $2p$ and $3p$ levels in MnF_2 single crystals. *Phys. Rev. B*, 11:1721, 1975.

[67] A. P. Grosvenor, B. A. Kobe M. C. Biesinger, and N. S. McIntyre. Investigation of multiplet splitting of Fe 2p XPS spectra and bonding in iron compounds. *Surf. Interface Anal.*, 36:1564, 2004.

[68] A. E. Bocquet, T. Mizokawa, H. Namatame, and A. Fujimori. Electronic structure of $3d$-transition-metal compounds by analysis of the $2p$ core-level photoemission spectra. *Phys. Rev. B*, 46:3771, 1992.

[69] K. Okada and A. Kotani. Charge transfer satellites and multiplet splittings in X-ray photoemission spectra of late transition metal halides. *J. Electron Spectrosc. Relat. Phenom.*, 58:325, 1992.

[70] N.-T. H. Kim-Ngan, A. G. Balogh, J. D. Meyer, J. Brötz, M. Zając, T. Ślęzak, and J. Korecki. Thermal and irradiation induced interdiffusion in magnetite thin films grown on magnesium oxide (001) substrates. *Surf. Sci.*, 603:1175, 2009.

Bibliography

List of Figures

List of Tables

Acknowledgment

This work would not have been possible without the support of many individual people.

First of all I want to thank my thesis advisor Prof. Dr. Joachim Wollschläger who gave me the possibility to do this work. His willingness to give good advice and his pleasant manner made everything very much easier.

Thanks also to Prof. Dr. Michael Reichling for taking the time to act as secondary advisor for my thesis. Prof. Dr. Michael Rohlfing and Dr. Karsten Küpper deserve equal thanks for being part of the examination board.

A large part of my work was funded by the Phd program "Synthesis and Characterisation of Surfaces and Interfaces assembled from Clusters and Molecules" of the federal state of Lower Saxony. Synchrotron measurements were performed at the DORIS III radiation source at DESY in Hamburg with the much appreciated assistance of Wolfgang Caliebe and Florian Bertram.

Surely this work would not have been possible without an excellent work group as support. The atmosphere was always very helpful, creative, motivating, and most of the time simultaneously hilarious. A special mention must be made of the guys who did a large part of the experimental work during their diploma, master or bachelor thesis, Christian Otte, Tobias Schemme and Frederic Timmer. One could not hope for more dedicated coworkers. A special thanks also to the guys who shared years of office stress and after-office entertainment with me, Sebastian Gevers, Timo Kuschel and Daniel Bruns. These times will be sorely missed.

I also owe thanks to Christian Taubitz and Stefan Bartkowski for helping me become acquainted with Charge Transfer Multiplet calculations, and to Frank de Groot for taking the time in helping me to solve some of the more intricate mysteries of the calculations.

The experimental work contained in this thesis was greatly facilitated by the uncomplicated cooperation with the mechanics and electronics workshops of the physics department of the University of Osnabrück, who always showed great commitment to our work.

A very huge thank-you must also go to my family, whose assistance throughout my long University years can not be valued high enough. The support I received from them extended far beyond any usual level and always was a great reassurance for me.

Finally I want to thank all of my friends who put up with me all this time. I really appreciate your understanding and continuing friendship that were a great support to me. I really hope we will be having more of amusing talk, loud music, delicious drinks and dangerous dungeons together in the future. And, of course, I am especially looking forward to not having to answer certain questions any more...

Acknowledgment

Danksagung

Diese Arbeit wurde mir ermöglicht durch die Unterstützung einiger Menschen, denen ich an dieser Stelle meinen Dank aussprechen möchte.

Zunächst danke ich meinem Doktorvater und Erstgutachter Prof. Dr. Joachim Wollschläger, der mir eine Promotion ermöglicht hat. Seine stete Bereitschaft, mir mit gutem Rat zur Seite zu stehen, und seine angenehme Art waren eine exzellente Grundlage für ein erfolgreiche Arbeit.

Danken möchte ich auch Prof. Dr. Michael Reichling, der sich die Zeit genommen hat, als Zweitgutachter für meine Arbeit zu fungieren. Prof. Dr. Michael Rohlfing und Dr. Karsten Küpper gebührt ebensolcher Dank für ihr Mitwirken in der Prüfungskommission.

Ein Großteil der hier vorliegenden Arbeit wurde finanziert durch das Promotionsprogramm „Synthesis and Characterisation of Surfaces and Interfaces assembled from Clusters and Molecules" des Landes Niedersachsen. Messungen mit Synchrotronstrahlung wurden durchgeführt an der DORIS III-Strahlungsquelle des DESY in Hamburg. Ich danke Wolfgang Caliebe und Florian Bertram für ihre freundliche Unterstützung während dieser Messungen.

Mit Sicherheit wäre diese Arbeit kaum möglich gewesen ohne die Unterstützung durch eine hervorragende Arbeitsgruppe. Dort herrschte stets eine hilfreiche, kreative, motivierende und zumeist gleichzeitig ausgelassene Atmosphäre. Eine gesonderte Erwähnung verdienen die Mitarbeiter, die während ihrer Diplom-, Master- oder Bachelorarbeit weite Teile der Messungen durchgeführt haben, Christian Otte, Tobias Schemme und Frederic Timmer. Engagiertere Kollegen findet man wohl nur schwerlich. Besonderer Dank geht auch an meine ehemaligen Bürokollegen Sebastian Gevers, Timo Kuschel und Daniel Bruns, die lange Jahre an Arbeitsstress und abendlicher Entspannung mit mir teilten. Diese Zeit wird mir fehlen.

Dank schulde ich auch Christian Taubitz und Stefan Bartkowski, die mir die ersten Schritte mit Charge Transfer Multiplets erleichtert haben, sowie Frank de Groot für die Beantwortung vieler manchmal trivialer Fragen und das Lösen einiger der eher ungewöhnlichen Probleme bei den Berechnungen.

Der experimentelle Teil dieser Arbeit wurde sehr erleichtert durch die unkomplizierte Zusammenarbeit mit der Feinmechanischen Werkstatt und der Elektronikwerkstatt des Fachbereichs Physik der Universität Osnabrück, deren Mitarbeiter jederzeit großes Engagement an den Tag legten.

Ein sehr großes Dankeschön gebührt schließlich meiner Familie, deren Unterstützung im Verlauf meiner Universitätszeit kaum hoch genug eingeschätzt werden kann. Dieser große Rückhalt hat mir in vielen Momenten neue Kraft gegeben.

Zuletzt möchte ich all meinen Freunden danken, die mich seit so langer Zeit ertragen. Euer Verständnis und unsere andauernde Freundschaft bedeuten mir viel. Ich hoffe, es wird in
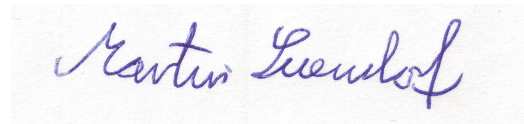
Zukunft noch mehr spaßige Unterhaltungen, laute Musik, leckere Getränke und gefährliche Verliese geben. Und natürlich freue ich mich sehr darauf, gewisse Fragen endlich nicht mehr hören zu müssen...

Hiermit erkläre ich an Eides statt, die vorliegende Abhandlung selbstständig und ohne unerlaubte Hilfe verfasst, die benutzten Hilfsmittel vollständig angegeben und noch keinen Promotionsversuch unternommen zu haben.

Osnabrück, 29. Oktober 2012

Martin Suendorf